Durham E-Theses

Molecular organic photonics

Gray, David

How to cite:

Use policy

Abstract

The work presented in this thesis is derived from experimentation in the field of molecular organic photonics. This is done from the standpoint that devices cannot be understood without recourse to the molecular properties and vice versa.

A background of nonlinear optics and a brief introduction to the origins of molecular organic nonlinearity is given to aid understanding of the main points of the argument.

The dipole moment of several organics was calculated using a simple capacitance method which has been successfully applied to reactive species. These dipole moment results were necessary in the extraction of β_ω from the $\mu\beta_\omega$ extracted from the EFISH technique. This experiment was performed at $1.064\mu m$ and $1.907\mu m$ with the latter wavelength being applied to the first in a new class of organic molecules.

Results of the work on a number of techniques relevant to thin film devices are also presented. This culminated in an amplitude modulator case study that brought all the techniques together.

Finally a discussion on the links between molecular and device related properties justifies the approach taken.

Acknowledgements

Molecular Organic Photonics

David Gray

Submitted for the degree of Doctor of Philosophy

Durham University

Department of Physics

September 1994

Contents

List of Figures

List of Tables

Declaration

I hereby declare that the work reported in this thesis has not previously been submitted for any degree and is not being currently submitted in candidature for any other degree.

Signed_____

The work reported in this thesis was carried out by the candidate. Any work not carried out by the candidate is acknowledged in the main text.

Signed_____

PhD Supervisor

Signed_____

Candidate

Statement of copyright

The copyright of this thesis rests with the author. No quotation should be published without his prior written consent and information derived from it should be acknowledged.

Chapter 1

Introduction

This body of work is concerned with organic materials in the context of photonics, where photonics can be defined as replacing traditional techniques of information technology using electronics with devices employing photons. The area encompassed by this definition is vast so in this work only transmission, optical switching, and frequency doubling are studied.

To try and reproduce the function of electronics with light was not possible until the advent of the laser, which could provide a coherent intense light source. With a ruby laser [1, 2] the first demonstration of nonlinear optics resulted in doubling the frequency of light. Up to this point none of the nonlinear phenomena studied had been at optical wavelengths [3, 4, 5, 6]. At this stage in the development of nonlinear optics more emphasis was placed on exploring phenomena rather than materials. Until the late 1960s work was carried out on such phenomena as:

- Sum–Frequency Generation [7]

- Parametric Amplification [8, 9]

- Two–Photon Absorption [10]

- Four–Wave Mixing [11]

- Intensity Dependent Refractive Index [12]

- Surface Nonlinear Optics [13]

This is just a small sample of many [14, 6].

It became clear that the available materials, although possessing the appropriate symmetry and transparency, were far from optimal. Materials such as potassium dihydrogen phosphate (KDP) and ammonium dihydrogen phosphate (ADP) originally developed for ultrasonic transducers, and so conforming to quadratic nonlinearity symmetry constraints, served as the starting point for inorganic compound research. These materials are important for bulk applications with the deuterated form of KDP, termed KD*P still the most common frequency doubling crystal in commercial laser systems [15].

Organic materials had not been identified as proving useful for nonlinear optics in part due to the scarcity of experiments being carried out on organics, and in part because the multi–disciplinary research needed had yet to be established. This situation changed as with the advent of the powder second harmonic generation (SHG) technique [16] a semi–quantitative method became available to screen inorganic and organics without having to go through the often long process of crystal growth.

Semi–conductor materials have also attracted interest and are similar to organics in that their optical properties can be tuned to a certain degree [17]. This can be done by the use of differing dopants and also by the recently developed technique of multi–quantum well (MQW) structures. The semi–conductor field can therefore be considered as a "competitor" to organic materials. This work is concerned with quadratic nonlinear effects coupled

to a suitability for devices with the focus on the use of organics.

Work on organics in the early 1970s, confirmed theoretical predictions of quadratic nonlinearities [18], using a two level model [6]. This work showed that organics with larger conjugation lengths gave rise to a higher quadratic nonlinearity.

Among techniques developed for measuring the second order nonlinearity, β, was electric field induced second harmonic (EFISH) [19] which had been set on a firm footing by the late seventies [20, 21]. The EFISH technique's next major advance was through Singer [22, 23], who developed a concentration dependence technique from earlier work on the determination of dipole moments [24].

From the results of work on powder SHG and EFISH [25] a large base of materials had been investigated. However this was from the point of view of available materials being investigated rather than the deliberate synthesis of improved materials for investigation. Work by two major groups, (Bell Labs and CNET), on the design and synthesis of promising molecules shifted the emphasis to more aggressive, directed research. Not only was an investigation made into molecules with high nonlinearity but this was extended to tailoring these molecules to grow favourable crystal structures for bulk nonlinearity. This culminated in the synthesis and crystal growth of N–(4–nitrophenyl)–(L)–prolinol (NPP) [26, 27] which is probably still the best example of this molecular engineering approach.

For practical devices that can be integrated with existing technologies a thin film [28] or doped fibre approach [29] is more appropriate than bulk crystals. The main reason for this is the long interaction lengths that are possible at high optical power densities [30, 31] which is not possible by

focusing in bulk materials. Several attempts have been made to grow crystals in film form [32, 33, 34] but growth in the correct orientation and with low enough optical losses for in-plane propagation has been difficult to achieve.

Over the last few years the complexity of single crystal thin film fabrication seems to have been superseded by polymer organics. These materials have the advantage that there is a large knowledge base of working with polymers in the semi–conductor industry for thin film processing. Using polymers doped with nonlinear molecules the previous work on molecular nonlinearity can be drawn on, including molecular materials whose bulk crystal structure is noncentrosymmetric.

Using crosslinkable and side–chain bonded polymers has made progress in addressing the main problems associated with poled polymer devices, namely relaxation back to centrosymmetric structures.

Enough work has now been done on organics in devices for them to be comparable with devices from existing inorganics such as KDP. However, as is usually the case a new technology has to prove itself superior rather than just comparable to an established technology to replace it. The case of frequency doubling organic devices to blue wavelengths is a likely example of this and makes it a good candidate in the market for organic devices. This is because producing a direct room temperature continuous wave (c.w.) diode laser is extremely difficult [35]. Sony for instance have only managed devices with a few minutes lifetime [36] after three years of concerted effort. Another reason is that because of the lack of progress in making direct blue lasers there is not the difficulty of replacing an incumbent technolgy.

The stage for nonlinear optical devices as far as organics is concerned is that poled polymer devices, side chain or doped, seem to be the best candi-

dates for the future. Nevertheless basic material properties still have to be improved as device performance is still not far enough in advance of inorganics for industrial interest. As material properties in the context of device fabrication can be so different it is sensible for molecular and device related properties to be investigated in parallel. Here this work adopts this principle and always tries to relate the findings concerning molecular properties to issues pertaining to device fabrication and performance.

To that aim Chapter 2 presents an introduction to nonlinear optics. The phenomenological approach is described first so that an intuitive feel for the subject can be gained. A more formal quantum method is presented next, with emphasis on the two–level model, which has been used with much success in the description of organic molecules [20]. The correlation between macroscopic and microscopic nonlinearities essential for the analysis of EFISH measurements is discussed. In the EFISH technique three media and four boundaries are negotiated by the primary beam and three boundaries for the harmonic. To help understand the assumptions used in the analysis a description of the propagation of the second harmonic is given.

Chapter 3 shows the general structure of organic molecules that possess high nonlinear coefficients and why they are thought to have them. In addition there is a description of the molecules studied and the reasons for their inclusion.

Chapter 4 gives the theoretical and experimental techniques used to determine β_0, the first molecular hyperpolarisability extrapolated to zero frequency. In the process the dipole moment μ must be determined as part of the alignment factor to isolate β_ω. The experiment to determine μ is described. A description of the laser system used to measure the macroscopic

nonlinearity and the data analysis used is also included in this chapter.

Chapter 5 describes the fabrication methods and measurement techniques important in polymeric thin film devices. Fabrication methods used were the spinning and withdrawal techniques. The technique used depends on the polymer solvent's volatility. The measurements described are prism coupling and end–fire coupling where prism coupling is used to measure film thickness and refractive index. Prism coupling is also used to measure waveguide loss. A special case of prism coupling called the M–line technique for more absorbing films is also described. The poling of polymers and measurement of the electro–optic coefficient r_{33} using two techniques is given.

Chapter 6 presents the results of the measurements performed on the molecules described in Chapter 3. This gives the dipole moment measured, and calculated for each. Calibrations of the high voltage supply, the glass windows, and the quartz standard were performed. Due to absorption of the second harmonic for one of the systems (DEMI, see Chapter 3) a longer wavelength was used. Several difficulties presented themselves while working with DEMI and the modifications made to the EFISH cell are described. Finally experimental β_0 values are given for each of the four materials and compared to theoretical calculations.

Chapter 7 describes the experiments carried out with the aim of producing a proof of principle device. The device chosen was an amplitude modulator using a commercially available polymer guide layer. Studies of this device utilised all the available techniques apart from loss determination. The refractive index was also measured of several other polymers and doped polymer systems. Loss measurements were made on a doped system. Most measurements were taken using a HeNe laser but some were taken at

1.3 μm with an in–house built laser because of visible absorption problems. The "blue" refractive index of DEMI doped polymer films was also measured with an argon ion laser. At the end of this chapter preliminary work is presented on compatibilty issues associated with a combination of reactive ion etching (RIE) and photolithography to produce channel waveguides of $\approx$ 10 $\mu m \times$ 2 $\mu m \times$ 5 mm.

Chapter 2

Nonlinear Optics

2.1 Introduction

In this chapter the models used to describe the interaction of light with organic molecules will be presented. The phenomenological approach is presented first as this gives a feel for how these particular systems respond. For more accurate calculations a quantum mechanical perturbation technique is presented. The relationship between the measured response and the microscopic parameters given by theory will be discussed in detail.

Apart from giving a general background to terms used in the literature, this chapter will present the special cases in the experiments performed and how they tie in to the overall framework.

2.2 Phenomenological Approach

For dielectrics Drude and Lorentz [37] considered that the valence electrons were held in equilibrium by linear restoring forces which could be set in motion by an electric field. To account for nonlinear effects this model can

be generalised by the inclusion of higher order terms for the restoring force. Under the action of an electric field a stress is set up in the dielectric and the polarisation P is a measure of the increase in flux due to this stress, and can be expressed as

$$P = \chi^{(1)} E \tag{2.1}$$

where E is the applied field, and χ is the susceptibility. When the nonlinear terms are included, the field strength is low, and the medium is assumed to be lossless and dispersionless, the polarisation can be expressed as a power series in the field strength, E

$$P = \chi^{(1)} E + \chi^{(2)} E^2 + \chi^{(3)} E^3 + \ldots \tag{2.2}$$

where the equation is in Gaussian units [37, 38]. $\chi^{(2)}$ and $\chi^{(3)}$ are the quadratic and cubic nonlinear susceptibilites respectively. For reasons of clarity the tensor nature of Eq. 2.2 will be ignored for the moment.

If the time varying field is taken to be sinusoidal, $E = E_0 \cos(\omega t)$ then the polarisation can be expressed as

$$P = \chi^{(1)} E \cos(\omega t) + \chi^{(2)} E^2 \cos^2(\omega t) + \chi^{(3)} E^3 \cos^3(\omega t) + \ldots \tag{2.3}$$

which can also be written

$$P = \chi^{(1)} E_0 + \frac{1}{2}\chi^{(2)} E_0^2 \left[1 + \cos(2\omega t)\right] + \chi^{(3)} E_0^3 \left[\frac{3}{4}\cos(\omega t) + \frac{1}{4}\cos(3\omega t)\right] + \ldots \tag{2.4}$$

This means that the polarisation gives rise to Fourier components at static and harmonic frequencies of the exciting field.

If anisotropic media are to be examined then it is expected that the polarisation response is also in directions other than the applied field. This requires rewriting Eq. 2.2 using tensor notation

$$P_i = \chi^{(1)}_{ij} E_j + \chi^{(2)}_{ijk} E_j E_k + \chi^{(3)}_{ijkl} E_j E_k E_l + \ldots \tag{2.5}$$

which follows the Einstein convention used in the literature [39, 40] and used throughout this work. Repeated indices are summed over the three directions of space, x, y, and z, where 1 represents the x axis, 2 represents the y axis, and 3 represents the z axis. Manipulating this expression can be cumbersome so the polarisation is often split up into terms equated with the power of the field. In the case of the quadratic term this is

$$P^{(2)}_i = \chi^{(2)}_{ijk} E_j E_k \tag{2.6}$$

Inverting Eq. 2.6 transforms E_j and E_k to $-E_j$ and $-E_k$. In materials that possess an inversion symmetry $P^{(2)}_i$ must transform to $-P^{(2)}_i$ giving

$$- \chi^{(2)}_{ijk} (-E_j)(-E_k) = \chi^{(2)}_{ijk} (E_j)(E_k) \tag{2.7}$$

which implies that $\chi^{(2)}_{ijk} = 0$ for materials that have inversion symmetry, i.e. centrosymmetric materials. This holds under the approximation that dipolar contributions to the polarisation are the most significant, termed the "dipole approximation". i.e. polarisable entities are small compared to the wavelength [41, 24, 26].

In general, 27 independent components of the $\chi^{(2)}$ tensor exist and twelve $\chi^{(2)}$ tensors are needed to represent the different polarisations possible. For-

tunately this number can be greatly reduced by considering the physical properties of the nonlinear susceptibility.

The polarisation is a physically measurable quantity as is the electric field, so, as the susceptibility relates these two quantities it must be constrained so that the polarisation remains real. The number of independent quantities is therefore reduced. For the case of a lossless medium, known as "full permutation symmetry", all the coefficents of $\chi^{(2)}$ must be real and it can be shown that only 27 coefficients are now independent [37, 17]. A further contraction may be valid in the case where all the frequencies are smaller than the resonance frequency, which means that the susceptibility is independent of the input frequency. This is known as Klienmann's symmetry [42, 43]. In the case of second harmonic generation this can reduce the number of independent coefficients to only 10. Any further contraction depends on the specific systems studied and their crystal class. These can be found in one of the standard texts e.g.[44].

2.3   Anharmonic Oscillator Model

The classical approach is to model the optical properties of a medium as the response of an assembly of forced harmonic oscillators [39]. This is achieved by solving the familiar equation of motion

$$\frac{d^2r}{dt^2} + 2\gamma\frac{dr}{dt} + \omega_0^2 r = -\frac{e}{m}E \tag{2.8}$$

where r is the displacement of the electron from it's equilibrium position, e is the charge of the electron, m is the mass of the electron, ω_0 is the natural resonance frequency, γ is the damping constant, and E is the applied field.

Solving this equation for time varying fields gives

$$r = -\frac{e}{m}E(\omega)\frac{e^{i\omega t}}{\omega_0^2 - 2i\gamma\omega - \omega^2} + c.c. \qquad (2.9)$$

If the dipole approximation is used [26] a medium with electron density N has $P = -Ner$. Combining this with Eq. 2.9 gives

$$P = \frac{Ne^2}{m}\frac{1}{\omega_0^2 - 2i\gamma\omega - \omega^2}E(\omega)e^{-i\omega t} + c.c. \qquad (2.10)$$

which suggests sinusoidal behaviour in time with increasing polarisation as the frequency approaches the natural frequency of the oscillator.

For the nonlinear case Eq. 2.8 is modified by including anharmonic terms such that

$$\frac{d^2r}{dt^2} + 2\gamma\frac{dr}{dt} + \omega_0^2 r + ar^2 = -\frac{e}{m}E \qquad (2.11)$$

where only the lowest anharmonic term has been included. Usually this is solved by assuming that the anharmonic terms have a much smaller contribution to the polarisation than the linear term. The solution becomes a power series in the displacement r. This equation can only be solved at specific frequencies. That is, we can determine the response at, for example, $2\omega_1$ giving

$$r^{(2)}(2\omega_1) = -\frac{a(e/m)^2 E_1^2}{(\omega_0^2 - 4i\gamma\omega_1 - (2\omega_1)^2)(\omega_0^2 - i\gamma\omega_1 - \omega_1^2)^2} \qquad (2.12)$$

so the response can be found for the particular combinations of frequencies that are of interest. Using $P = -Ner$ we can now find the polarisation in terms of this response function for a particular frequency term. That is $P^{(2\omega)}$

can be expressed as

$$P^{(2\omega)} = \frac{Ne^3/m^2a}{(\omega_0^2 - 4i\gamma\omega_1 - (2\omega_1)^2)(\omega_0^2 - i\gamma\omega_1 - \omega_1^2)^2} \qquad (2.13)$$

For semiconductors and nonconjugated systems this model works well. However for highly conjugated systems the electrons that contribute most to the nonlinearity are not localised so cannot be thought of as point oscillators. For these systems a different approach must be used, where the concept of microscopic nonlinearity is introduced.

2.4 Microscopic Nonlinearity

Organic systems such as crystals and dilute solutions consist of molecular units that in general only interact weakly. That is they are usually neutrally charged and there is usually little intermolecular charge transfer [18]. Therefore an oriented gas model has often been used to relate the microscopic nonlinearities to the macroscopic susceptibilities. In a similar way as for the macroscopic polarisation it is possible to write an expression for the microscopic polarisation in terms of a power series.

$$\begin{aligned} p(\omega) &= \alpha(\omega) \cdot E(\omega) + \beta(-\omega; \omega_1, \omega_2) \cdot E(\omega_1)E(\omega_2) + \\ &\quad \gamma(-\omega; \omega_1', \omega_2', \omega_3') \cdot E(\omega_1')E(\omega_2')E(\omega_3') + \dots \end{aligned} \qquad (2.14)$$

The microscopic tensors $\alpha(\omega)$, $\beta(-\omega; \omega_1, \omega_2)$, and $\gamma(-\omega; \omega_1', \omega_2', \omega_3')$ have the same properties as their macroscopic counterparts in terms of symmetry. This is expressed in the usual notation for the dependence of the susceptibility on the frequency. The negative sign is for a photon "emitted" and the positive

for one "absorbed", where the photon emitted is the sum of those absorbed. Similarly for centrosymmetric molecules β vanishes as in the case of the macroscopic susceptibility $\chi^{(2)}$ for centrosymmetric solids.

2.5 Coupled Anharmonic Oscillator Model

This model, originally proposed by Bloembergen [6] and extended by Prasad [45], is similar to the anharmonic oscillator model. In this case each oscillator is a linearly coupled chain of simple anharmonic oscillators which is an attempt to represent conjugated molecules and polymers. Compared to the non–coupled model each oscillator is of a higher level system in that each monomeric unit is considered an oscillator, and not just a single electron. The first and second hyperpolarisabilities are represented by quadratic and cubic terms added to the standard equation of motion. To represent the π–electron delocalisation over the whole system a single coupling constant, k is used. The model also assumes a single resonant frequency ω_0. This simple model is solved in the same way as for the non–coupled model, where the displacement r is solved for and from the expansion of the dipole moment, the polarisabilities found.

When compared to experimental values this model confirms the power law increase in polarisability with repeat unit number [45]. The advantages of this model are that a single molecule's large nonlinearity can be understood, and it also explains the increase when longer chains are used to achieve greater π–electron delocalisation. The main disadvantage of this model is that only a single resonant frequency is used. This is where recourse must be given to the quantum mechanical approach, as here each atom can have

many different energy levels or equivalently, different resonant frequencies.

2.6 Quantum Mechanical Approach

There are two main methods, the derivative and the sum over states method. We shall confine ourselves to the sum over states, SOS, method as this has been applied most successfully to the study of larger conjugated systems such as those studied here [46].

The SOS approach was developed to account for the electron movement under an applied electromagnetic field for the molecule of interest. Under the oscillating field the electrons will oscillate, in turn generating oscillating currents. The polarisation of the molecule, caused by the induced oscillating dipole can be expressed as a perturbation to the state of the system by the field.

This results in an expression for the polarisability and hyperpolarisabilities as infinite sums over the various excited states where, for example the molecular second harmonic coefficient is given as

$$\beta(-2\omega;\omega,\omega) = p \sum_{n_1,n_2} \left(\frac{e^3}{2\hbar^2}\right) \frac{r_{gn_2} r_{n_2 n_1} r_{n_1 g}}{(\omega - \omega_{n_1 g})(2\omega - \omega_{n_2 g})} \qquad (2.15)$$

in which g is the ground state, n are the various excited states, $\omega_{ng} = \omega_n - \omega_g$, and p indicates that summations are to be carried out over all permutations of the Cartesian indices (i, j, k), and r is the coordinate associated with electron position (cf. Fig 2.1 [2]). It is possible to consider the molecular properties by approximating the SOS approach to two levels [20]. Eq. 2.15
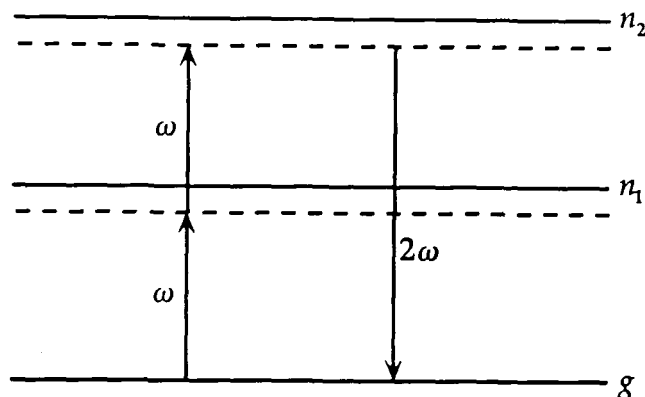
Figure 2.1: Energy Level Diagram

then simplifies to

$$\beta(-2\omega;\omega,\omega) \cong \frac{3e^2}{2\hbar m} \cdot \frac{\omega_{eg} f \Delta\mu}{\left(\omega_{eg}^2 - \omega^2\right)\left(\omega_{eg}^2 - 4\omega^2\right)} \qquad (2.16)$$

in which ω_{eg} is the angular frequency of the optical transition, f is the oscillator strength (related to the transition moment between ground and excited state dipole moment i.e. $\langle g|er|n\rangle^2$), and $\Delta\mu$ is the difference between the ground and excited state dipole moment.

2.7 Macroscopic to Microscopic

The macroscopic formalism used assumes that the molecular assembly is acted on by the macroscopic field that appears in Maxwell's equations. However each molecule in the ensemble is acted on, not by this macroscopic field but a local field, often referred to as the Lorentz local field. In relating any macroscopic polarisation measured to a microscopic property such as a β tensor component a ratio of the local field to the macroscopic field must be

used. This ratio is a combination of local field factors, one for each of the

frequency interactions.

The local field is the sum of the field acting on a molecule due to all

external sources and the external field. This is found by considering a small

sphere centred on the molecule [47], that is large enough to enable the field

at the centre, due to the other molecules to cancel. This allows the field

at the centre due to the molecule of interest to be calculated. In general,

when less symmetrical systems, such as poled polymers are considered, the

cavity surrounding the molecule is taken to be an ellipsoid. In this case the

relationship between the local field $E_l(\omega)$ and the macroscopic field $E(\omega)$ can

be written [26]

$$E_l(\omega) = E(\omega) + 4\pi L P(\omega) \qquad (2.17)$$

where L is a tensor whose elements are determined by the shape of the cavity

surrounding the molecule [24], and $P(\omega)$ is the dipole density. For a spherical

cavity $L_1 = L_2 = L_3 = \frac{1}{3}$. In the case of a linear dielectric the local field

factor $f(\omega)$ can be represented by

$$f(\omega) = 1 + \frac{\epsilon_\omega - 1}{L} \qquad (2.18)$$

which for an isotropic liquid gives

$$f(\omega) = \frac{\epsilon_\omega + 2}{3} \qquad (2.19)$$

However this only applies to induced dipoles, but under the action of a static

field the dipole can also be oriented. This case, first described by Onsager

[48] gives a zero frequency correction factor:

$$f(0) = \frac{\epsilon_0 \left(\epsilon_\omega + 2\right)}{2\epsilon_0 + \epsilon_\omega} \tag{2.20}$$

Using this definition of local field factors the linear case can be extended to the nonlinear terms, giving

$$\chi^{(1)}(\omega) = f(\omega) N \alpha(\omega) \tag{2.21}$$

$$\chi^{(2)}(-\omega; \omega_1, \omega_2) = f(\omega) f(\omega_1) f(\omega_2) N \beta(-\omega; \omega_1, \omega_2) \tag{2.22}$$

$$\chi^{(3)}(-\omega; \omega_1', \omega_2', \omega_3') = f(\omega) f(\omega_1') f(\omega_2') f(\omega_3') N \gamma(-\omega; \omega_1', \omega_2', \omega_3') \tag{2.23}$$

For the special case of electric field induced second harmonic we can write

$$\chi^{(3)}(-2\omega; \omega, \omega, 0) = f(2\omega) f^2(\omega) f(0) N \gamma(-2\omega; \omega, \omega, 0) \tag{2.24}$$

where

$$f(\omega) = \frac{n_\omega^2 + 2}{3}$$

$$f(2\omega) = \frac{n_{2\omega}^2 + 2}{3}$$

and

$$f(0) = \frac{\epsilon_0 \left(n_\omega^2 + 2\right)}{2\epsilon_0 + n_\omega^2} \tag{2.25}$$

which gives a total local field factor in an isotropic solution with an applied field, as used in EFISH experiments, of

$$f(2\omega) f^2(\omega) f(0) = \frac{\epsilon_0 \left(2 + n_\omega^2\right)^3 \left(n_{2\omega}^2 + 2\right)}{27 \left(2\epsilon_0 + n_\omega^2\right)} \tag{2.26}$$

(cf. Eq. 4.23).

The expression 2.24 implies that any orienting field applied to the system gives perfect alignment. However the situation is more complex with further mapping between laboratory and molecular reference frames requiring further explanation (cf. § 4.2.2).

2.8 Propagation of the Second Harmonic

An explanation is given here of the propagation of the second harmonic wave, as this is most pertinent to the experiments carried out in the present study. This requires an analysis of Maxwell's equations which describe the propagation of electromagnetic waves. [43].

In a nonmagnetic medium the wave equation for propagation of an electric field and its induced polarisation can be stated

$$\nabla^2 E = \frac{\partial^2}{\partial t^2}\left(\frac{\epsilon}{c^2}E\right) - \frac{4\pi}{c^2}\frac{\partial^2 P}{\partial t^2} \qquad (2.27)$$

where the linear polarisation is included in ϵ, and P is only the nonlinear polarisation. For clarity this is restricted to the one dimensional case by setting $\partial/\partial y = \partial/\partial x = 0$, therefore assuming propagation in the z direction. For the analysis of $\chi^{(2)}$ we are only interested in the interaction of three waves, two at the fundamental and the resulting harmonic. This gives three interacting travelling waves of the form

$$E_1(z,t) = E_1(z)e^{i(\omega_1 t - k_1 z)} \qquad (2.28)$$

$$E_2(z,t) = E_2(z)e^{i(\omega_2 t - k_2 z)} \qquad (2.29)$$

$$E_3(z,t) = E_3(z)e^{i(\omega_3 t - k_3 z)} \qquad (2.30)$$

From Eq. 2.2 we get

$$P_1(z,t) = 2\chi^{(2)}E_2^*(z)E_3(z)e^{i[(\omega_3-\omega_2)t-(k_3-k_2)z]} \qquad (2.31)$$

$$P_2(z,t) = 2\chi^{(2)}E_3(z)E_1^*(z)e^{i[(\omega_3-\omega_1)t-(k_3-k_1)z]} \qquad (2.32)$$

$$P_3(z,t) = 2\chi^{(2)}E_1(z)E_2(z)e^{i[(\omega_1+\omega_2)t-(k_1+k_2)z]} \qquad (2.33)$$

where all the amplitudes are dependent on each other, and so a general solution is not trivial. If the assumption is made that the harmonic generated is small enough not to deplete the fundamental then the three equations reduce to one, and can be solved to give, in the second harmonic generation case [39]

$$E^{2\omega}(z) = E_\omega e^{ik_f z} + \frac{16\pi\omega^2}{c^2\left(k_f^2 - k_b^2\right)}\chi^{2\omega}E_\omega^2 e^{ik_b z} \qquad (2.34)$$

where $k_f = \frac{2\omega}{c}n_{2\omega}$, and $k_b = \frac{2\omega}{c}n_\omega$ and f represents the free wave and b represents the bound wave. The free wave is that generated at the boundary of the nonlinear medium, and the bound wave travels with the fundamental. This implies that two waves of differing phase velocities are propagating in the nonlinear medium.

If this equation is used to set the boundary conditions in a nonlinear medium, solving for $E_f^{2\omega}$ gives

$$E_f^{2\omega} = \frac{TE_b(e^{i(k_b-k_f)l} - 1)}{k_b - k_f} \qquad (2.35)$$

where T are Fresnel like factors (cf. Oudar [20]). This means that the second harmonic intensity given by $\left|E_f^{2\omega}\right|^2$ is

$$I^{2\omega} \propto T^2 16\pi^2 \left(\frac{2\omega}{c}\right)^4 (I^\omega)^2 \chi^{2\omega}\frac{\sin^2(\Delta k l_c/2)}{(\Delta k)^2} \qquad (2.36)$$

where l_c is the coherence length defined as the length over which ω and 2ω dephase by π. With a medium of known χ under the same I^ω, I^ω can be cancelled and a χ value for an unknown material can be determined relative to, for example, quartz. For the case of EFISH much the same analysis is carried out except that the number of boundaries encountered is increased (cf. § 4.2.5 for a more detailed discussion).

Chapter 3

Material Systems

3.1 Introduction

For molecules of interest in nonlinear optics the molecule must be readily polarised, which means that the electrons must be free to move around the molecule. If a system is made up from alternate single and double bonds in a chain or a ring system the π–electrons can become completely delocalised and move over the complete conjugation length. For quadratic nonlinearity the systems must be noncentrosymmetric so a general system would be one with an electron donor separated from an electron acceptor by a conjugated system. This type of charge transfer system was first mention by Davydov [18] where the length of the conjugation [46] was found to be proportional to $\sqrt[3]{\beta}$. Since sufficient $2p_z$ orbital overlap is required for delocalisation of π–electrons it follows that planar molecules should provide higher β values than nonplanar molecules.

3.2 General Properties

A general framework for determining those molecules with high β values, and therefore promising candidates for nonlinear optics, has been established. However there are many compromises that have to be considered for materials to be of practical importance.

The λ_{max} tends to increase as the extent of conjugation and the hyper-polarisability increase so for frequency doubling into, for example the blue, most materials absorb and so cannot be used. Materials with a low enough absorption tend not to possess a large enough nonlinear coefficient to be practical.

Material stability can also be a problem for molecules with the highest nonlinearity as they tend to be more reactive. For the high coefficient systems waveguide configuration can help as long interaction lengths can negate the need for high laser power.

For bulk nonlinear optical applications there is the additional problem of crystal structure, in that noncentrosymmetric molecules may crystallise in a centrosymmetric manner. This is quite likely as these polar molecules will prefer to align head to tail. Various synthesis strategies have been employed to overcome this.

- low dipole moment eg. POM [26]

- octupolar molecules [49]

- hydrogen bonding eg. DAN [50]

- attachment to polymer chains

- doping into polymers

In electro–optic applications organics have the advantage over inorganics in that they possess a low dielectric constant and hence a low RC time constant so high switching speeds are possible $\approx 10GHz$. Also there is little dispersion between ϵ', the real part of the dielectric constant, at low frequency and at optical frequency (n^2) so travelling wave devices have less phase matching problems in comparison to inorganics.

3.3   Systems Studied

In this study four main compounds were studied for molecular β. These were:

- 2–methyl–4–nitroaniline (MNA)

- N–(4–nitrophenyl)–(L)–prolinol (NPP)

- 2–(N,N–dimethylamino)–5 –nitroacetanilide (DAN)

- Z–β [(N,N'–diethylmethylimmonium)–α–cyano–4– styryldicyanometh-anide] (DEMI)

where these structures can be seen in figure 3.1

3.3.1   MNA

MNA contains a typical donor–acceptor pair of groups separated by a conjugated system. The donor group is NH_2 and the acceptor group is NO_2 with the aromatic ring separating the two as the conjugated system. This molecule has been extensively studied [51, 52, 53] and for this reason was chosen as a standard in this work. The CH_3 group on the ring lowers the molecular
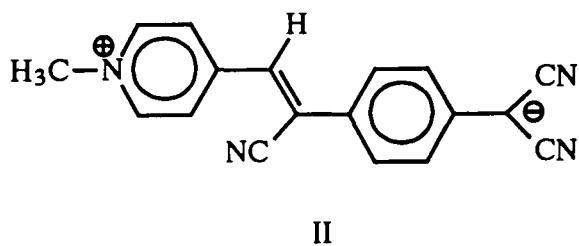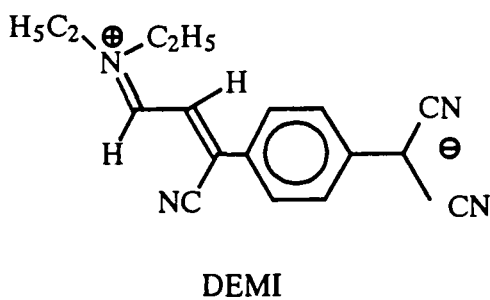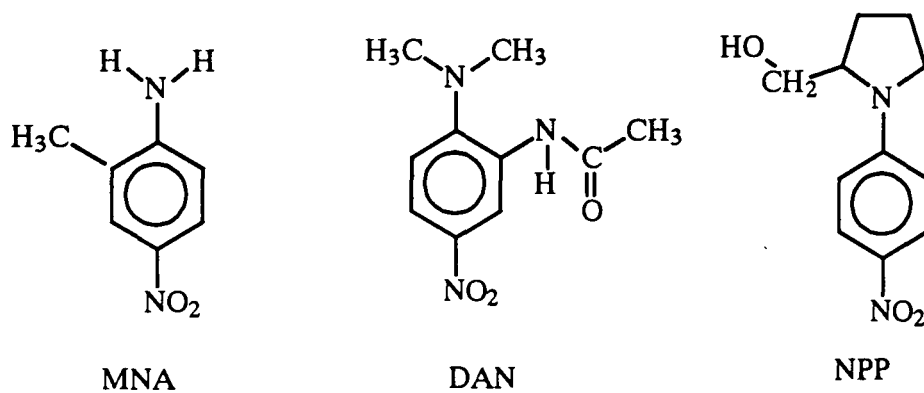
Figure 3.1: Materials Investigated

nonlinearity as it increases the dimensionality of the system but is necessary for maintaining the bulk nonlinearity. This gives a crystal structure that is monoclinic which is one of the more favourable point groups [54].

3.3.2 NPP

NPP is a derivative of MNA where the molecule was designed for optimal phase–matching of second harmonic in the bulk [27]. The strategy was two fold, a combination of chirality and hydrogen bonding to ensure optimal crystal structure. In fact the chromophore is oriented at 58.6° in the unit cell very close to the optimum of 54.74°. Noncritical phase matching was demonstrated [55] at 1.3 μm.

3.3.3 DAN

DAN has been extensively studied for its bulk properties [33, 56, 32]. Its donor group is NMe_2 and its acceptor group is NO_2. The $-NHCOCH_3$ substituent is very important in maintaining the energetically unfavourable dipole alignment through hydrogen bonding for bulk crystals. Hydrogen bonding has also been shown to enhance stability in relaxation of poled polymers [50]. The alignment of 70.8° [33] gives a high projection of β onto the crystallographic axes.

3.3.4 DEMI

This molecule has been shown to be planar [57] with a delocalised π–electron system and is also fairly long which should lead to a high β value. Due to its zwitterionic nature a high dipole is expected. The minus charge on the
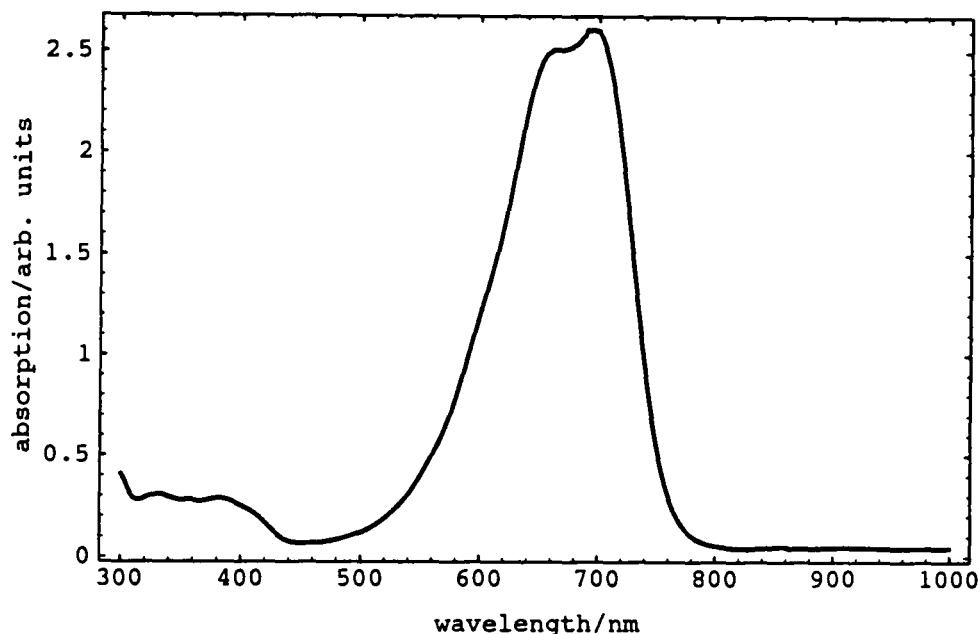
Figure 3.2: Absorption Spectrum of DEMI in DMF

carbon adjacent to the aromatic ring is distributed onto the ring giving rise to more delocalisable charge enhancing the nonlinearity. The main advantage for this material is its high nonlinearity coupled to its transparency range and through Kramers–Kronig relation its expected anomalous dispersion. This acts over the range 950 → 475 *nm* ideal for doubling near IR diode lasers into the blue (cf. Fig. 3.2). The crystal structure of DEMI is a head to tail arrangement of dimers, not surprising in view of the high dipole moment. Doped film SHG and EFISH measurements suggests that dimers are not formed in great numbers in dilute systems which is possibly due to screening effects in polar solvents. This is the first in a new class of molecules of great promise. The material called II in table 6.2 is a derivative of DEMI and the μ and β measurements which follow are the first made on such highly dipolar molecules [58].

3.4 Polymers

The polymers used in the device sections of this work were:

- Polymethyl methacrylate (PMMA)

- Polyvinyl alcohol (PVA)

- Telene

- Polyvinyl chloride (PVC)

- Poly–4–vinyl pyridine (P4VP)

- Bis–phenol–A polycarbonate (PC)

Except Telene which is manufactured by BF Goodrich all of these are commercially available through the Aldrich Chemical Company. The particular polymers used depend to a large on the intended application and those chosen for this work fulfilled the compatibility requirements for the devices studied. This is described in greater detail in Chapters 5 and 7.

Chapter 4

Experimental Methods: Molecules

4.1 Introduction

In determining the usefulness of a molecular material for photonics a set of its fundamental properties has to be known.

With integrated optics in mind, an example device of interest could be a frequency doubler waveguide, where important fundamental properties of the nonlinear molecule would certainly include:

- Favourable linear absorption spectrum

- High dipole moment: μ

- High first hyperpolarisability (resonant: β_ω and static: β_0)

The linear absorption spectrum determines the frequency regime within which the device can operate. This information is important in calculating both β_ω and β_0 as will be pointed out later.

The absorption spectrum is easily measured with a spectrophotometer and knowing the path length of the solution the absorption coefficient α measured in units of cm^{-1} can be calculated for any wavelength of interest. In this case a Perkin Elmer Lambda 9 with a working range of $170 \rightarrow 3700$ nm was used.

The dipole moment is necessary when using electric field induced second harmonic generation (EFISH) to determine the nonlinearity β as EFISH only gives the $\mu\beta$ product.

In the case of the dipole moment of a molecule an HP LCR meter with a standard bridge attachment was used. This gives the capacitance of the bridge where the concentration dependence of the capacitance enables determination of the dipole moment. Placing a spectrometer cell between the plates of the bridge can give the capacitance of the solution in the cell, after calibration of both the bridge and the cell, cf. § 4.2.5.

The first hyperpolarisability was determined using the technique of EFISH [59]. This was performed at one of two primary wavelengths depending on the linear absorption of the medium using apparatus constructed for this study.

4.2 Electric Field Induced Second Harmonic

4.2.1 Introduction

The technique of electric field induced second harmonic generation [60, 61, 62, 63, 21, 51], enables the generation of second harmonic fields in isotropic materials, and operates through a third order process requiring an applied static electric field to break the symmetry. This section describes the theory

behind EFISH, and gives a description of the data reduction methods which allow the molecule's microscopic second order susceptibility to be calculated.

4.2.2 Theory

When an isotropic material, where the dipole moment approximation is valid, is subjected to a static electric field, E^0 it becomes anisotropic and noncentrosymmetric with respect to the polarisation. When irradiated with a laser of frequency ω, a microscopic polarisation $p^{2\omega}$ is induced in each molecule, according to:

$$p_i^{2\omega} = \beta_{ijk} E_j^\omega E_k^\omega + \gamma_{ijkl} E_j^\omega E_k^\omega E_l^0 \qquad (4.1)$$

where i, j, k, l, refer to molecular axes (x, y, z), β_{ijk} is the second hyperpolarisability and γ_{ijkl} is the third [20, 22]. The Einstein summation convention is used here as stated in §2.2. On the macroscopic scale, as measured by EFISH the average nonlinearity, Γ_{IJKL}^0 is obtained, where $\Gamma_{IJKL}^0 E_L^0$ may be taken to be the effective second harmonic susceptibility of the liquid. I, J, K, L, are taken to be the laboratory reference frame axes (X, Y, Z)[21]. If we assume that we are far from resonance, it is then possible to invoke Kleinman symmetry [37] and therefore, due to the liquid isotropy in the absence of an external field, Γ_{IJKL}^0 has only one independent component [21]. If the molecule is one dimensional and the ground state dipole moment μ is aligned along the molecular z axis, Γ_{ZZZZ}^0 is given by [51, 21, 59]

$$\Gamma_{ZZZZ}^0 \equiv \Gamma_L^0 = N f^0 (f^\omega)^2 f^{2\omega} \left(\gamma + \frac{\beta_z \mu}{5 k_B T} \right) \qquad (4.2)$$

where k_B is Boltzmann's constant, T is temperature, N is the number of molecules per unit volume, f represents local field corrections, β_z is the vector

$$\beta_X = \beta_{zzz} \sin\theta\cos\phi$$
$$\beta_Y = \beta_{zzz} \sin\theta\cos(90-\phi) = \sin\theta\sin\phi$$
$$\beta_Z = \beta_{zzz} \cos\theta$$
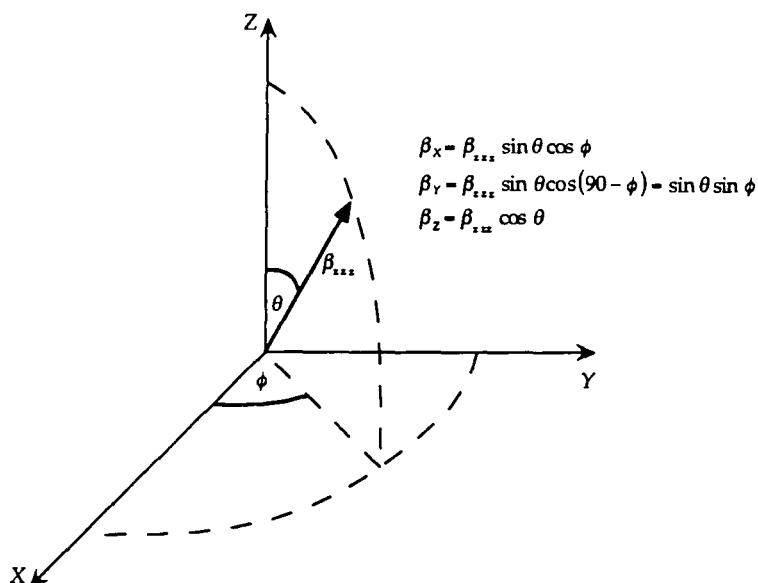
Figure 4.1: Coordinate Axes Transformations.

part of the microscopic second order susceptibility, and γ is the microscopic third order susceptibility. The factor $\mu/5k_BT$ is derived from transforming the molecular coordinates onto the laboratory axes. In general transforming a tensor from one coordinate system to another takes a direction cosine term for each rank [64]. i.e. $\cos^3\theta$ for the coefficient, β_{zzz}, projected onto the Z axis. This is more easily visualised by referring to figure 4.1

Physically we have β_{ijk} defined in a molecular coordinate system, and a polarisation response in the laboratory coordinate system due to a set of exciting fields. The β value that is accessed in EFISH is directed along the dipole moment. From Eq. 4.1 it can be seen that β interacts with two fields which are equivalent. When the primary beam is polarised along the Z axis, (E^ω), each is a $\cos\theta$ projection onto the β of the molecule. This means that each field is only interacting by $\cos\theta$ of its magnitude, giving a $\cos^2\theta$ factor for both fields. The molecule's nonlinear response is a further projection of

$\cos\theta$ onto the laboratory Z axis as long as the static field is co-aligned with the Z axis. In total there is a $\cos^3\theta$ factor between the measured response and the molecular β value.

Here the assumption is that μ and β are along the same molecular axis. In this case the work done aligning one dipole moment, where μ makes an angle θ with E_L^0, is given by $W = -\mu E_L^0 \cos\theta$ [24] and the interaction with other dipoles is neglected. In this analysis, due to the presence of other dipoles in a liquid, the field experienced will not be E_L^0 but some other field, the local field E_l^0 as described in § 2.7, whose average is still in the same direction, giving $W = -\mu E_l^0 \cos\theta$.

Without a field the number of dipoles inclined to the z axis and distributed evenly between θ and $d\theta$ is

$$dN = N\frac{2\pi r \sin\theta r d\theta}{4\pi r^2} = \frac{1}{2}N\sin\theta d\theta \qquad (4.3)$$

According to Boltzmann's energy distribution law, the dipole distribution is nonuniform under a uniform applied field. To find the number of dipoles which are aligned a distribution function has to be introduced, giving

$$dN = Ae^{\frac{\mu E_l^0 \cos\theta}{k_B T}} \cdot \frac{1}{2}N\sin\theta d\theta \qquad (4.4)$$

where A is some constant. Under the applied field, E_l^0 and at some temperature T we can calculate $\langle\cos\theta\rangle$ which is the average value of $\cos\theta$. If all the dipoles are aligned along E_l^0 then $\langle\cos\theta\rangle = 1$, and if there is a random

orientational distribution then $\langle \cos\theta \rangle = 0$. From Eq. 4.4 we get

$$\langle \cos\theta \rangle = \frac{\int_0^\pi \cos\theta \cdot e^{\frac{\mu E_l^0 \cos\theta}{k_B T}} \cdot \frac{1}{2}N \sin\theta d\theta}{\int_0^\pi e^{\frac{\mu E_l^0 \cos\theta}{k_B T}} \cdot \frac{1}{2}N \sin\theta d\theta} \tag{4.5}$$

However this only gives the polar alignment and it is the relationship between β_z and the macroscopic susceptibility Γ_{ZZZZ} that is needed.

This is achieved by modifying Eq. 4.5 to introduce $\langle \cos^3\theta \rangle$. Eq. 4.5 becomes

$$\langle \cos^3\theta \rangle = \frac{\int_0^\pi \cos^3\theta \cdot e^{\frac{\mu E_l^0 \cos\theta}{k_B T}} \cdot \frac{1}{2}N \sin\theta d\theta}{\int_0^\pi e^{\frac{\mu E_l^0 \cos\theta}{k_B T}} \cdot \frac{1}{2}N \sin\theta d\theta} \tag{4.6}$$

Using the substitutions $x = \mu E_l^0 \cos\theta / k_B T$ and $a = \mu E_l^0 / k_B T$ we get

$$\langle \cos^3\theta \rangle = \frac{\int_a^{-a} \cos^3\theta \cdot e^x \cdot dx}{\int_a^{-a} e^x \cdot dx} \tag{4.7}$$

the substitution $\frac{x^3}{a^3} = \cos^3\theta$ is made to enable the $\cos^3\theta$ term to be eliminated so that the integration becomes manageable.

$$\Rightarrow \langle \cos^3\theta \rangle = \frac{\frac{1}{a^3}\int_a^{-a} x^3 \cdot e^x \cdot dx}{\int_a^{-a} e^x \cdot dx} \tag{4.8}$$

Integrating by parts gives

$$\frac{(e^a + e^{-a})\left(1 + \frac{6}{a^2}\right)}{e^a - e^{-a}} - \frac{3}{a} - \frac{6}{a^3} = \coth(a)\left(1 + \frac{6}{a^2}\right) - \frac{3}{a} - \frac{6}{a^3} \tag{4.9}$$

Expanding this as a series leads to

$$\frac{a}{5} - \frac{a^3}{105} + \frac{4a^5}{4725} - \cdots \qquad (4.10)$$

Taking the first term in the series, which is within the errors for the overall calculation, the factor transforming the molecular hyperpolarisability to the macroscopic susceptibility is $\mu_z E_l^0/5k_B T$. Specifically, Eq. 4.1 can be changed to

$$p_i^{2\omega} = \left(\frac{\beta_{ijk}}{E_l^0} + \gamma_{ijkl}\right) E_j^\omega E_k^\omega E_l^0 \qquad (4.11)$$

This enables the local field in the alignment factor to cancel giving

$$p_i^{2\omega} = \left(\frac{\mu\beta_z}{5k_B T} + \gamma_{ijkl}\right) E_j^\omega E_k^\omega E_l^0 \qquad (4.12)$$

The macroscopic susceptibility can be related to the microscopic hyperpolarisability by the expression [20]

$$\Gamma_{ZZZZ} = Nf\gamma \qquad (4.13)$$

where f is taken to represent all the local field correction terms and γ can be represented with reference to Eq. 4.12 [59, 20] by

$$\gamma = \frac{\mu\beta_z}{5k_B T} + \gamma_{ijkl} \qquad (4.14)$$

Upon substitution of Eq. 4.14 into Eq. 4.13, the familiar Eq. 4.2 is returned. In general, for conjugated molecules such as those studied here, and in line with previous studies, [65, 20, 23, 49, 51] $\gamma_{ijkl} \ll \mu\beta_z/5k_B T$ is neglected so that, if Γ_0 is known the β_z for the liquid can be determined.

4.2.3 Experimental Technique

The method used to measure Γ_L is the Maker fringe wedge technique [66, 67, 68]. In the specific case of a two component solution, Γ_L is the sum of the solvent, Γ_0 and solute, Γ_1 contributions and is expressed as [51]

$$\Gamma_L = N_0 f_0^0 \left(f_0^\omega\right)^2 f_0^{2\omega}\gamma_0 + N_1 f_1^0 \left(f_1^\omega\right)^2 f_1^{2\omega}\gamma_1 \qquad (4.15)$$

where γ_i ($i = 0, 1$) is defined as $\gamma_i = \mu_i\beta_i/5k_BT$. Here a wedge shaped material is translated normal to the incident laser radiation. When the wedge is translated the optical path length changes and a pattern of interference fringes is observed due to the differing relative phases of the bound and free harmonic waves being accessed.

In the case of liquids and solutions subject to a static, symmetry breaking field, the wedge is defined by bounding input windows set at such an angle to generate a reasonable number of fringes. The liquid cell design [23, 20, 51, 21] is shown in figures 4.2 and 6.15. The field profile in this particular arrangement is shown in figure 4.3. The cell is made from stainless steel and PTFE insulation. The windows are fabricated to an angle of 2° from Schott BK7 glass, rather than fused silica which can produce second harmonic without an applied field simply due to microcrystalline regions [21]. These glass windows are placed in predefined PTFE grooves to aid assembly. The whole arrangement is placed in a large spectrometer cell [21] (supplied by Hellma Inc.) for ease of filling and held in place with a PTFE lid. Once filled, in a nitrogen atmosphere, the cell is sealed so that the solvent does not absorb water [69].

For the experiment (cf. figure 4.4) a Nd:YAG (10 Hz with pulse duration
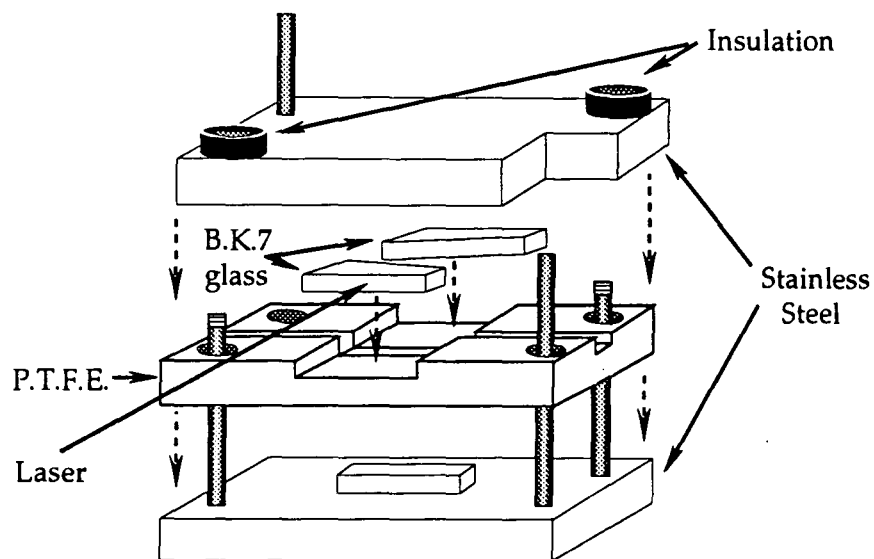
Figure 4.2: Cell (1.064 μm Design)
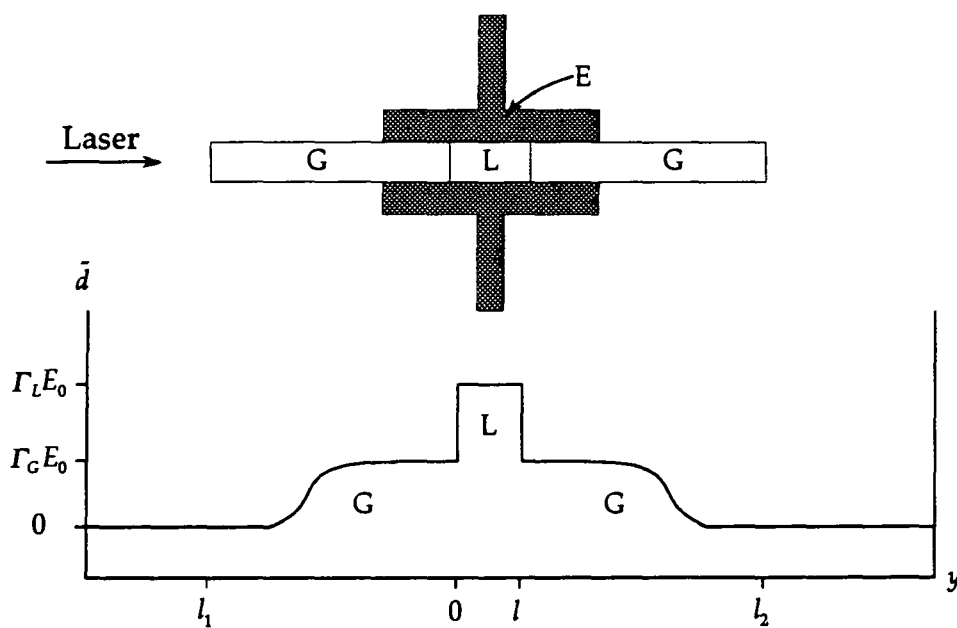
Figure 4.3: Field Profile of EFISH Cells. E = Electrode, G = Glass, L = Liquid

8 nm) source is employed lasing at 1.064 μm to produce a second harmonic at 532 nm. This is polarised vertically with respect to the electrodes in the sample cell, and brought to a focus approximately in the centre of the wedge. A digital delay generator controls the timing of the applied static field, the laser pulse, and the data acquisition. With the inclusion of a reference to the fundamental wavelength any fluctuations in the incident energy can be minimised. A further refinement is applied through shot to shot averaging, where the computer divides the signal by the square of the reference and this value is averaged. The reference is provided by a fast response silicon photodiode (rise time 500 ps) with appropriate neutral density filters. This is set at a glancing angle so that the reflectance for the two orthogonal polarisations is the same [70]. The second harmonic is detected with a photomultiplier tube which is prefiltered with a short pass KG3 filter and a 532 nm band pass interference filter. The sample is mounted on a computer controlled translation stage which can be set down to 1 μm steps. To obtain quantitative measurements a reference quartz wedge oriented to access the d_{11} tensor component is measured.

The experiment performed at 1.907 μm is similar but with some important differences. This wavelength is provided by pumping a Raman shifter with 1.064 μm and picking off the first Stokes line from H_2. Filtering has to be more careful in this configuration as the second harmonic (954 nm) and the primary beam (1.064 μm) are relatively close. Most of the primary beam is filtered with a dielectric stack mirror which only reflects 1.064 μm, and the rest is picked off in the Raman shifter with a dispersing prism, and a pair of widely spaced slits. A holographic filter that blocks 954 nm is also included because there is a large amount of second harmonic generated in the Raman
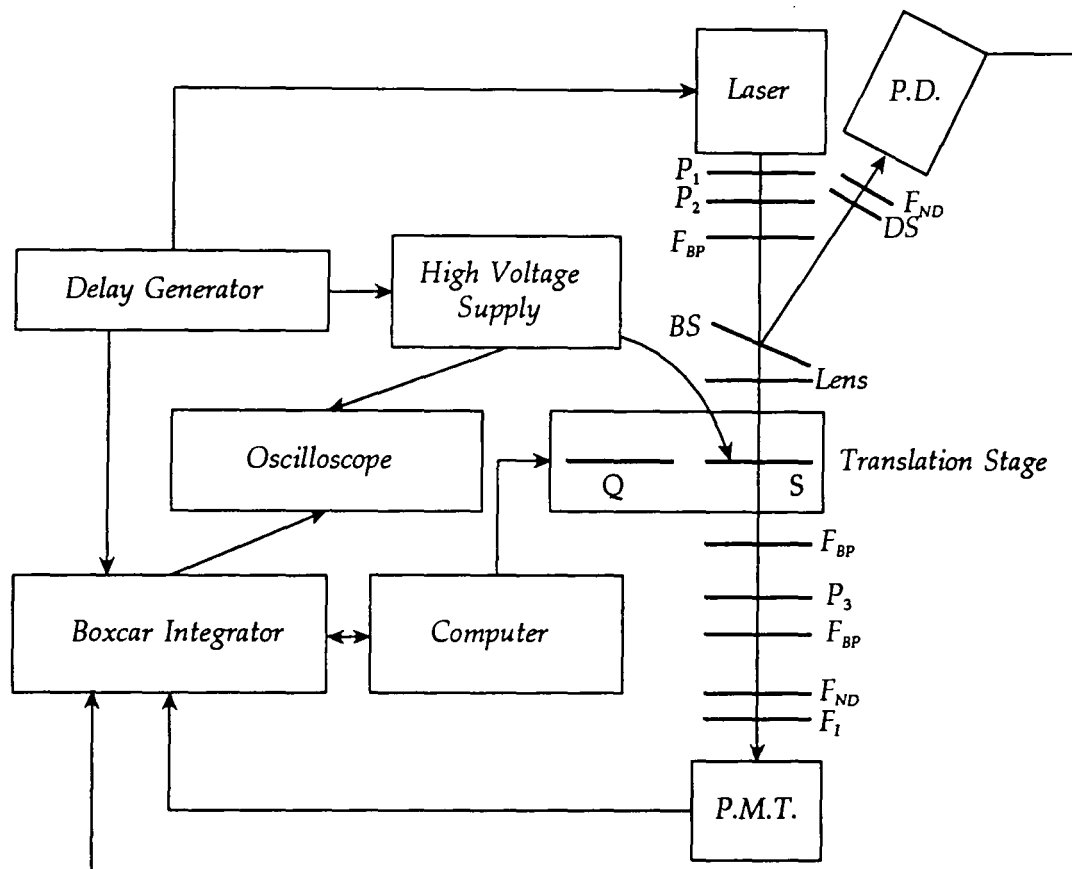
Figure 4.4: 1.064 μm Setup. P=Polariser, F=Filter, BS=Beam Splitter, DS=Diffusion Screen, BP=Band Pass Filter, ND=Neutral Density Filter, I=Interference Filter, Q=Quartz, S=Sample

shifter which would swamp the signal generated by the EFISH cell.

The reference this time is provided from the second harmonic generated by a powdered NPP sample. This is because none of the detectors available could detect 1.907 μm directly, but the S1 response photomultiplier tubes can detect the second harmonic at 954 nm. An added benefit is that the signal can now be divided directly by the reference signal value instead of the square of this.
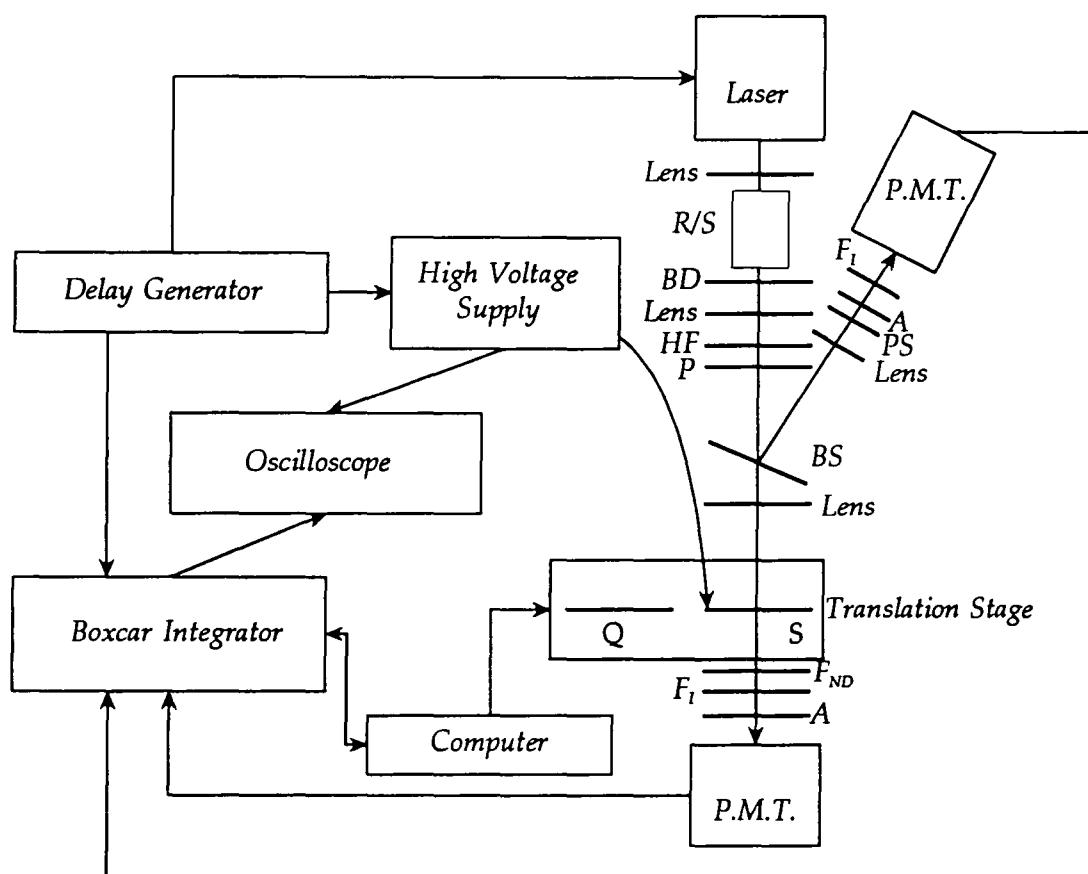
Figure 4.5: 1.907 μm Setup. R/S=Raman Shifter, BD=Beam Dump, HF=Holographic Filter, A=Aperture, P=Polariser, F=Filter, BS=Beam Splitter, PS=Powder Sample, BP=Band Pass Filter, ND=Neutral Density Filter, I=Interference Filter, Q=Quartz, S=Sample
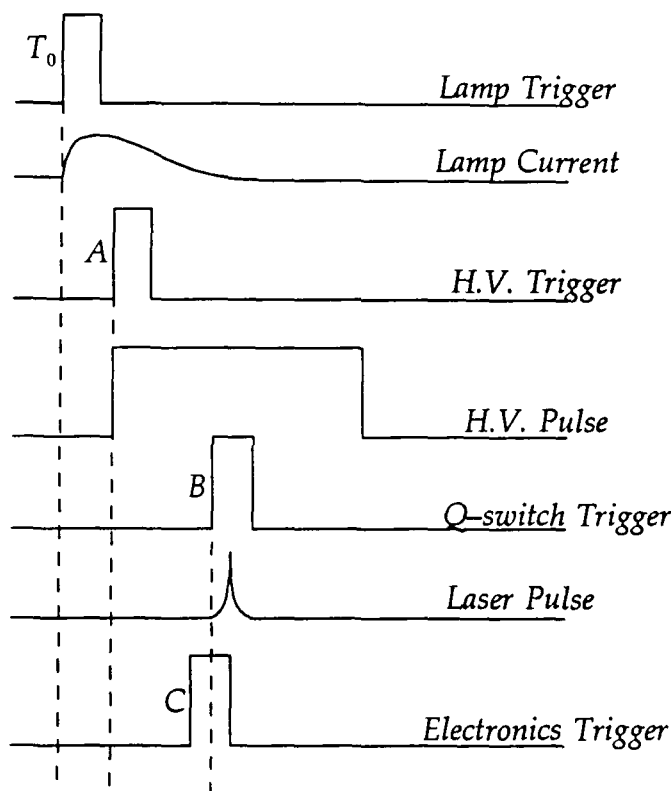
Figure 4.6: Experiment Timing Diagram. T_0=lamp, A=d.c. supply, B=Q-switch, C=electronics trigger.

4.2.4 Data Acquisition

An IBM compatible micro computer is used for logging the data from the boxcar integrators and moving the stepper motor. The timing of the laser, d.c. power supply, and the triggering of the acquisition electronics is achieved through an internally triggered digital delay generator, according to the scheme shown in figure 4.6

At time T_0 the lamp in the laser is fired. A short time later the d.c. supply is triggered. As the d.c. supply provides a pulse of $\approx 7\ \mu s$, the field is essentially static for the duration of the laser pulse. In practice the laser pulse is chosen to be nearer the end of the d.c. pulse due to noise created by the supply at the start of the pulse. The positioning of the laser pulse is achieved

through the Q–switch delay relative to the d.c. pulse. The boxcar integrators

and the oscilloscope are triggered together at a time just before the Q–switch

trigger so that the whole of the laser signal can be captured. The oscilloscope

is used to monitor the reference, second harmonic, d.c. pulse, and the related

boxes for the reference and signal. The boxcars and the translation stage are

controlled via an IEEE standard interface [65] with an IBM compatible PC.

A schematic diagram of the data acquisition program is shown in figure 4.7.

The boxcar computer interface is arranged to store readings of the reference and second harmonic up to the averaging desired. Under direct memory access, DMA, control the readings are sent to the computer where the shot to shot averaging is performed. The translation stage then moves on the desired distance, then the boxcar is signalled to start taking the next set of readings. At the end of the run the translation stage is returned to its starting position and the data stored on the hard disc and passed to a commercial plotting program.

4.2.5   Analysis

Figure 4.3 (page 36) shows the field distribution in the cell, varying from zero at the input and output faces, and the sharp increases at both glass — liquid interfaces. The field is zero at the outer faces of the glass so these contribute negligibly to the second harmonic as no free wave is generated. However both the inner faces experience a finite field and so contribute to the total second harmonic generated. The field profile is slowly varying in the glass compared to the coherence length of the glass so the bound second harmonic is proportional to the induced nonlinearity $\bar{d}$ [20, 21]. Applying the
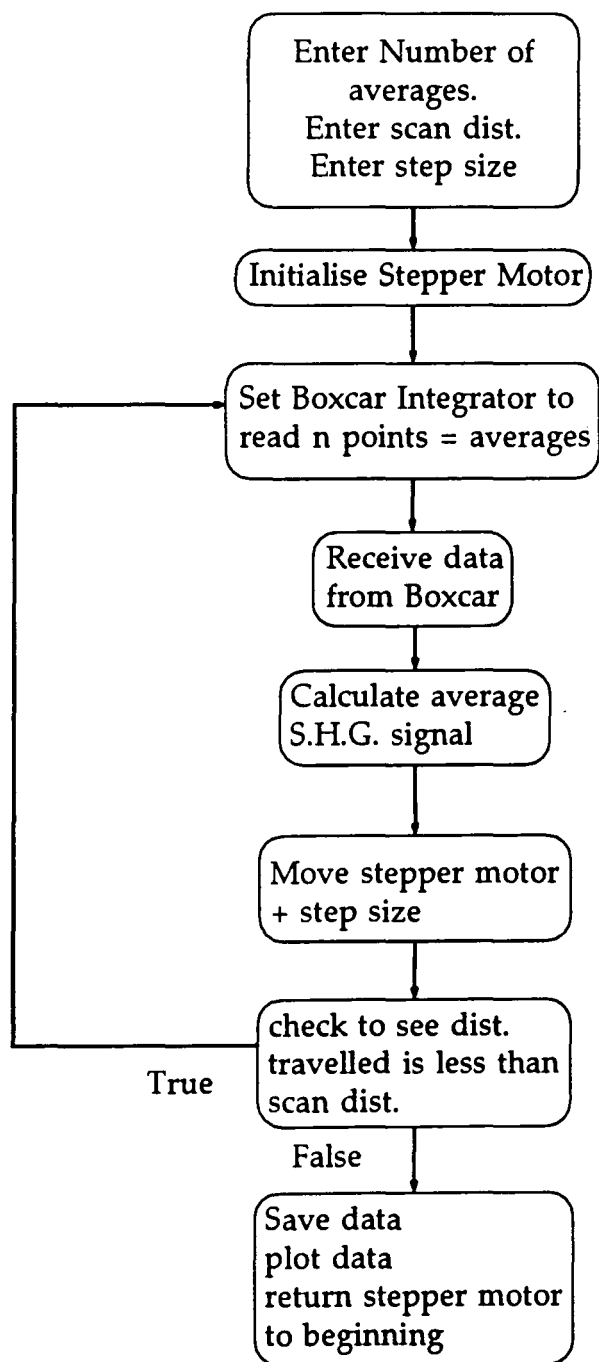
Figure 4.7: Simplified Flow Diagram of Control Program

boundary conditions to Maxwell's equation for the generation of the second harmonic [6, 67] shows that the free wave created is essentially the difference between the bound waves in the glass and the liquid. Applying the boundary conditions to each successive interface leads to the expression [20, 21]

$$\frac{A_m^L}{A_m^Q} = \frac{E_0^2 \left(T_1 \Gamma_G l_c^G - T_2 \Gamma_L l_c^L\right)^2}{\left(Q_1^2 + Q_2^2\right) d_{11}^2 \left(l_c^Q\right)^2} \tag{4.16}$$

where E_0 is the static electric field, l_c^G, l_c^Q, l_c^L are the coherence lengths of the glass, quartz and liquid respectively and Γ_G is the macroscopic susceptibility of the glass. The value of d_{11} for quartz is $1.1 \times 10^{-9} esu$ at $1.064 \ \mu m$ [71, 72].

$$T_1 = t_{2\omega}^G t_\omega^2 \frac{1}{n_{2\omega}^G + n_\omega^G} \cdot \frac{n_\omega^G + n_{2\omega}^L}{n_{2\omega}^G + n_{2\omega}^L} \tag{4.17}$$

$$T_2 = t_{2\omega}^G t_\omega^2 t_\omega' \frac{1}{n_{2\omega}^L + n_\omega^L} \cdot \frac{n_\omega^L + n_{2\omega}^L}{n_{2\omega}^G + n_{2\omega}^L} \tag{4.18}$$

T_1 and T_2 are the transmittance factors for the two boundaries under consideration [67, 51], T_1 for the glass to liquid and T_2 for the liquid to glass boundary. The transmission factors due to the different media passed through, and the equivalent factors for quartz are given by:

$$t_{2\omega}^G = \frac{2n_{2\omega}^G}{1 + n_{2\omega}^G}, \ t_\omega = \frac{2}{1 + n_\omega^G}, \ t_\omega' = \frac{2n_{2\omega}^G}{n_\omega^G + n_\omega^L} \tag{4.19}$$

$$Q_1 = \frac{2n_{2\omega}^Q}{1 + n_{2\omega}^Q} \cdot \frac{n_\omega^Q + 1}{n_{2\omega}^Q + 1} \cdot \frac{1}{n_{2\omega}^Q + n_\omega^Q} \cdot \left[\frac{2}{1 + n_\omega^Q}\right]^2 \tag{4.20}$$

$$Q2 = \frac{n_{2\omega}^Q + n_\omega^Q}{1 + n_{2\omega}^Q} \cdot \frac{1}{n_{2\omega}^Q + n_\omega^Q} \cdot \left[\frac{2}{1 + n_\omega^Q}\right]^2 \tag{4.21}$$

$A_m^{(L,Q)}$ is the mean value of the Maker fringes which is found through a Levenberg–Marquardt fit [73] to

$$y = A_1 \sin^2\left[\frac{\pi l}{2A_3} + \frac{A_4}{2}\right] \tag{4.22}$$

where $(A_1 + A_2)$ and A_2 are the maximum and minimum respectively of each measured fringe, A_3 is related to the coherence length through $A_3 = \tan\alpha/l_c$ where α is the wedge angle, and A_4 is the phase offset. Where A_m is given by $A_m = A_1/2 + A_2$. From a typical run of the experiment two sets of fringes are needed, one for the quartz reference, A_m^Q and one for the sample, A_m^L. From Eq. 4.16 which is simply quadratic when all the experimental parameters have been entered, Γ_L the only unknown, can be found. However Γ_L is still a mixture of β_0 and β_1 components (see Eq. 4.15).

It has been shown [22, 23] that by taking an infinite dilution extrapolation the solute first hyperpolarisability can be extracted. This method was developed from the formalism first applied to solution dipole moment measurements [74, 48, 41, 24]. These methods tried to minimise interactions between the solute molecules, the solvent molecules and between the two. Following the same method of accounting for these interactions by applying a concentration extrapolation to determine β, gives

$$N_A \frac{\mu\beta}{5k_B T} = \frac{27M_1\left(2\epsilon_0 + n_\omega^2\right)}{\epsilon_0\left(2 + n_\omega^2\right)^3\left(n_{2\omega}^2 + 2\right)}\left(v_0\left.\frac{\partial\Gamma_L}{\partial w}\right|_0 + \Gamma_0\left.\frac{\partial v}{\partial w}\right|_0 + \right.$$

$$\left. v_0\Gamma_0 - v_0\Gamma_0\left\{\frac{3}{n_0^2 + 1}\cdot\left.\frac{\partial n^2}{\partial w}\right|_0 + \frac{1}{\epsilon_0 + 2}\left.\frac{\partial\epsilon}{\partial w}\right|_0\right\}\right) \tag{4.23}$$

using the same local field factors for solvent and solute as dielectric constants of dissolved species are undefined [75, 20]. The error involved in this approximation was found to be less than 5%. In this study it is assumed that v_0, the specific volume, is one, $\partial v / \partial w$ is zero, and, for these very dilute solutions, that $\partial n^2 / \partial w$ is zero. n_0 is the pure solvent refractive index, Γ_0 is the pure solvent macroscopic susceptibility, and N_A is Avogadro's number. Measurements of Γ_L, and ϵ_L at several concentrations are needed to determine β. Γ_L is measured as discussed previously but ϵ_L has to be found using a separate experiment. The expression for the dipole moment as derived by Guggenheim [74, 65] is

$$\mu\,(Debye's) = \sqrt{\frac{10^{36}}{N_A} \cdot \frac{9k_B T}{4\pi} \frac{3}{(\epsilon_0 + 2)\,(n_0^2 + 2)} \cdot \left.\frac{\partial \epsilon}{\partial C}\right|_0} \qquad (4.24)$$

where C is the concentration. To determine μ the change in dielectric constant versus concentration has to be known.

The apparatus used here is an HP LCR meter at 1 KHz and 1 MHz attached to a capacitance cell, where a standard spectrometer cell (supplied by Starna Ltd.) is placed.

In the first place the cells themselves have to be calibrated, to determine the path length and the thickness of the quartz in the cell. From the expression of the total capacitance of the system (Eq. 4.25) the total thickness of the quartz can be found.

$$\frac{1}{C_t} = \frac{1}{C_a} + \frac{1}{C_q} \qquad (4.25)$$

Using the formula for a parallel plate capacitor [76, 77] the following
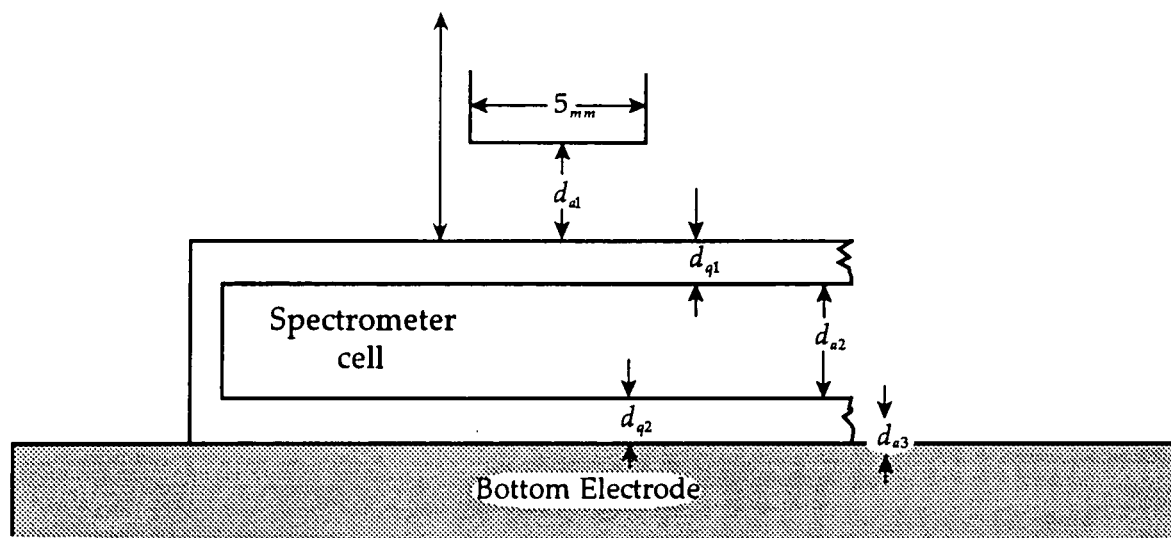
Figure 4.8: Capacitance Cell With Spectrometer Cell in Place.

formulae are obtained

$$\frac{1}{C_t} = \frac{(d_g - d_q)}{\epsilon_0 \epsilon_a' A} + \frac{d_q}{\epsilon_0 \epsilon_a' A}$$

$$\Rightarrow \frac{1}{C_t} = \frac{d_g}{\epsilon_0 A} + \frac{d_q\left(1 - \epsilon_q'\right)}{\epsilon_q' \epsilon_0 A} \qquad (4.26)$$

where the various distances are defined in figure 4.8 and assuming $\epsilon_a' = 1$. A plot of d_g vs. $1/C_t$ yields $1/\epsilon_0 A$ where A is the "effective" area which is substituted into the intercept

$$c = \frac{d_q\left(1 - \epsilon_q'\right)}{\epsilon_q' \epsilon_0 A} \qquad (4.27)$$

Rearranging Eq. 4.27 gives the following expression for the thickness of quartz in the cell:

$$d_q = \frac{c \epsilon_q' \epsilon_0 A}{1 - \epsilon_q'} \qquad (4.28)$$

For the purposes of determining the dielectric constant of the solution the

thickness inside the cell must be determined. This is found by using a travelling microscope to measure the total cell thickness and subtracting the quartz thickness:

$$path\ length = cell\ thickness - d_q \qquad (4.29)$$

Following the same type of analysis as employed to find the quartz thickness the dielectric constant of a particular solution can be found. This time the capacitance of the material is substituted for the air space in the cell. Entering the previously calibrated constants into the expression for intercept and gradient of graph d_g vs. $1/C_t$ yields

$$\epsilon'_m = \frac{path\ length}{path\ length + d_q \left(1 - \frac{1}{\epsilon'_q}\right) + c\epsilon_0 A} \qquad (4.30)$$

A typical run consists of preparing a stock solution in a glove box, under nitrogen, due to the hygroscopic nature of 1,4 dioxane and, using spectrometer cells, make up solutions of varying weight fractions. These are converted to concentrations, where weight fraction and concentration are defined as:

$$weight\ fraction = \frac{mass\ of\ solute}{mass\ of\ solute + mass\ of\ solvent} \qquad (4.31)$$

$$concentration = \frac{moles}{cm^3} \qquad (4.32)$$

The dielectric constant is measured from high to low concentrations and low to high concentrations so that any ageing effects will be noticed. Plotting ϵ'_m versus concentration and weight fraction yields ϵ_0, $\partial\epsilon/\partial w|_0$, and $\partial\epsilon/\partial C|_0$ thus enabling determination of μ, and hence β_ω.

To extrapolate β_ω to β_0 (zero frequency) the two–level model (cf. § 2.6)

is used. Here we divide β_0/β_ω to get

$$\beta_0 = \beta_\omega \left(1 - \frac{\omega^2}{\omega_{eg}^2}\right) \left(1 - 4\frac{\omega^2}{\omega_{eg}^2}\right) \tag{4.33}$$

and use $\omega_{eg} = c/2\pi\lambda_{\max}$ where $\lambda_{\max}$ is obtained from the absorbance spectra of very dilute solutions. The error introduced by using $\lambda_{\max}$ to calculate ω_{eg} can be neglected as it is less than those errors inherent in the two–level model.

Chapter 5

Experimental Methods:

Devices

5.1 Introduction

Up to now the discussion has been limited to specific molecular properties, especially β and attention will now be turned to device considerations. The device configurations considered here are waveguide devices rather than bulk devices. This is because optical confinement, where quadratic effects are important, offers two main advantages over the bulk. (i) It has been reported [26] that up to two orders of magnitude increase for second harmonic generation can be achieved if the device is configured as a waveguide rather than as a bulk configuration. (ii) Optical switching using electric field induced phase shifts benefits due to the ratio of the interaction length versus the electrode spacing [2, 78].

The other point to be noted is that nonlinear molecules that have a centrosymmetric crystal structure can be dispersed in a polymer matrix and ori-

ented with a poling field to achieve noncentrosymmetric configurations[79, 80, 81]. With the use of hydrogen bonding[50] and cross linking [82] the stability problems associated with poled polmers in the past have been surmounted to the point that they can be considered for commercial applications [83].

To combine the work of molecular properties and devices, doped polymers were chosen because, (i) it was not possible to grow thin film crystals in the time provided, (ii) the crystal structures of some of the materials were centrosymmetric, (iii) relevance to processing methods used in industry[83].

Although there are general properties that waveguide devices must fulfil there are many that depend only on the application. For the devices considered here: refractive indices, solvents and nonsolvents of polymers, loss, and poling characteristics are the properties that must be known before the simplest slab waveguide device can be made. The basis of their importance will be discussed when the necessary theory has been shown.

5.2 Theory

It is simplest to start the theory of thin film optical waveguiding with the ray treatment. The coordinate system used in the rest of this section can be seen in figure 5.1. For wavguiding to be achieved the refractive index of the guide, n_1, must be greater than the refractive indices of both the cladding layer, n_2, and the substrate n_0. From Snell's law we have

$$\frac{\sin \theta_2}{\sin \theta_1} = \frac{n_1}{n_2}, \quad and \quad \frac{\sin \theta_0}{\sin \theta_1} = \frac{n_1}{n_0} \tag{5.1}$$

As angle θ_1 increases above the critical angle $\sin^{-1}(n_2/n_1)$ the impossible condition $\sin \theta_2 > 1$ occurs and there is total internal reflection at the air/film
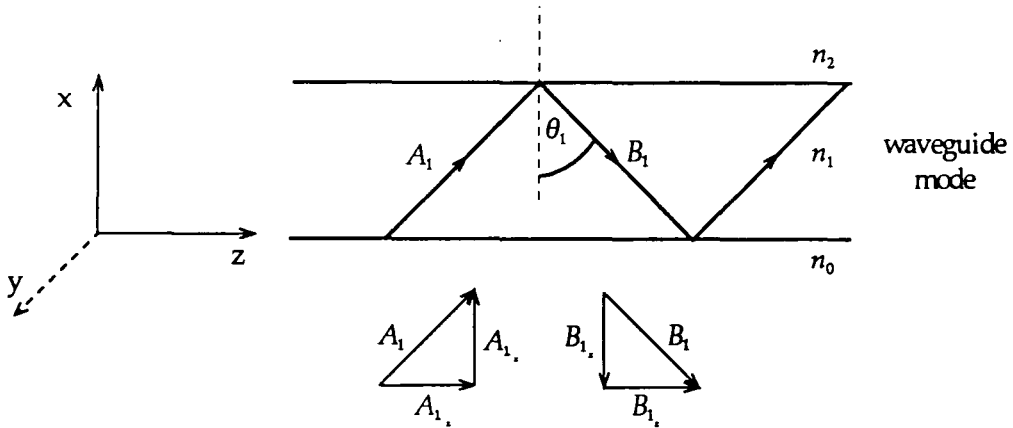
Figure 5.1: Waveguide Coordinate System.

interface and a substrate mode can occur. Similarly as angle θ_1 increases further it is possible to achieve a waveguide mode. This guided wave can be represented by a zigzag made up of two vectors A_1 and B_1 which can in turn be decomposed into vertical and horizontal components. For these waves to add in phase the vertical round trip must be $2m\pi$ where m is an integer [84, 28]. The vertical components of A_1 and B_1 have magnitude $kn_1 \cos \theta_1$ as the vectors have magnitude kn_1, where the wavenumber $k = \omega/c$. There are also phase changes at each reflection, $-2\phi_{12}$ at the top boundary, and $-2\phi_{10}$ at the bottom boundary, which represent the Goos–Haenchen shifts [85]. Taking all the phase conditions into account leads to

$$2f k n_1 \cos \theta_1 - 2\phi_{10} - 2\phi_{12} = 2m\pi \qquad (5.2)$$

where f = film thickness. From a consideration of the evanescent transmitted wave at the boundaries the phase shift can be calculated. For the transverse

electric (TE), and the transverse magnetic (TM) cases this is [86, 87]:

$$TE \begin{cases} \tan\phi_{12} = \left(n_1^2\sin^2\theta_1 - n_2^2\right)^{\frac{1}{2}} / \left(n_1\cos\theta_1\right) \\ \tan\phi_{10} = \left(n_1^2\sin^2\theta_1 - n_0^2\right)^{\frac{1}{2}} / \left(n_1\cos\theta_1\right) \end{cases} \qquad (5.3)$$

$$TM \begin{cases} \tan\phi_{12} = n_1^2\left(n_1^2\sin^2\theta_1 - n_2^2\right)^{\frac{1}{2}} / \left(n_2^2 n_1\cos\theta_1\right) \\ \tan\phi_{10} = n_1^2\left(n_1^2\sin^2\theta_1 - n_0^2\right)^{\frac{1}{2}} / \left(n_0^2 n_1\cos\theta_1\right) \end{cases} \qquad (5.4)$$

5.3 Waveguide Fabrication

Waveguide fabrication is essentially the formation of a guide layer of higher refractive index than its surroundings. Fabrication of polymer waveguides can be achieved by several methods [88]. Two methods, the withdrawal technique [89] and the spinning technique, are chosen for their simplicity.

Withdrawing a substrate at a constant velocity from a solution of polymer can produce high quality films of dimensions suitable for optical waveguides. At a set solution viscosity, differing withdrawal speeds produces differing film thicknesses, with higher speeds producing thicker films than slower speeds.

In the case of spinning, the polymer solution is placed on the substrate and the substrate spun to disperse the solution creating a thin film. The viscosity of the solution and to a lesser extent, the number of revolutions per minute determining the thickness. More viscous solutions and slower spin speeds producing the thickest films.

Typically 2 → 3g of polymer is dissolved in an appropriate solvent to make up a solution of around 10% w/w (weight of polymer per weight of solvent). This solution is then filtered down to 0.5 μm. The fabrication technique used depends on the volatility of the solvent in the polymer solutions. High

volatility solvents are best suited to the withdrawal technique and spinning for the lower volatility solvents. The solvent is removed in the same way for both techniques, where the films are baked in a vacuum oven at slightly less than the glass transition temperature, T_g, until the solvent has fully evaporated.

Fused silica or ordinary glass substrates are used, fused silica being preferred as its refractive index (cf. Table 7.3) is lower than most glasses and consequently a wider range of polymer guides can be made. These simple slab waveguides are the basis for the measurement techniques described in the rest of this chapter.

5.4   Input and Output Coupling

The methods of waveguide fabrication have been discussed but are of little use if waveguide modes cannot be excited. This section will describe the three main methods used to introduce light into optical waveguides.

Coupling efficiency and mode selectivity are the principle characteristics of importance in choosing a coupling method. Coupling efficiency is usually defined as an insertion loss in dB, or alternatively as a fraction of the input beam power. When a mode selective coupler is used, the efficiency can be determined independently for each mode. The coupling loss is defined as:

$$loss = 10\log \frac{\text{Total power in input beam}}{\text{Power coupled into (out of) the } m^{th} \text{ mode}} \qquad (5.5)$$

and the coupling efficiency is defined as:

$$\eta_m = \frac{\text{Power coupled into (out of) the } m^{th} \text{ mode}}{\text{Total power in input beam}} \qquad (5.6)$$
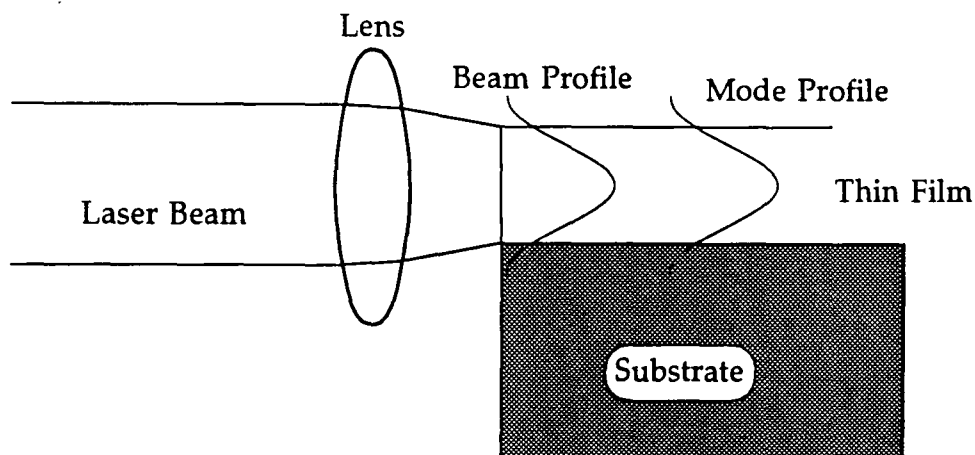
Figure 5.2: End–Fire Coupling

In general the coupling efficiency depends most on the degree of matching between the field profile of the mode and the field profile of the input beam.

5.4.1   End–Fire Coupling

End–fire coupling is a simple method that transfers the beam power to a mode by focusing directly onto the end face of the waveguide (cf. figure 5.2). The beam field profile must be closely matched to the waveguide mode field pattern for efficient coupling [90, 91, 92]. For this reason end–fire coupling is most efficient for monomode guides where the field profile is closest to the Gaussian distribution of the laser beam. Alignment, both in focus point and vertical height is critical, and so micrometer controlled translation stages have to be used.

5.4.2   Prism Coupling

The prism coupling technique [93, 84] employs the process of frustrated total internal reflection to couple an incident laser beam, via an evanescent wave, into a thin film.(cf. figure 5.3).

To couple the laser beam into the thin film the angle that the laser makes with the base of the prism must be large enough to produce total internal reflection. At this point a standing wave is set up with an evanescent tail beneath the prism extending into the air gap. If the gap is of the order $\frac{1}{8}$ of the wavelength [28] this tail will extend into the film. At the point the horizontal component of one of the waveguide modes equals that of the light wave in the prism, energy can be coupled between the prism and the film. As energy can transfer in either direction, the laser beam has to be positioned as close to the corner of a right angled prism as possible. In this configuration the light is trapped in a waveguide mode. Another prism can be clamped in the opposite sense, to couple light out, which can then be viewed on a screen.

From the screen the particular mode of excitation can be seen, so the angle the incident laser beam makes with the prism can be associated with a mode number. By definition, mode zero has the smallest angle, θ_2 then mode 1, mode 2, etc until the substrate modes are encountered. It is a simple matter to calculate the mode index from the laser angle normal to the prism face. (cf. figure 5.3). Taking clockwise from the normal as positive angles, Snell's law can be used to determine the angle in the prism, giving

$$\frac{\sin \theta_1}{\sin \theta_0} = \frac{n_0}{n_1} \Rightarrow \theta_1 = \sin^{-1}\left(\frac{n_0 \sin \theta_0}{n_1}\right) \tag{5.7}$$

this leads by elementary geometry to the angle relative to the base of the prism:

$$\theta_2 = \frac{\pi}{2} - \phi + \theta_1 \tag{5.8}$$

From the condition that the horizontal components of the waveguide mode

FILM
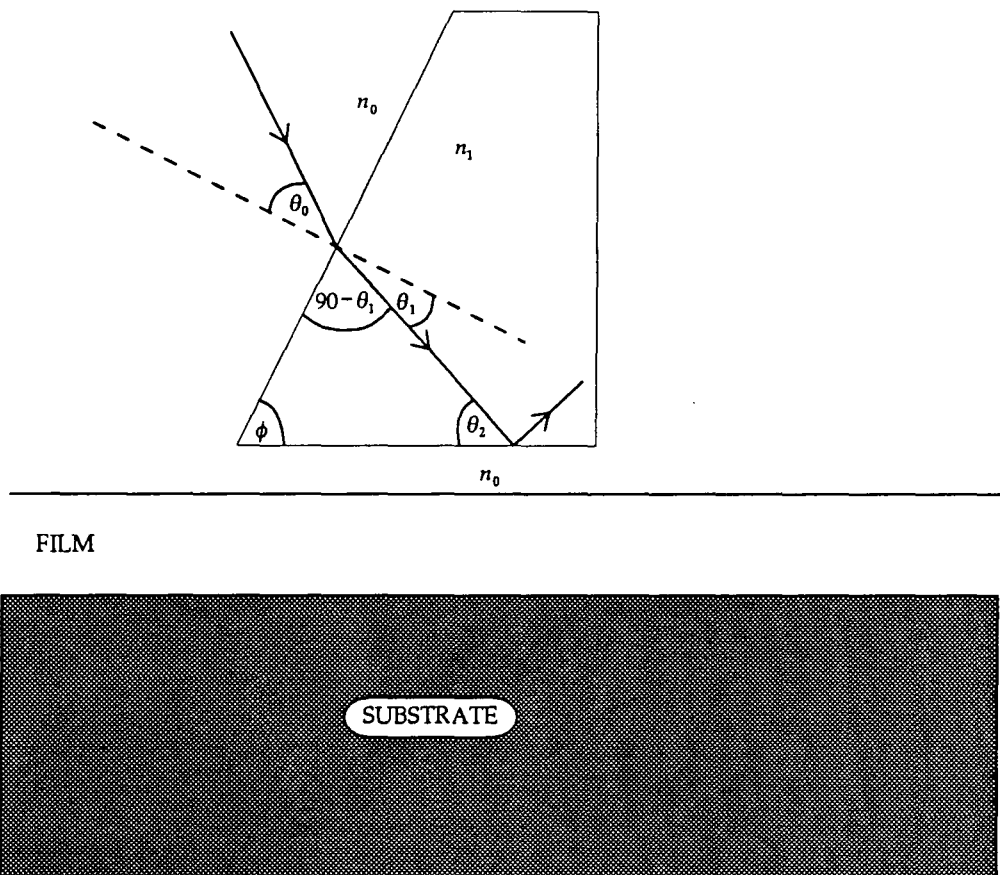
Figure 5.3: Prism Coupling: ϕ=prism angle, n_0=cladding index, n_1=prism index, θ_0 = incident beam angle to normal, θ_1 = refracted beam angle to normal, θ_2 = refracted beam angle to prism base
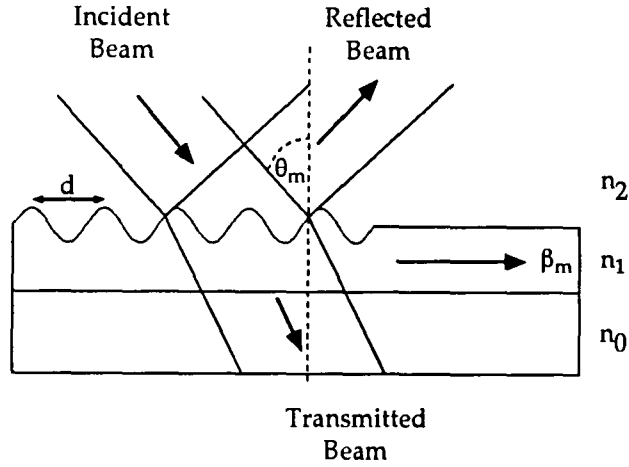
Figure 5.4: Grating Coupler: ϕ = prism angle, n_0= substrate, n_1 = guide index, n_2 = cladding index d = periodicity, θ_m = incident beam angle to normal, β_m = mode propagation constant

and the laser in the prism must be equal for coupling:

$$n_m = n_1 \cos \theta_2 \text{ or } n_m = n_1 \cos \left(\frac{\pi}{2} - \phi + \sin^{-1} \left(\frac{n_0 \sin \theta_1}{n_1} \right) \right) \qquad (5.9)$$

where n_m is the mode index.

By rotating the laser relative to the prism, angles for all the modes can be determined and hence the refractive index for each mode. Using this information the film index and thickness can be determined (cf. § 5.6).

5.4.3 Grating Coupler

The grating coupler is similar to the prism coupler [28, 94] in that it enables phase matching between a waveguide mode and the incident optical beam (cf. figure 5.4). Due to the periodic nature of the grating the wave supported by the film acquires harmonics over the length of the grating. The

propagation constants of these harmonics is given by [94]:

$$\beta_\nu = \beta_0 + (2\nu\pi/d), \quad \nu = 0, \pm 1, \pm 2, \cdots, \tag{5.10}$$

where β_0 is approximately equal to the mode propagation factor under the assumption that the perturbation from the grating is small. As ν can take on negative values it is possible to couple light into the film at certain θ_m values.

The main advantage of the grating coupler is that it is an integral part of the structure and so does not suffer from the mechanical displacements that are possible with end–fire and prism coupling.

5.5   Loss Measurements

In commercially viable devices only a certain amount of loss can be tolerated, because in general low power pump lasers are used. This loss is a combination of input coupling, output coupling, and guiding loss, for each component. Input and output coupling losses are well characterised and have set values for each coupling method. Depending on the guide structure and materials used the guide losses can vary over orders of magnitude.

To determine guide losses several methods can be used [95], with the best method being a measurement of transmitted power as a function of guide length. The can be done with two prisms, an input coupler and a sliding ouput prism. The input prism is coupling into mode zero and the output prism being moved closer and closer towards the input prism. If a graph of $10 \log(V)$ versus distance is plotted the gradient gives the loss in dB cm^{-1} which is in the most convenient units for a comparison to the literature.

5.6 Refractive Index Calculation

The calculation of the refractive index of step index thin films can be derived in a number of ways [96, 97] with the method presented here based on the normalised frequency [87, 98],V (cf. Eq. 5.11).

$$V = kf \left(n_1^2 - n_0^2\right)^{\frac{1}{2}} \tag{5.11}$$

where $k = 2\pi/\lambda$, f is the film thickness, n_1 is the film refractive index, and n_0 is the substrate refractive index. In the literature it is common practice to use normalised variables. This is to express the main equations in a general form which is independent of the refractive index, and guide width.

From the discussion in § 5.4 it should be obvious that for films with a large number of modes, differentiating between modes will be subject to more uncertainty than for films with less modes. Fabricating films that support three to four modes returns the best results as modes are easily separated but there are still enough modes to be able to determine an average value of refractive index. Using cut-off values for Eq. 5.2 and the normalised frequency it is possible to determine the number of modes a guide can support given refractive index and thickness [87]:

$$TE: \quad M = \left\{\frac{1}{\pi} \left(V - \tan^{-1}\left[\left(\frac{n_0^2 - n_2^2}{n_1^2 - n_0^2}\right)^{\frac{1}{2}}\right]\right)\right\}_{int} \tag{5.12}$$

$$TM: \quad M = \left\{\frac{1}{\pi} \left(V - \tan^{-1}\left[\left(\frac{n_1}{n_2}\right)^2 \left(\frac{n_0^2 - n_2^2}{n_1^2 - n_0^2}\right)^{\frac{1}{2}}\right]\right)\right\}_{int} \tag{5.13}$$

where M is the number of modes, expected at the wavelength being used, n_2 is the cladding index, and int indicates the next largest integer. Using

a guess for the refractive index and choosing a thickness of around 3 μm, substitution into Eq. 5.12 or Eq. 5.13 gives the number of modes expected. The thickness is changed until there are a reasonable number of modes. The films are fabricated to the thickness wanted, then the refractive index can be determined from the method of Kogelnik [98].

5.6.1 For TE Modes

To calculate V, the asymmetry measure a, of the waveguide has to be calculated

$$a = \frac{n_0^2 - n_2^2}{n_1^2 - n_0^2} \tag{5.14}$$

where n_2 is the cladding refractive index. The normalised guide index b has to be calculated

$$b = \frac{n_m^2 - n_0^2}{n_1^2 - n_0^2} \tag{5.15}$$

where n_m is the refractive index of a particular mode. Using a and b, a value of V can be calculated from:

$$V(1 - b)^{\frac{1}{2}} = m\pi + \tan^{-1}\left[\left(\frac{b}{1 - b}\right)^{\frac{1}{2}}\right] + \tan^{-1}\left[\left(\frac{b + a}{1 - b}\right)^{\frac{1}{2}}\right] \tag{5.16}$$

where m is the mode number.

5.6.2 For TM Modes

In the case of TM modes two asymmetry measures, a and d are needed. Also a reduction factor q_0 is required. These are defined as:

$$q_0 = \frac{n_m^2}{n_1^2} + \frac{n_m^2}{n_0^2} - 1 \tag{5.17}$$

$$a = \frac{n_1^4}{n_2^4} \cdot \frac{n_0^2 - n_2^2}{n_1^2 - n_0^2} \tag{5.18}$$

$$b = \frac{n_1^2}{n_0^2 q_0} \cdot \frac{n_m^2 - n_0^2}{n_1^2 - n_0^2} \tag{5.19}$$

$$d = \frac{1 - n_0^2}{n_1^2} \cdot \frac{1 - n_2^2}{n_1^2} \tag{5.20}$$

leading to the following expression:

$$\frac{V q_0^{\frac{1}{2}} n_1 (1 - b)^{\frac{1}{2}}}{n_0} = m\pi + \tan^{-1}\left[\left(\frac{b}{1 - b}\right)^{\frac{1}{2}}\right] + \tan^{-1}\left[\left(\frac{b + a(1 - bd)}{1 - b}\right)^{\frac{1}{2}}\right] \tag{5.21}$$

A computer program was written (and listed in Appendix A) to calculate the film thickness and refractive index for a measured set of mode indices, usually from prism coupling. From Eqs. 5.16 and 5.21 the film thickness at a particular film index can be calculated for each mode. The variance between the film indices is calculated. Starting from mode zero the film index is chosen as the point that minimises the variance between the film thicknesses. This automatically weights the modes correctly as mode zero has the highest dispersion, and consequently has the most accurate mode angle. If only a monomode film can be made it is still possible to measure the film index provided the thickness is accurately known eg. by measuring with a surface profiler. A plot of the mode dispersion gives the refractive index at the measured thickness. However this method is less accurate as no independent measure of the mode angle accuracy is available.

When the refractive index of highly absorbing or scattering films is required the double prism method cannot be used as any signal will be too

small. In this case an isosceles shaped prism is used where guiding is only of

the order of the beam width. The modes are found when there is a drop in

the reflected wave intensity from the film where each mode is excited. The

film thickness and refractive index are found in the same way as for prism

coupling.

Another method of measuring the refractive index is from the analysis

of interference fringes produced when a thin film is placed in a spectropho-

tometer. The film refractive index can be shown to be [99]:

$$n_1 \approx \frac{1}{2fs} \tag{5.22}$$

where s is the separation of the interference maxima measured in wavenum-

bers. This method though less accurate is useful for determination of the

index over a range of wavelengths.

5.7   Linear Electro–Optic Effect

Electro–optic effects can be broadly defined as changes in the optical proper-

ties of a material by the application of an electric field. When the refractive

index changes linearly with the field amplitude, the effect is known as the

linear electro–optic, or Pockels effect.

A beam propagating through an anisotropic material can be thought of

as having two orthogonal linearly polarised electric field components. These

two fields will in general propagate with different velocities leading to bire-

fringence. The birefringence can be represented by an index ellipsoid [39]:

$$\frac{x^2}{n_1^2} + \frac{y^2}{n_2^2} + \frac{z^2}{n_3^2} = 1 \tag{5.23}$$
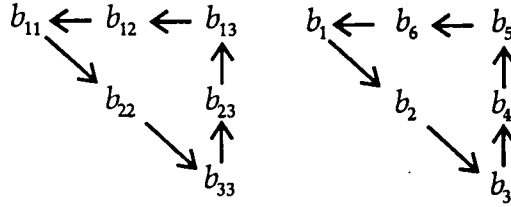
Figure 5.5: Tensor Contraction

On applying a field the linear electro–optic effect produces a change in the

index ellipsoid represented by new off–axis components:

$$b_{11}x^2 + b_{22}y^2 + b_{33}z^2 + 2b_{23}yz + 2b_{13}xz + 2b_{12}xy = 1 \qquad (5.24)$$

where $b_{11} = 1/n_{11}^2$. Using symmetry conditions this notation can be con-

tracted to

$$b_1x^2 + b_2y^2 + b_3z^2 + 2b_4yz + 2b_5xz + 2b_6xy = 1 \qquad (5.25)$$

which can be visualised more easily by reference to figure 5.5. The elec-

trooptic tensor gives the change of b_i as the result of an applied field E_j

giving

$$\Delta b_i = r_{ij}E_j \ (i \rightarrow 1 \ldots 6) \ (j \rightarrow 1 \ldots 3) \qquad (5.26)$$

remembering that r_{ij} is really a third rank tensor [2]

$$\Delta \left(\frac{1}{n^2} \right)_i = r_{ij}E_j \ (i \rightarrow 1 \ldots 6) \qquad (5.27)$$

The electro–optic coefficients r_{ijk} can be measured by the linear electro-

optic effect. If a linearly polarised laser beam is incident on such a material,

on emerging from the material there will be an induced phase difference in
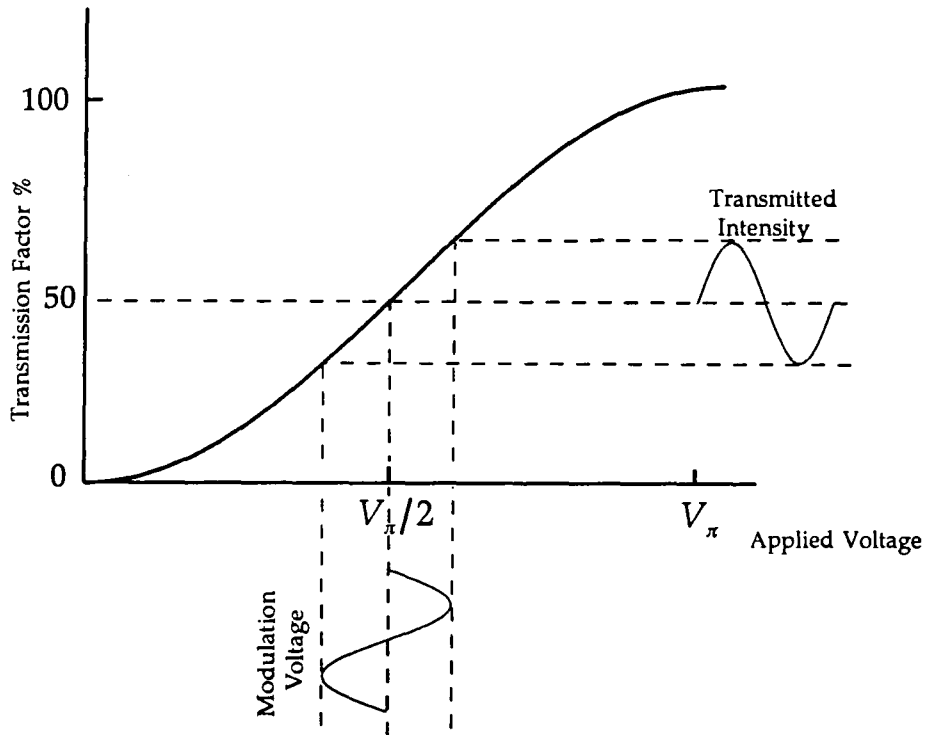
Figure 5.6: Modulation Voltage versus Transmission Factor %

addition to the static phase difference between the ordinary and the extraordinary components. Several methods have been developed to determine r_{33} in poled polymers and molecular crystals by measuring this phase difference [100, 79, 101, 78]. The basis of the measurement technique employed is electro–optic amplitude modulation [2], (cf. figure 5.6) where V_π is the bias required to change the phase difference by π. The set–up is a modified version of that described in reference [100] and is a reflection technique, useful for materials too absorptive and/or too lossy for waveguiding. This method simplifies the usual $\sin^2$ response by biasing the intensity at the $V_\pi/2$ point. The object of this is to centre the output on a quasi–linear region of the transmission curve, enabling the intensity ratio to be linear with phase shift, providing the modulation voltage is small. In practice the phase bias is achieved with a Soleil–Babinet compensator so that any intrinsic birefringence is removed,
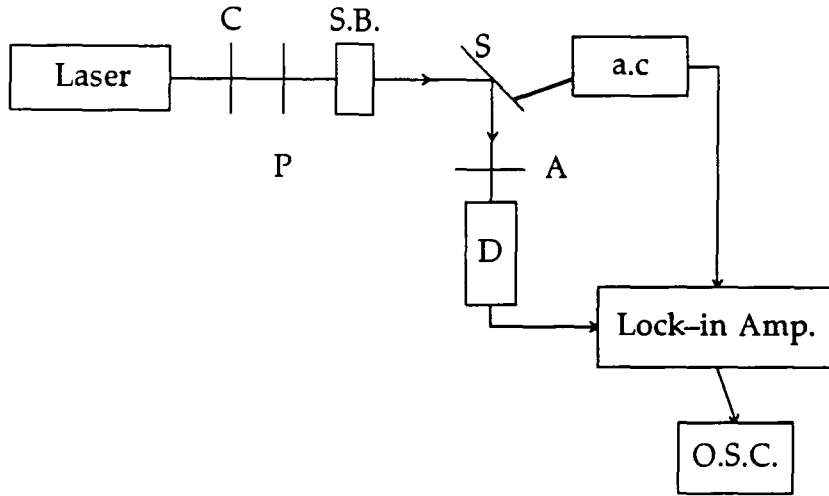
Figure 5.7: Electro–Optic Experimental Setup; C = Chopper, P = Polariser, S.B. = Soleil–Babinet, S = Sample, A = Analyser, D = Detector, a.c. = Modulation voltage, O.S.C. = Oscilloscope

and only the field induced response measured. The experimental set–up is shown schematically in figure 5.7. From this setup the linear electrooptic coefficient can be calculated from experimentally measured values using

$$r_{33} = \frac{3\lambda I_m \left(n^2 - \sin^2\theta\right)^{\frac{3}{2}}}{4\pi V_m n^2 I_0 \left(n^2 - \sin^2\theta\right)\sin^2\theta} \tag{5.28}$$

where V_m is the modulation voltage, λ the wavelength, and I_m and I_0 are the modulation intensity and incident intensity respectively. This assumes that the ratio $r_{33}{:}r_{13}$ is constant at 3:1. By setting the film at 45° the sine terms are set at $1/\sqrt{2}$

5.8 Poled Polymers

In general $\chi^{(2)} = 0$ for centrosymmetric systems such as polymers. This is also the case when nonlinearly optically active chromophores are dispersed into the polymer matrix. If the chromophores are dipolar it is possible to
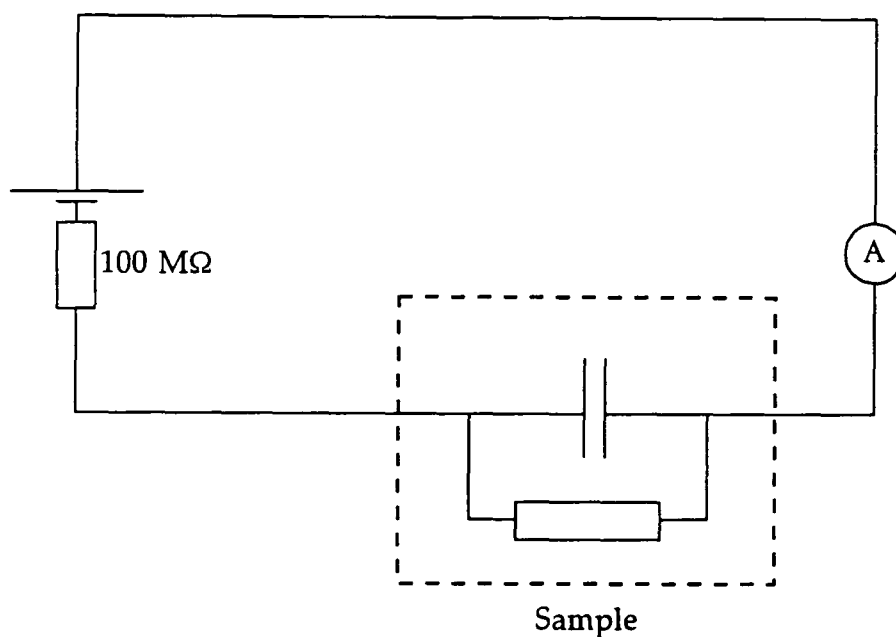
Figure 5.8: Poling Circuit

align them under the action of an electric field. These permanent dipoles experience a force which tends to align them with the applied field (cf. § 4.2.2). An equilibrium is reached with this alignment and the kinetic energy associated with thermal equilibrium in the system. To align the chromophores they must be free to rotate, which involves heating the polymer to near its glass transition temperature, T_g while a field is applied. After allowing time for alignment the polymer is cooled down with the field still applied. When the field is switched off the chromophores are held in place by the now rigid polymer matrix. Figure 5.8 shows the equivalent circuit when poling polymers using fixed electrodes. Another method, known as corona poling, where the field is generated by injecting electrons from a corona discharge from a needle point, can be used to pole thin films [102]. Fixed electrode poling was used, as the same electrodes could be used for the modulating fields that would drive the electro–optic experiments.

When a sample is poled it is useful to monitor the current versus heating

and cooling to see how the material responds as T_g is approached. This is because when a nonlinear optical material is added to the polymer the T_g of the mixture is not precisely known. As the polymer matrix is heated up a current is passed, up to the point of catastrophic breakdown. To align the molecules a high field has to be maintained across the sample, but at the same time the molecules must be free to rotate. These two necessities are mutually exclusive so a compromise has to be reached. This is usually just below T_g.

5.9 Amplitude Modulation

The discussion previously has concentrated on techniques to measure the properties related to device fabrication. However to determine if this is correct a working device applying these methods should be made. The choice was that of an amplitude modulator, not only because this ties together all the previous work but also it has the added merit of giving an independent determination of r_{33} over the reflection technique (cf. § 5.7).

The method relies on the same background theory as § 5.7 but the light is guided in this configuration instead of transmitted. This means that there is enough interaction with the sample to change the phase of one orthogonal component with respect to the other by π. To take the measurement a transverse electrode waveguide structure has to be made (cf. figure 7.10) and the output of the waveguide measured. The voltage required for complete extinction of the output is termed V_π [2] and

$$V_\pi = \frac{\lambda d}{r_{33} n_{eff}^2 LG} \tag{5.29}$$

where V_π is the switching voltage, λ is the laser wavelength, d is the electrode gap, G is the fraction of energy guided in the active layer, r_{33} is the electro-optic coefficient, L is the waveguide length, and n_{eff} the mode index. In general the guide is mono-mode so that there is no possibility of cross modal coupling to reduce the efficiency.

Chapter 6

Results: Molecules

6.1 Introduction

The method of determining the first hyperpolarisability has been described. Here the results for four chromophores are presented, which gives a static value of β for each. This determination necessarily includes the calibration steps and a description of the linear optical properties of the chromophores.

For all the molecules studied, the optical absorption spectra in either 1,4 dioxane or DMF (N N dimethylformamide), is taken. The dipole moment is determined at 1MHz. Γ is measured at several concentrations, and from this information β_0 is calculated.

6.2 Dipole Moments

To measure the dipole moment the relative permittivity at various concentrations has to be determined. The cell dimensions are not known precisely enough for the relative permittivity to be determined satisfactorily. In figure 6.1 a graph of reciprocal capacitance of the empty cell versus air gap is
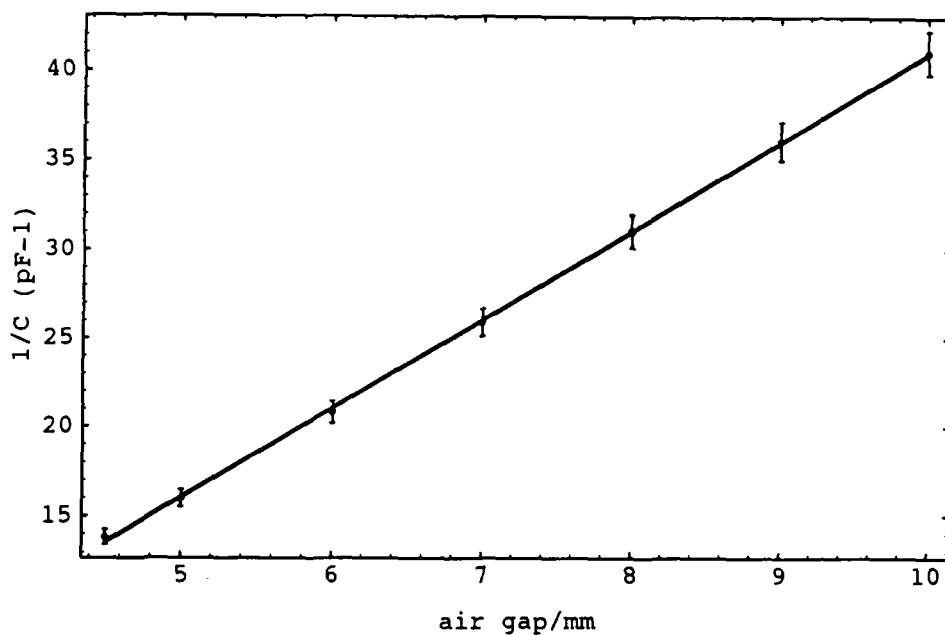
Figure 6.1: Cell Calibration Data

cell number	$d_q/mm \pm \sigma$	$d_m/mm \pm \sigma$
1	2.44±0.03	2.02±0.03
2	2.45±0.03	2.02±0.03
3	2.43±0.03	1.98±0.03
4	2.44±0.03	1.98±0.03

Table 6.1: Cell Calibration Results

shown. The cell thickness, $d_{q_1} + d_{q_2} + d_{a_2}$ (cf. figure 4.8), was measured with a micrometer accurate to 0.01 mm. Using this and Eqs. 4.26 and 4.28 we get d_q and the path length, d_m.

Remembering Eq. 4.30, ϵ'_m can be calculated. As a further calibration the relative permittivity of the the pure solvent, in this case 1,4 dioxane, was measured. This was found to be 2.2 ± 0.1 which is, within error limits the same as the literature value of 2.29 [103].

The same procedure was repeated for different concentrations of the chromophores. As there is the possibility of degradation, from water absorption,
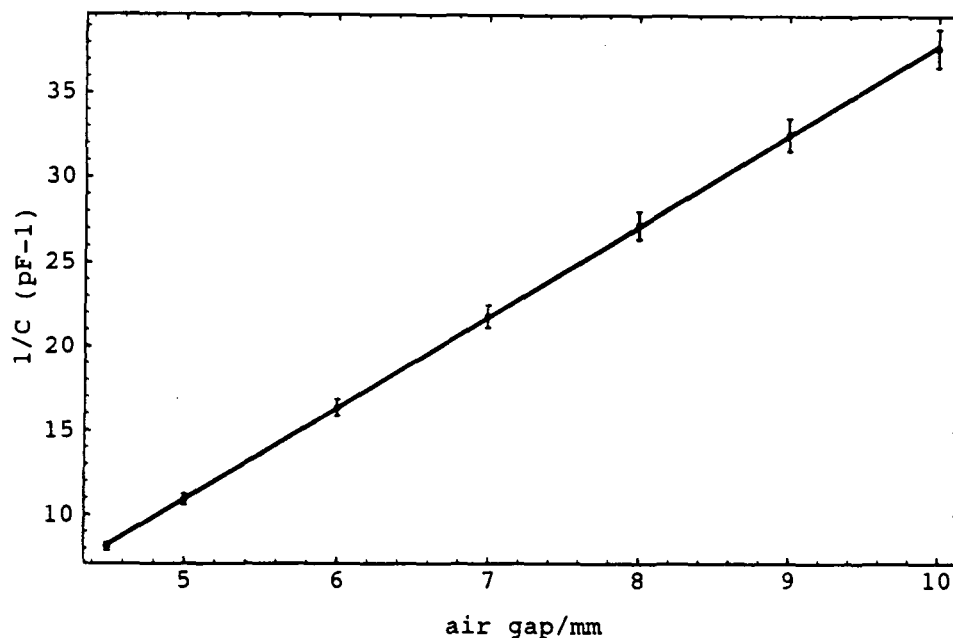
Figure 6.2: DAN 0.25×10^{-2} Weight Fraction

all solution preparations were performed under nitrogen. As a further precaution the solutions were measured alternately from increasing concentration and from decreasing concentration. This method shows any results of degradation, as a departure from a linear dependence, and has the added advantage that only one set of measurements has to be taken. As before (cf. figure 6.2 through to figure 6.5) plots of reciprocal capacitance versus air gap enables the relative permittivity of the material, illustrated in the case of DAN, to be determined.

Plotting the relative permittivity of each solution versus the concentration of the solution (cf. figure 6.6) gives $\partial \epsilon / \partial C|_0$.

Knowing the solvent ϵ' and n and using expression 4.24 the dipole moment of the molecule can be calculated. Substituting the errors from the previous calibrations, and the errors of the constants, the standard deviation of the dipole moment was calculated to be 6%. Table 6.2 shows the dipole moments of the molecules studied.
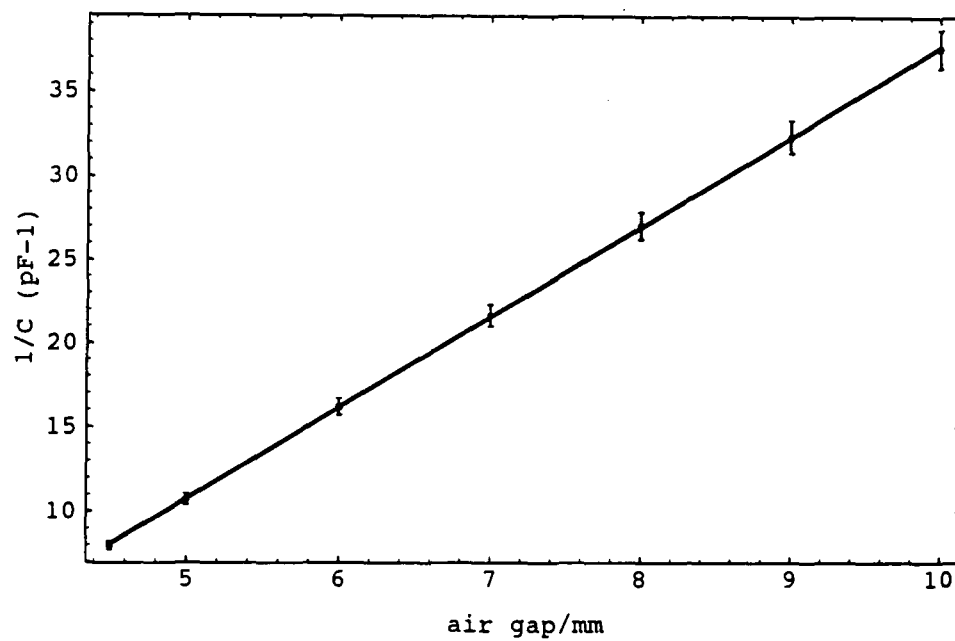
Figure 6.3: DAN 0.50×10^{-2} Weight Fraction
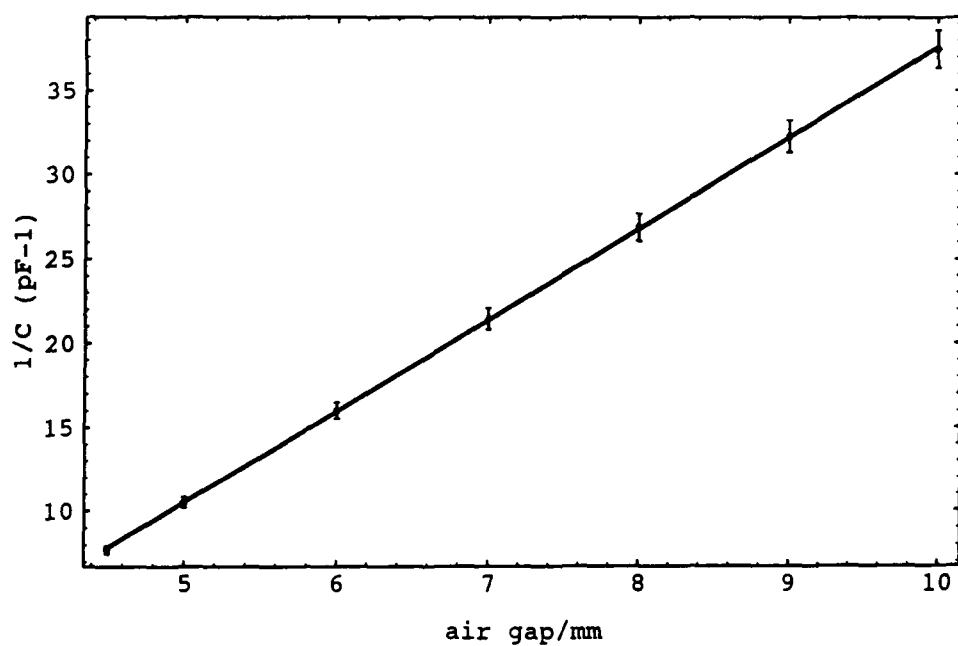
Figure 6.4: DAN 0.75×10^{-2} Weight Fraction
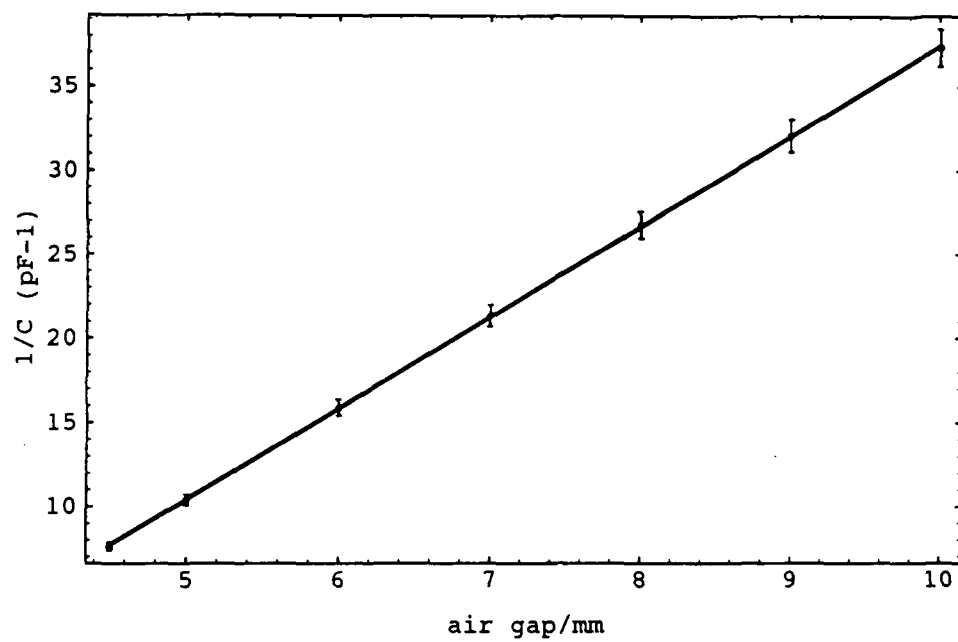
Figure 6.5: DAN 1.00×10^{-2} Weight Fraction
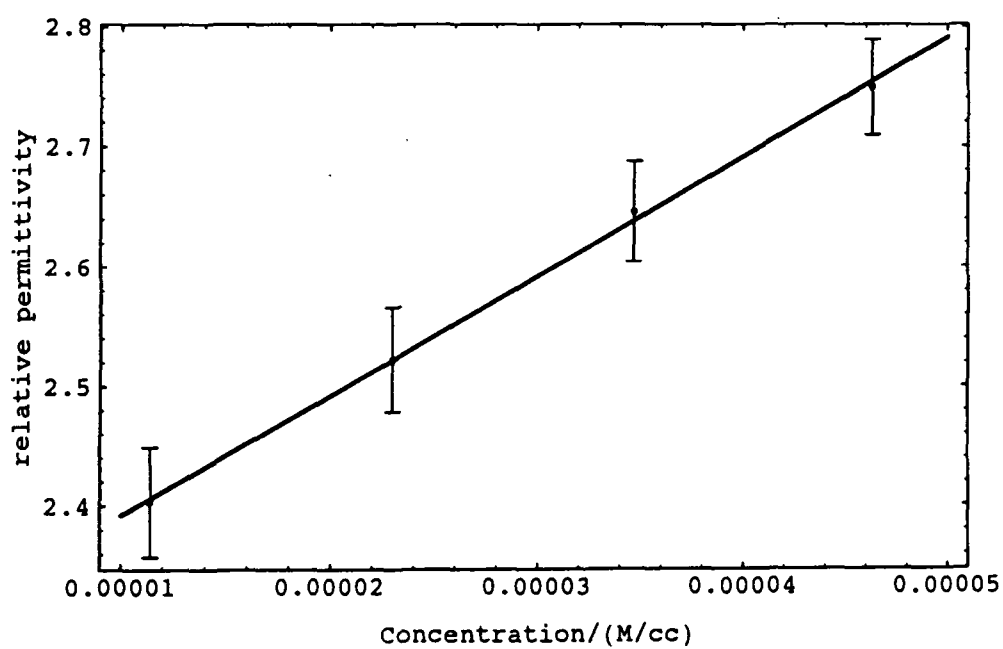
Figure 6.6: DAN Dielectric Constant versus Concentration

Material	Solvent	μ/ (D) (Experimental)	μ / (D) (Theoretical Gas Phase)
MNA.	1,4 dioxane	6.0 ± 0.4	7.39
DAN	1,4 dioxane	9.2 ± 0.6	9.4
NPP	1,4 dioxane	6.7 ± 0.4	9.02
DEMI	DMF	45 ± 10	14 [104]
II	DMF	56 ± 10	21[104]

Table 6.2: Dipole Moments

Also in this table are the dipole moments from AM1 SCF calculations us-
ing MOPAC. The calculations were performed by initially entering the bond
length parameters from the NEMESIS package and converting to MOPAC in-
put with a pattern matching program called awk. DEMI was calculated with
INDO-SCI, SOS (40 states), by Brédas [104]. The table shows that there is
a consistent over estimation of theory compared to experimental value. This
is most likely due to the gas phase nature of the calculation and the equation
(Eq. 4.24) used to calculate the dipole moment not able to account for all
interactions between solvent and solute. Calculations were also carried out
using the crystal structure [57] configuration of DEMI to decide the level of
applied theoretical field. This value was determined to be 35D thus showing
the sensitivity of DEMI to its environment.

6.3 β–Measurements

6.3.1 Calibrations

Using a high voltage probe the actual voltage produced by the pulsed supply
was measured. A graph of this voltage versus monitor voltage measured
using an oscilloscope shows a linear relationship (cf. figure 6.7). Using this
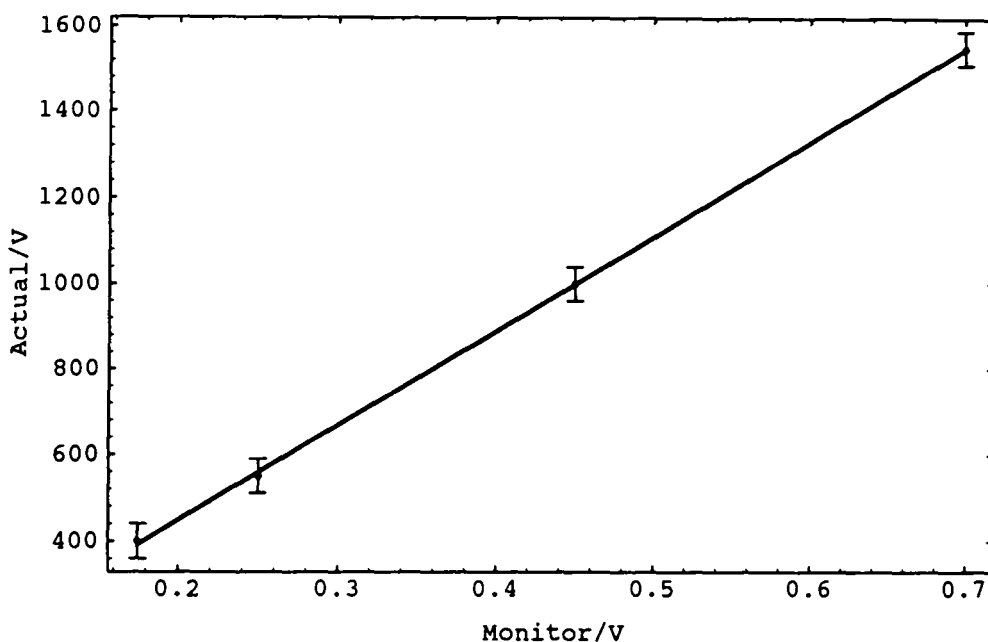
Figure 6.7: High Voltage Supply Calibration

calibration graph the oscilloscope can be used to measure the high voltage

output to a standard error, σ, of 5%.

The next step in determining β_0 is to determine Γ_m for a solution. Before

this can be attempted, Γ for the Schott BK7 glass windows and the solvent,

1,4 dioxane must be determined. Γ_G was determined by placing a piece of

BK7 glass cut to the same dimensions as the solution cavity between the

electrodes and using a relatively low field (15 statvolts per cm) to prevent

air breakdown. This was scanned across the laser beam and referenced with

a quartz wedge. Modifying Eq. 4.16 to exclude the solution term gives

$$\frac{A_m^L}{A_m^Q} = \frac{E_0^2 \left(T_1 \Gamma_G l_c^G\right)^2}{\left(Q_1^2 + Q_2^2\right)^2 d_{11}^2 \left(l_c^Q\right)^2} \tag{6.1}$$

Since the angle of the glass wedge is known, ($2°$), the coherence length and

Γ_G can be determined from the fit to the fringes. This gives a value of

$\Gamma_G = (6.5 \pm 0.5) \times 10^{-14} esu$ which is within the error from the literature
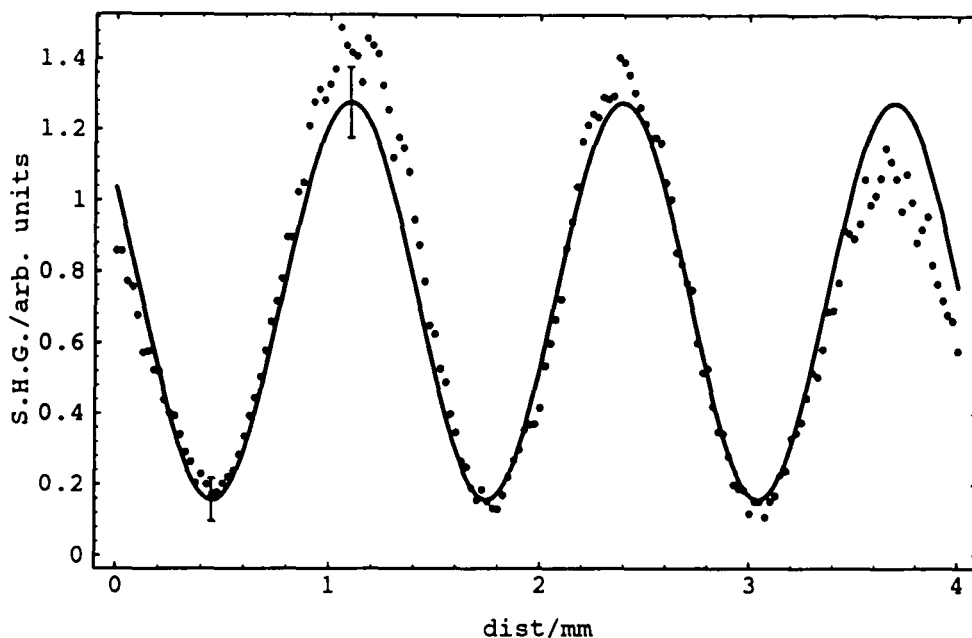
Figure 6.8: NPP: 1.00×10^{-2} Weight Fraction

[68, 72]. A first EFISH scan was performed with pure 1,4 dioxane. The cell was filled under nitrogen using anhydrous 1,4 dioxane (0.0005% water). The cell was sealed with 'Parafilm' and the experiment performed immediately. Using Eqn 4.16 and the value for Γ_G and l_c^G, Γ_m can be extracted giving $\Gamma_L = (3.5 \pm 0.5) \times 10^{-14} esu$. This value gives confidence in the experimental procedure as it is within the error of the accepted value of the solvent [51]. This value can also be used as a check for Γ_0 found using the weight fraction dependence of Γ_m graphs.

6.3.2 $1.064 \mu m$ Experimental Values

An EFISH scan was performed at several concentrations giving the set of graphs seen in figures 6.8 to 6.11. This particular set of data is of NPP at four different concentrations.

Of note is the fact that the coherence length does not change significantly
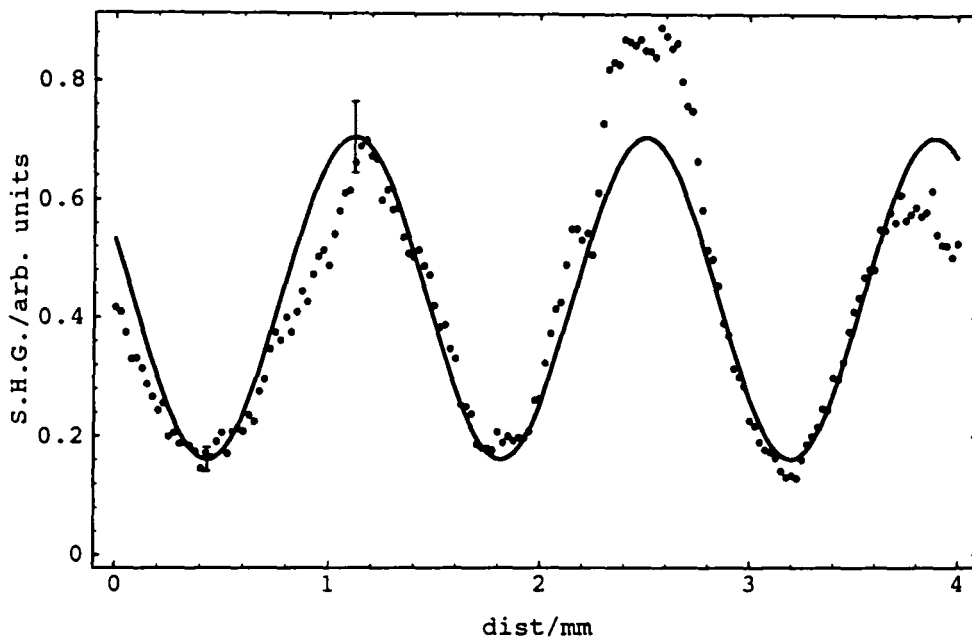
Figure 6.9: NPP: 0.75×10^{-2} Weight Fraction
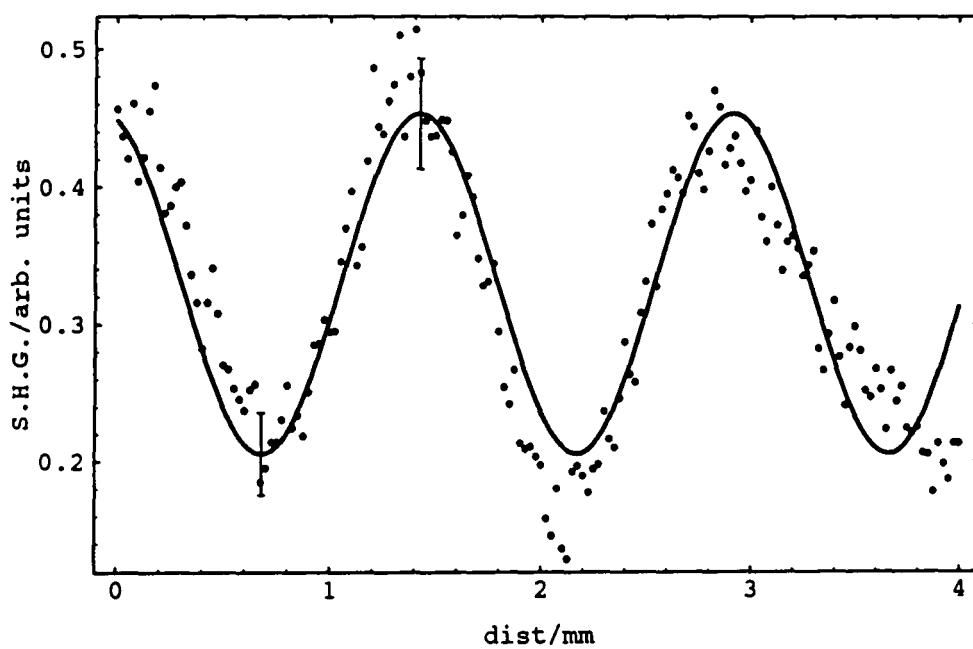
Figure 6.10: NPP: 0.50×10^{-2} Weight Fraction
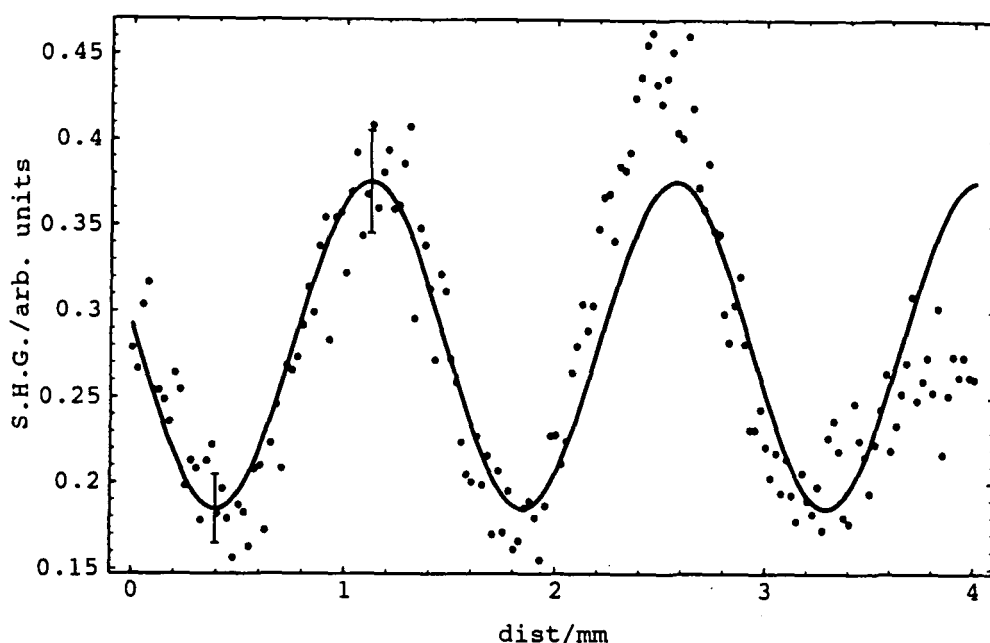
Figure 6.11: NPP: 0.25×10^{-2} Weight Fraction

between concentrations. This is represented by half the period in the fringes. That means that the coherence length of 1,4 dioxane can be used instead. This also gives n_ω since $n_{2\omega}$ is known [75]. The raised baseline shows a small amount of absorption which from the factor $\left(e^{-\alpha_\omega l} + e^{-\alpha_{2\omega} l}\right)$ changes the result by much less than the error.

A quartz scan was taken first (figure 6.12) then successive scans of increasing concentration taken. The quartz coherence length can be calculated for any quartz set of fringes as the wedge angle is known to be $1°$.

A stock solution was made, under nitrogen, and added to $10ml$ of 1,4 dioxane, also under nitrogen. A graduated $10ml$ syringe was filled with the stock solution, and injected into the cell. This whole assembly was then sealed with parafilm and transferred to the EFISH setup. The first scan was taken, then 5, 2.5, and 2.5 ml added respectivly, with enough time left between scans for the solution to mix properly. A quick quartz scan was then taken as a check that there has been no signal drift since the first quartz scan.
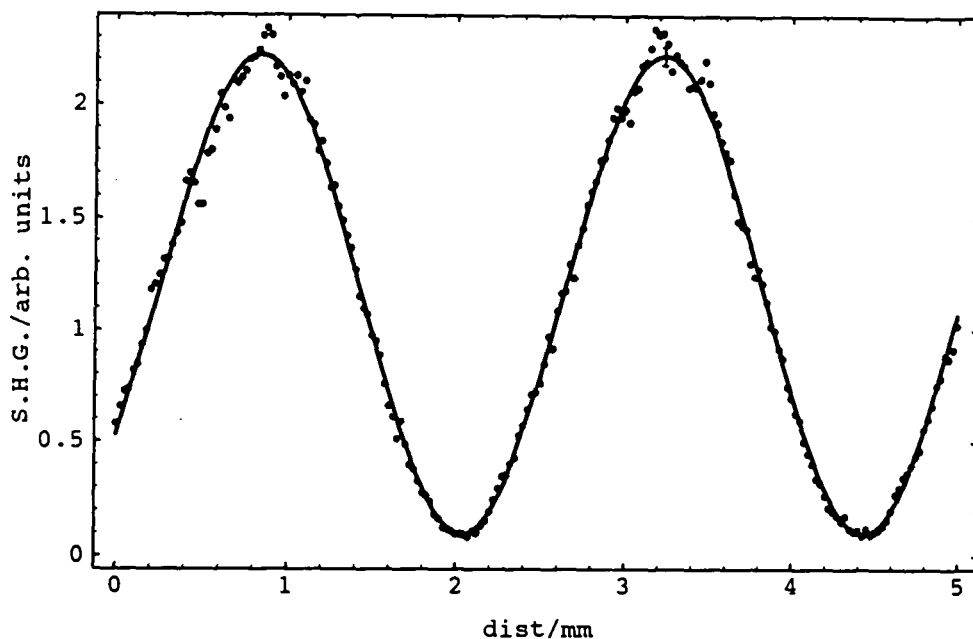
Figure 6.12: NPP Quartz Fringes

From the evidence of the concentration versus ϵ'_m dependence measurements not being affected by aging it was thought that doing the scans in reverse concentration was not required.

Each of the scans gives an effective Γ_m associated with a particular weight fraction. When a graph of Γ_m versus weight fraction is plotted (cf. figure 6.13) , $\partial\Gamma_m/\partial(wf)|_0$ and Γ_0 can be determined. This Γ_0 should be close to that found from the pure solvent.

The literature gives Γ_0=5.1 $\times 10^{-14} esu$ [51] which is of the correct order compared to Γ_0 from this experiment (cf. Table 6.3). The factors due to n^2 and specific volume are omitted from Eq. 4.23 as they are assumed to be negligible. They only contribute a few percent and because of the large uncertainty in the d_{11} value for quartz are omitted.

$\lambda_{\mathbf{max}}$ was determined from the optical absorption spectrum and is given in table 6.3. β_ω is the value of the first hyperpolarisability determined under resonance enhanced conditions. That is, the pump frequency is not infinitely
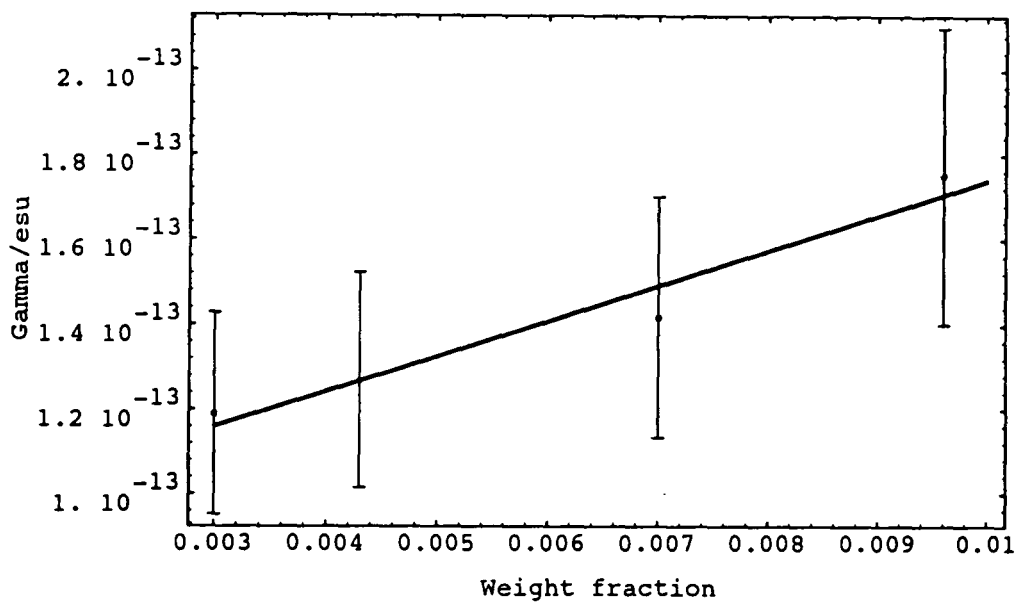
Figure 6.13: NPP Γ Versus Weight Fraction

Material	DAN	MNA.	NPP
Solvent	1,4 dioxane	1,4 dioxane	1,4 dioxane
$\Gamma_0/10^{-14}esu$	4.0 ± 0.4	3.0 ± 0.3	9.1 ± 0.8
$\partial\Gamma_m/\partial(wf)\vert_0/10^{-12}esu$	18 ± 3	9 ± 1	8 ± 1
$\partial\epsilon'_m/\partial(wf)\vert_0$	47 ± 3	29 ± 2	24 ± 2
$\mu/Debye$	9.2 ± 0.6	6.0 ± 0.4	6.7 ± 0.4
$\mu\beta_\omega 10^{-48}esu$	313	121	190
$\beta_\omega/10^{-30}esu$	34 ± 5	20 ± 3	28 ± 5
$\lambda_{max}/10^{-9}m$	355	370	386
$\beta_0/10^{-30}esu$	17 ± 3	9 ± 1	12 ± 2
$\mu\beta_0 10^{-48}esu$	156	54	80

Table 6.3: Summary of 1.064 μm EFISH Experiment

far from the absorption band. Using the two level model [33] (cf. Eq. 4.33) it is possible to scale this value to one where there is no enhancement. This enables a more objective comparison to be made between β values for different molecules. $\mu\beta_0$ is included as a figure of merit, as ease of alignment coupled with high β is important in electrooptic devices. From table 6.3 it can be seen that although DAN and NPP have a similar β the $\mu\beta$ factor for DAN is almost twice that of NPP. This makes DAN a more logical choice for any device related work, especially as it is more transparent, making any device less lossy. $\beta_\omega = (16.7 \pm 0.5) \times 10^{-30} esu$ and $\beta_\omega = 15.3 \times 10^{-30} esu$ [51] values from the literature for MNA compares with $\beta_\omega = (20.7 \pm 3) \times 10^{-30} esu$ from this study. This value suggests that the values obtained are a slight over estimate. This is consistent with the fact that the γ contribution to Eq. 4.2 has been neglected. For a comparative study this over estimate is not significant although it should be borne in mind in comparisons with the literature.

6.3.3 $1.9\mu m$ Experimental Values

Unfortunately many organic molecules of interest in optical applications are highly coloured. This means that often the experiment cannot be performed at 1.064 μm as the frequency doubled signal would be absorbed. Using a Raman shifter it is possible to achieve a fundamental wavelength of 1.907 μm so the frequency doubled signal at 954 nm is far from the absorption band. However the main organic solvents available almost always absorb at 1.907 μm (cf. figure 6.14), so a different type of cell was used, with a shorter optical pathlength ($\sim$ 0.5 mm, cf. figure 6.15).

The results shown here are for only one compound, DEMI, which due to its highly reactive nature, meant that the standard EFISH setup had to
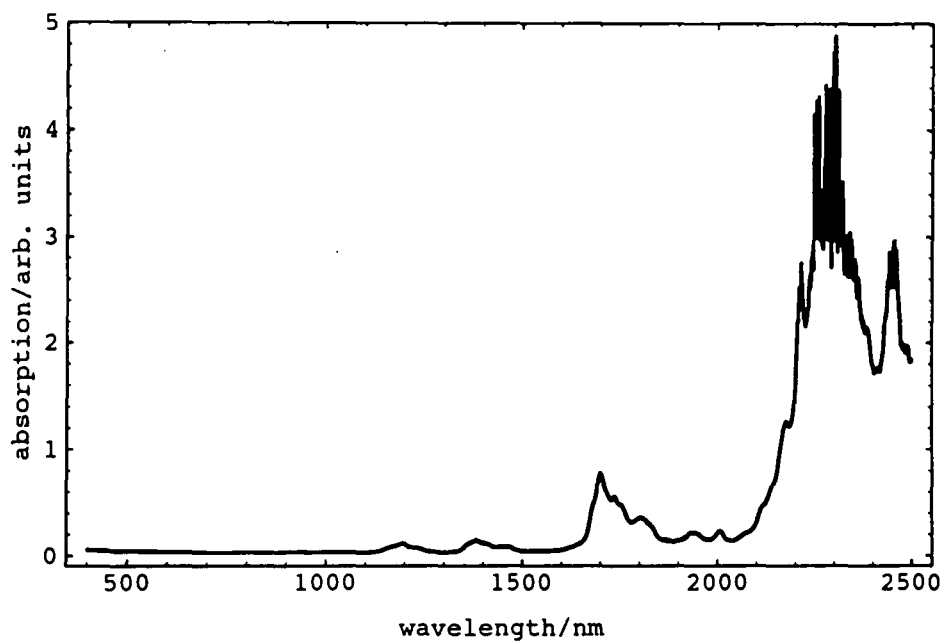
Figure 6.14: Absorption Spectrum of DMF
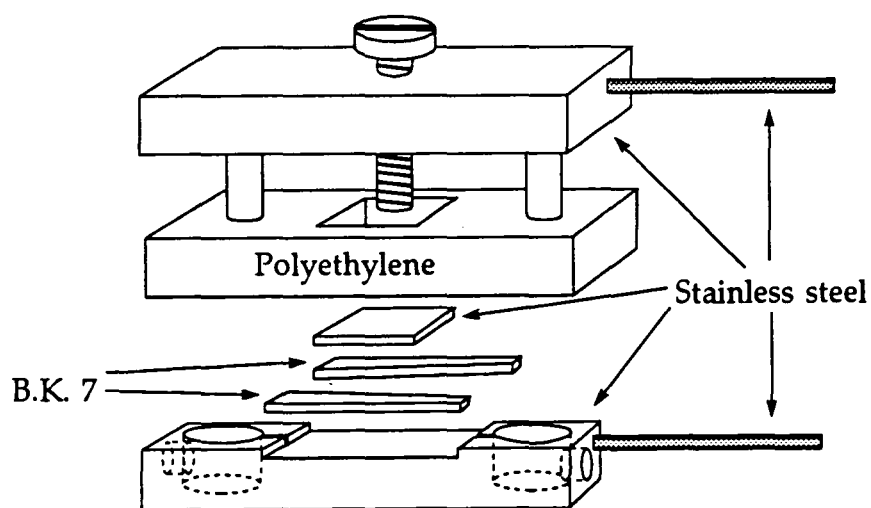
Figure 6.15: Cell (1.907 μm Design)

be modified. As DEMI is one example of a larger set of related compounds with high intrinsic dipole moment these modifications should enable their β values to be measured.

Modifications

DEMI only dissolves appeciably in DMF, that is up to 16 mg in 10 ml. If wet DMF is used DEMI solvation effects occur very quickly, on the order 10 minutes for 5 mg in 20 ml. The whole experiment had to be performed with as little contact with water as possible. In laboratory grade solvents DEMI is very light sensitive but with properly dried solvents, and under nitrogen this does not prove to be a difficulty. Due to its sensitivity to water the method of adding solvent in situ cannot be risked. This results in having to clean, dry, and refill the cell between scans. A quartz scan was taken for each concentration as day to day drift in the laser was more critical, as the powdered NPP reference was more prone to changes in the focusing position. For this reason as soon as a DEMI scan was taken the quartz was taken immediately without switching the laser off or even changing the power.

With the results of the solution preparation studies showing such a susceptibility to water contamination, the insulating layer chosen was PTFE because it is impervious to water. After repeated experiments with differing concentrations where no signal was discerned it was noticed that the solutions had become opaque. Running a new solution with just the laser and no applied field did not appeciably change the solution. Upon applying just the field, only a few minutes was required before the solution became opaque. If the cell was illuminated it was noticed that in the early stages the solution turned purple at the edges of the cathode. From this it was surmised that

water could be trapped in the PTFE due to its sintered fabrication. At the conjunction of the cathode and PTFE the DEMI becomes absorbing, reducing any signal to values too low to be detected. This problem persists even when the cell was stored under vacuum prior to filling.

The insulating layer was changed to polyethylene as it is relatively resistant to solvents and is non porous and so should not take up water. Upon applying a field this time, a fine layer of bubbles was observed on the cathode. Over a period of fifteen minutes the solution turned from bright blue through yellow and finally clear. At this point there was field breakdown across the now large gas bubbles. This was interpreted as an electrochemical reduction at the positive charge centred on the nitrogen (cf. fig 3.1). The negative charge on the other end of the molecule however is spread round the aromatic ring and therefore less susceptible to oxidative electrochemistry.

If a thin enough charge trapping layer can be deposited on the cathode then it was thought that the reduction reaction could be stopped, enabling a field to be sustained across the solution. Telene (cf. § 7.6.1) was chosen because as a pure hydrocarbon it should trap any electrons from the cathode. It does not dissolve in DMF, and it is very hydrophobic. About 3 μm thick layers of Telene were spun onto the cathode. These layers could sustain fields up to 50 statvolts per *cm* before breaking down and the solution being reduced. These layers therefore could sustain enough of a field for a signal to be measured and are thin enough that the relative permittivity of Telene means a change of field across the solution of < 5%. Figures 6.16 through to 6.21 show the fringes resulting from scans at different concentrations. Associated with each scan the fringes for the quartz reference are shown.

The high base line in these fringes compared to the ones taken at 1.064
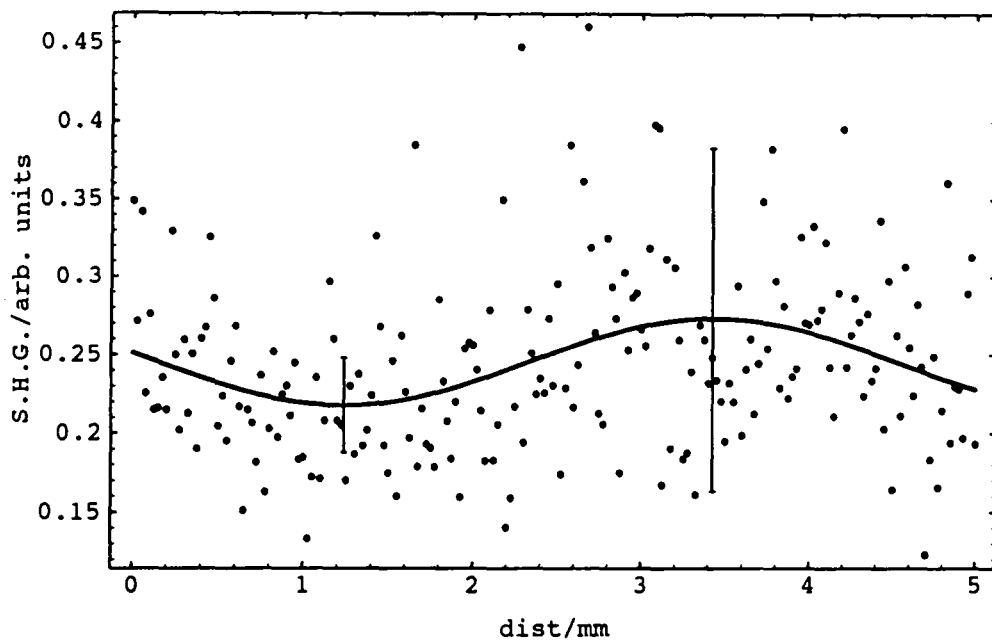
Figure 6.16: DEMI 0.08×10^{-2} Weight Fraction
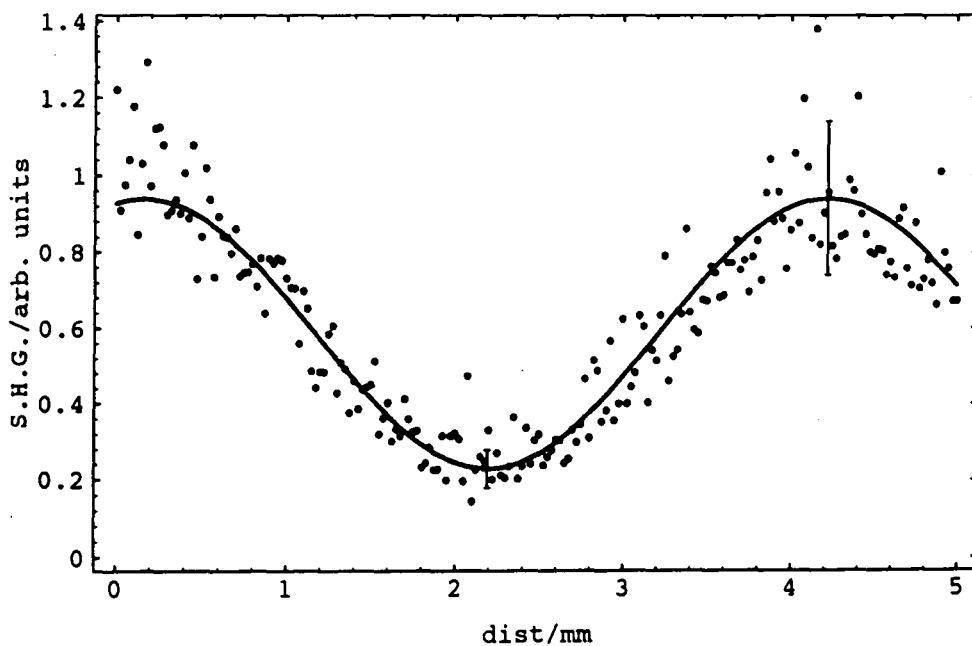
Figure 6.17: Quartz Associated with 0.08×10^{-2} Weight Fraction
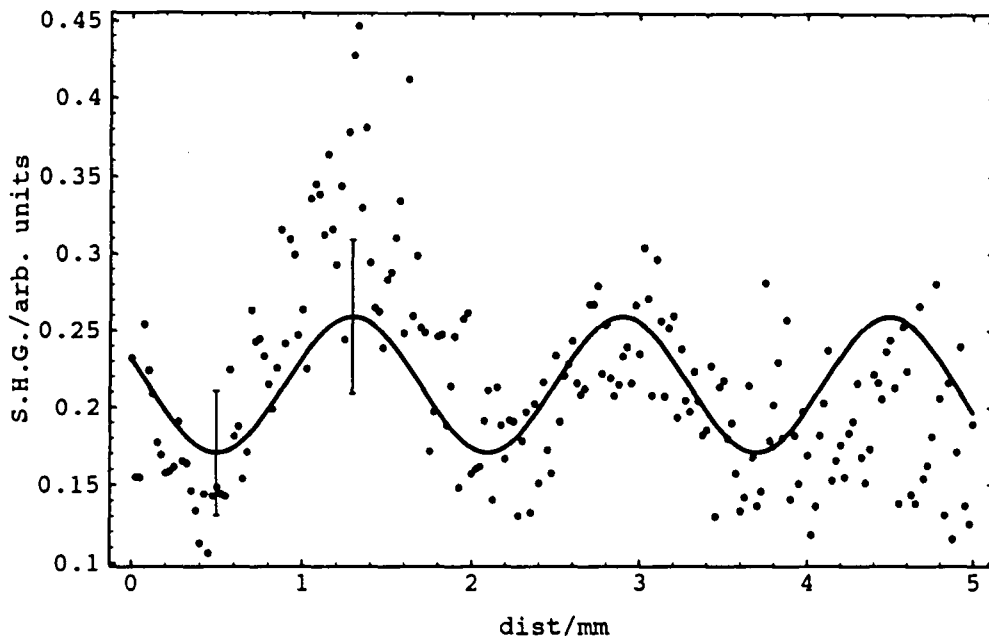
Figure 6.18: DEMI 0.10×10^{-2} Weight Fraction
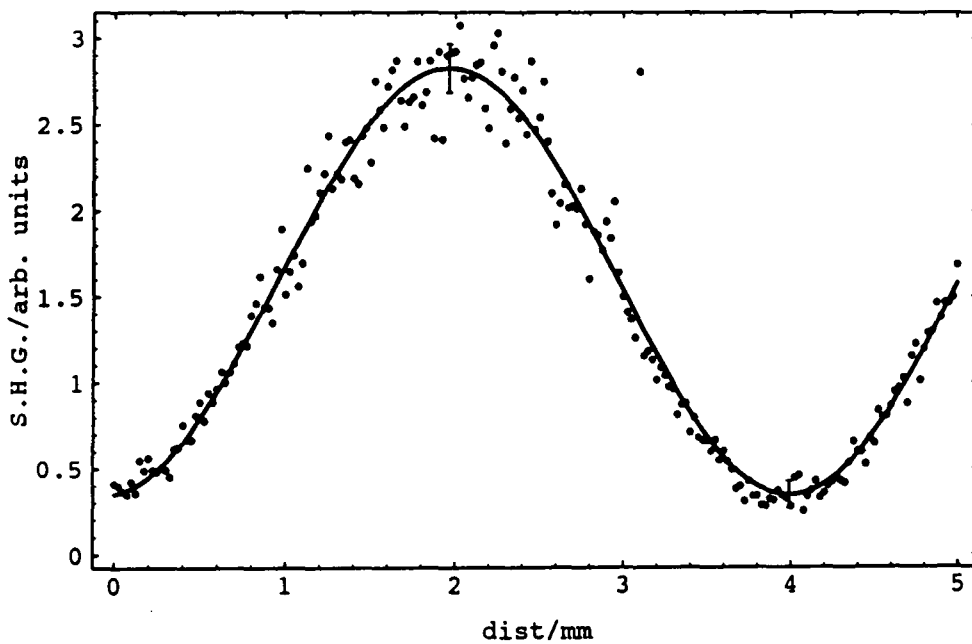
Figure 6.19: Quartz Associated with 0.10×10^{-2} Weight Fraction
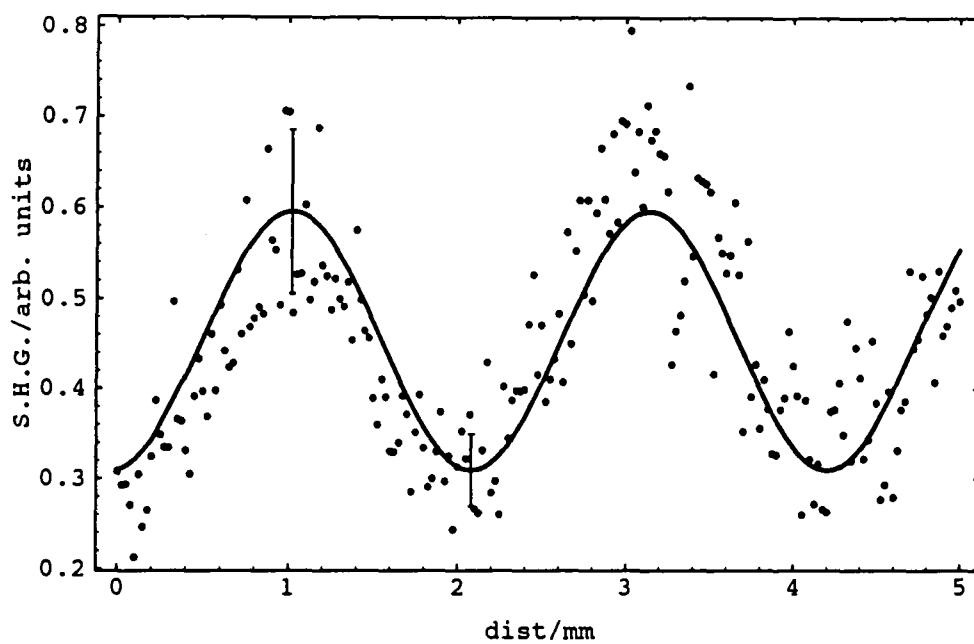
Figure 6.20: DEMI 0.16×10^{-2} Weight Fraction
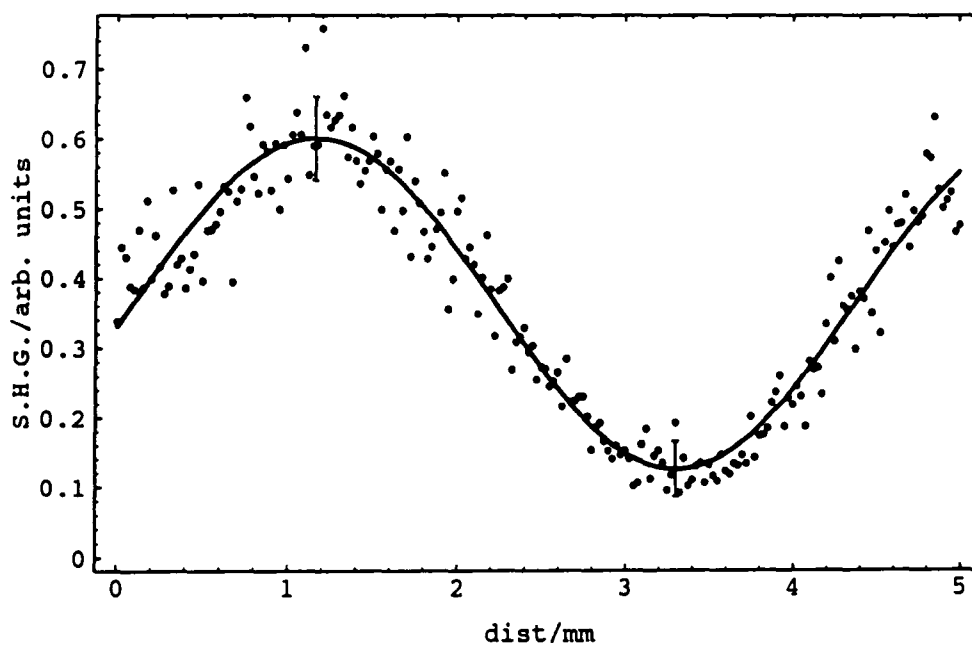
Figure 6.21: Quartz Associated 0.16×10^{-2} Weight Fraction

Material	DEMI
Solvent	DMF
$\Gamma_0/10^{-14}esu$	-3.0 ± 0.4
$\partial\Gamma_m/\partial(wf)\|_0/10^{-12}esu$	526 ± 42
$\partial\epsilon'_m/\partial(wf)\|_0$	9000 ± 550
$\mu/Debye$	45 ± 10
$\mu\beta_\omega/10^{-48}esu$	8550
$\beta_\omega/10^{-30}esu$	190 ± 50
$\lambda_{\max}/10^{-9}m$	667
$\beta_0/10^{-30}esu$	85 ± 23
$\mu\beta_0/10^{-48}esu$	3825

Table 6.4: Summary of DEMI results

μm is due to a background of second harmonic as mentioned previously. It should be noted that the coherence length change between concentrations was because the windows are not slotted into grooves as previously but held with silicon vacuum grease. The grease means that the angle of the defining windows was different between scans. This angle was calculated from micrometer readings taken after the scan, and lead to values of l_c and n_ω. The coherence length was calculated from the measured angle and half the period of the fringes. The refractive index was found from [75]

$$n_\omega = n_{2\omega} - \frac{\lambda}{4l_c} \qquad (6.2)$$

The value derived from this data can be seen in table 6.4. The value for β_0 was obtained by correcting for dispersion using a two–level model. This is now known to be a poor method for DEMI. Under certain conditions of reaction field this error can account for a factor of at least two. However even this cannot account for the discrepancy between the measured value of β_0 and the computed value [104]. In the crystal, for example, the computed

value for β_0 is -550 $\times 10^{-30} esu$. Coupled with a computed value of 35D for the dipole moment this gives $\mu\beta_0 = 19250 \times 10^{-48} esu$ which is the largest figure of merit known at this time. Clearly there have been problems in the EFISH measurement which need resolving if these large predicted values are to be verified.

Chapter 7

Results: Devices

7.1 Introduction

This chapter will present the results for the experiments necessary to characterise materials for waveguide devices. Results from a prototype amplitude modulator with a commercial polymer and preliminary work on channel fabrication are also presented.

Before any type of properties can be determined polymer solutions must be made and substrates must be cleaned. The methodology of this is described first, then waveguide fabrication detailed using both the spinning and the withdrawal techniques. With these simple slab waveguides refractive index measurements and loss measurements were taken. For the amplitude modulation and frequency doubling devices of interest the symmetry of the isotropic guide material must be broken. The method chosen here is fixed electrode poling, with the results of one to three layers presented. This leads up to the determination of the switching voltage required in a commercial polymer for an amplitude modulator configuration.

7.2 Sample Preparation

For waveguides to have low scattering loss, particles in the structure must be kept to a minimum. Cleanliness is also important to promote the adherence of the polymers to the substrate. To achieve this, all sample preparation was carried out in a clean room, with critical operations carried out in a class 100 clean air cabinet situated in the clean room.

7.2.1 Substrate Preparation

Most of this work was carried out using cut microscope slides 7.5x3x1 *mm*. Low refractive index polymers were measured with fused silica substrates, and poling studies with indium tin oxide (ITO) coated glass. However the same method was followed with all the withdrawal technique substrates.

The microscope slides were cut into quarters 1.5x3.75x1 *mm* using a diamond scribe. These were then wiped using lint free paper to remove as much of the obvious dirt as possible. Then each piece was placed individually in a glass sample bottle with $\approx$ 5% decon 90 and de–ionised water, and left in an ultrasonic bath for half an hour. They were then rinsed in three changes of de–ionised water with about fifteen minutes of ultrasonic treatment for each change. The excess water was blown off with a nitrogen gun and the substrates were then dried in a drying cabinet.

When the substrates are silicon wafers a slightly different method was used, as the wafers just have to be degreased. This was done by boiling for 5 minutes in trichloroethane, then repeating with fresh solvent. Finally they were spun dry with a little iso–propyl alchohol (IPA).

7.2.2 Solution Preparation

The substrate preparation was done in a clean room environment. The sample bottles were cleaned out with IPA and placed in an ultrasonic bath for 10 minutes, and the excess removed with a nitrogen gun. To avoid cross contamination the same magnetic stirrers were used with the same type of solutions each time. If the polymer did not dissolve easily, or was not homogenous it was possible to use the ultrasonic bath for up to 10 minutes to complete the process. Finally a hot plate could be used but usually it is better to use a different solvent as problems such as gelling can occur in these cases.

Once the polymer was dissolved the solution had to be filtered to remove any dust or other undissolved impurities. Depending on the viscosity one of two methods was used. For low viscosity solutions, the solution was filtered with a syringe and disposable filters. With solutions too viscous to filter by hand a nitrogen gas pressure filter was used. When possible the solutions were filtered down to 0.5 μm but if not they were filtered to 5 μm. The solutions were then left to stand for around 24 hours before use to let any bubbles clear.

7.3 Thickness Studies

Each polymer solution has to be calibrated to determine the thickness of films that can be produced. Although there have been studies to determine film thicknesses from viscosities [89], in practice it is usually easiest to calibrate the solutions. A typical polymer solution spun at 2000 revs per minute for 10 seconds gave films a few microns thick, and was a useful a starting point for further investigation. Similarly withdrawing a substrate from a solution at

Sample	Speed / (mm/min)	Thickness / μm
1	10	1.64
2	15	2.39
3	20	2.44

Table 7.1: Telene $3g$ in 20 ml of Cyclohexane

Sample	Speed / (mm/min)	Thickness / μm
1	10	0.65
2	15	0.70
3	20	0.95

Table 7.2: P4VP $3g$ in 25 ml of IPA

40 mm/min also gave films of a few microns. The thicknesses were measured using a surface profiler (Alpha Step). Tables 7.1 and 7.2 show the results of the withdrawal technique with two pure polymers.

The only polymer investigated for spinning was PVC, as it proved to be the only polymer suitable as a buffer layer in the trial device fabricated (cf. § 7.6.1. Using 10 % weight for weight (w/w) cyclohexanone at 1500 revs/min and 40 s spin time gave films of thickness 1.1 μm.

7.4 Loss Measurements

The loss measurement technique used was the method of two prism coupling, with the output prism being moved closer to the input prism. A coupling fluid, glycerol, was used so that the output coupling did not change. This was because it was found that coupling out from the scatter of a scratched film with a fibre did not provide enough signal using the 2 mW diode laser. The input was kept on mode zero throughout.
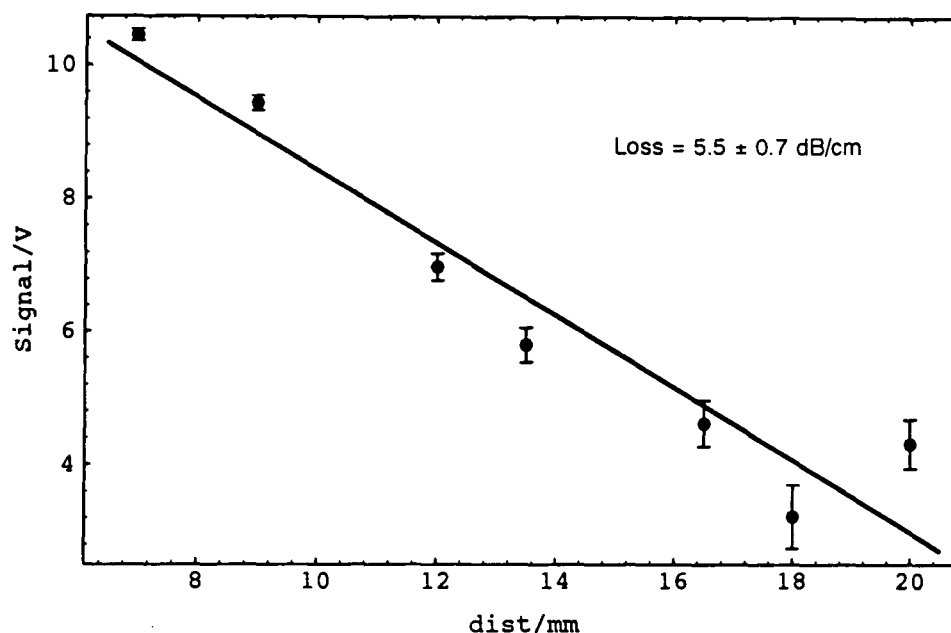
Figure 7.1: Loss Data (Doped DEMI Film 1)

The signal was measured with a 1×1 *mm* germanium photo–diode operating in its linear regime, which was found by calibrating with neutral density filters, and a lockin amplifier. After each measurement the film was scratched along the base of the output coupling prism. The film at the input coupling prism was scratched at the end of the set of measurements and was taken to be the zero point, with all distance measurements being taken relative to this.

A plot of 10 log(*Voltage*) versus the relative distance gave a gradient which is a measure of the guide loss in *dB/cm*. For a calibration pure PMMA films at 1.3 *μm* were taken but the loss in these films was too small to measure. Figure 7.1 through to figure 7.3 gives the losses for 2% *w/w* heat treated doped DEMI films in PMMA on fused silica. This gave losses on the order of 4.9 ± 0.6 *dB/cm* which is within losses cited in [29, 30] as a requirement for practical optical waveguides. Therefore this material can be used in a slab waveguide configuration device, as it is within tolerated losses.
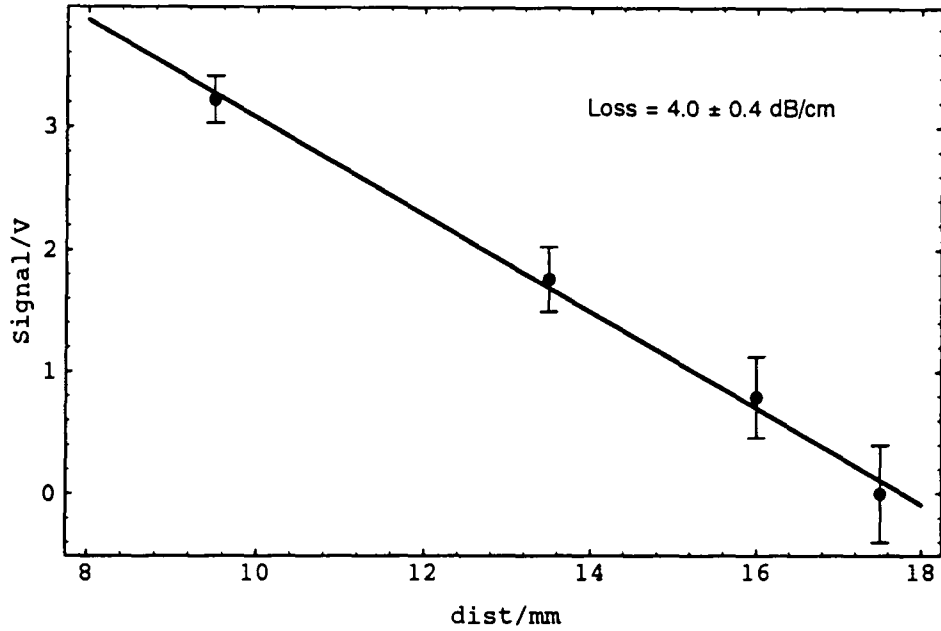
Figure 7.2: Loss Data (Doped DEMI Film 2)
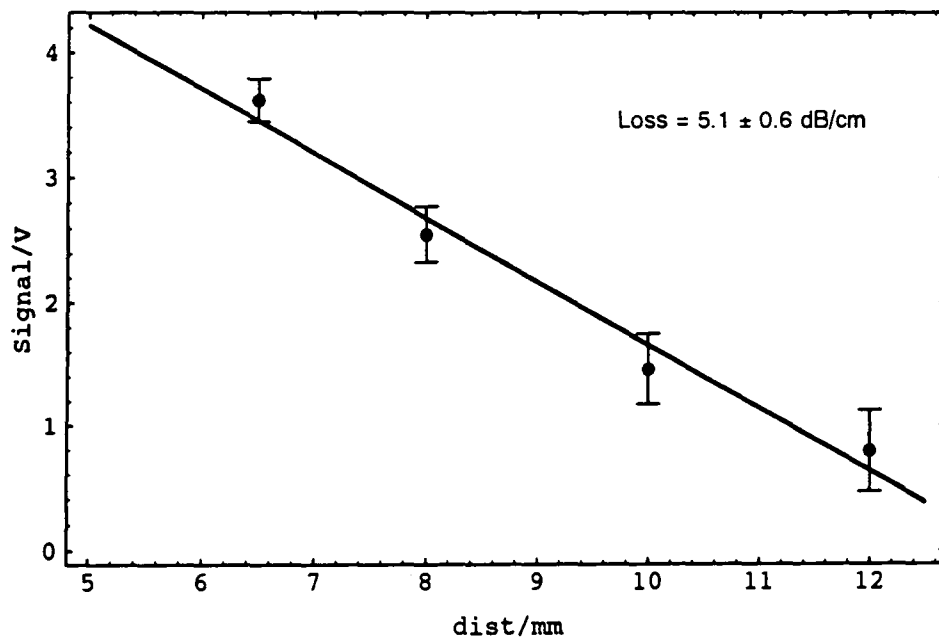
Figure 7.3: Loss Data (Doped DEMI Film 3)

7.5 Refractive Index Measurement

The general theory behind prism coupling has been described in § 5.4.2, so here only specifics to the particular setup used will be described.

The input laser was mounted with its polarisation at 45° to the vertical .This means that either TE or TM modes could be excited with a simple rotation of the polariser. In this configuration, with the films mounted vertically, vertical alignment will excite TE modes and horizontal alignment will excite TM modes.

The sample was mounted on two micrometer controlled translation stages which were mounted orthogonally to provide X-Y axis control of the sample. Underneath these was a lab–jack for Z axis control and a micrometer controlled rotation mount with a vernier scale that read to ± 4 mins. of arc. The samples were mounted on a U–shaped bracket screwed centrally on top. Using the translation stages the laser beam could now impinge on the centre of rotation of a film. The prism clamping arrangement employed a 'G'–clamp to which the prism was glued.

The prism was attached to the film by gently screwing the clamp until a coupling spot was seen. The coupling spot was an irregular clear area spreading from around the clamp spot, which indicated that the prism was close enough to the film for evanescent coupling into the waveguide. The translation stages were adjusted until the coupling spot and laser beam were coincident.

Another prism clamped to the film in the opposite sense acted as an output coupler. It was often helpful to avoid stray reflections, that could be confused with the modes lines, if the back face of the input coupler was blacked out.

Wavelength/nm	457.9	632.8	1300
SF6(RI)	1.83757	1.79883	1.76822
SF53(RI)	1.75413	1.72318	1.69773
fused–silica(RI)	1.46498	1.45702	1.44692

Table 7.3: Refractive Indices of the Glasses Used

To find the modes in the film it is best to start with the laser beam impinging on the film at a fairly steep angle so as to excite the substrate modes, which are seen as dots on the faces of the substrate. As the film was rotated to shallower angles these dots became further apart until the highest order mode of the film was excited, seen as a vertical line on the screen. Continuing in this direction will show up any other modes until mode zero which was the brightest and had the sharpest cut off. The angle for each mode was read off the vernier. The zero point was found by rotating the prism so the back reflection from the prism face travels back down the beam path. The prism angle was found by moving the prism out of the beam path and back reflecting off the substrate surface back down the beam path. This was done with an aperture placed as far down the beam path as possible.

Using the equations from § 5.4.2 and § 5.6, the mode indices and the effective film refractive index and thickness can be calculated. The refractive indices of the prisms at the laser wavelength were found using the Sellmier coefficients from the Schott Glass catalogue. In this case SF6 and SF53 glass prisms are used. Appendix A gives the programs that were written to calculate the film index, mode indices, and film thickness.

The wavelengths used were 457.9 nm, 632.8 nm, and 1300 nm, where the results of the calculations of the refractive indices of the various glasses and substrates can be found in table 7.3. A typical set of results to determine

Telene	
Mode Number	Mode Index
0	1.522 ± 0.004
1	1.511 ± 0.004
2	1.492 ± 0.003
3	1.466 ± 0.003

Table 7.4: Mode Indices for a 2.6 μm thick Telene film at 632.8 nm
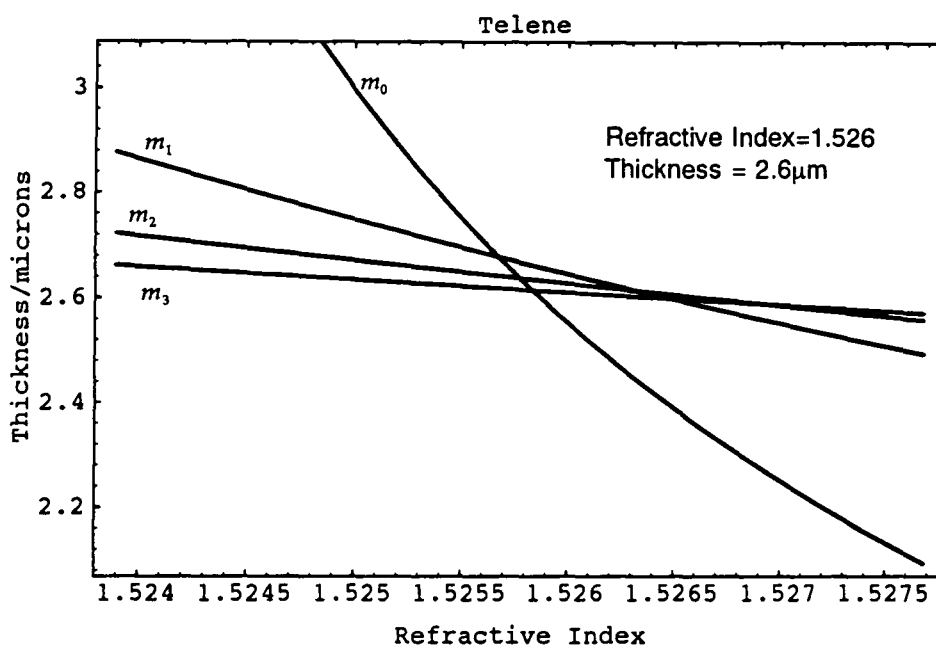
Figure 7.4: Mode dispersion curves for Telene

the refractive index are shown in table 7.4 which lists the mode indices of a "Telene" film. Using these mode indices and plotting a dispersion curve of thickness versus refractive index the least squares crossing point of these curves gives the film thickness and film index. The result of this process can be seen in figure 7.4. Table 7.5 gives the refractive indices and thicknesses of the pure polymer films measured in this way at 632.8 nm.

For doped polymer films the dopant can absorb too much for the two prism method to be used to measure the refractive index. In this case the M–Line technique was used (cf. Section 5.6). As only the width of the

Polymer	Refractive Index	Thickness/μm
PMMA	1.483	3.3
PVA	1.497	3.0
Telene	1.526	2.6
PVC	1.541	2.8
P4VP	1.566	1.9
PC	1.580	2.2

Table 7.5: Polymer Refractive Indices at 632.8 nm
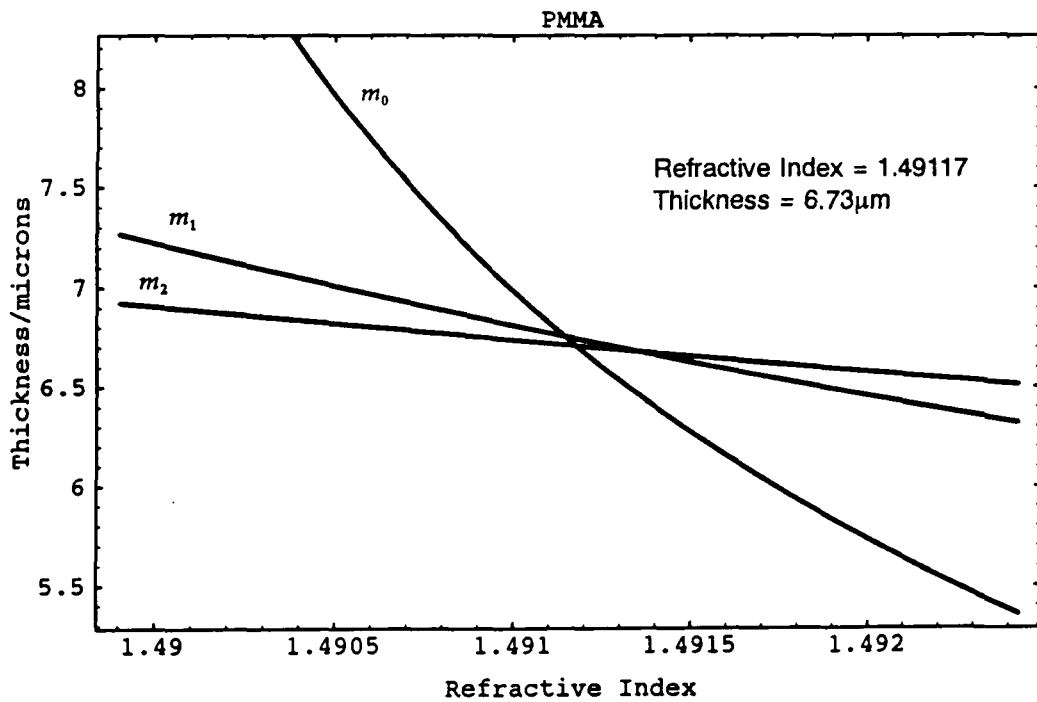
Figure 7.5: Mode Dispersion Curves for PMMA (Film 1) at 1.3 μm
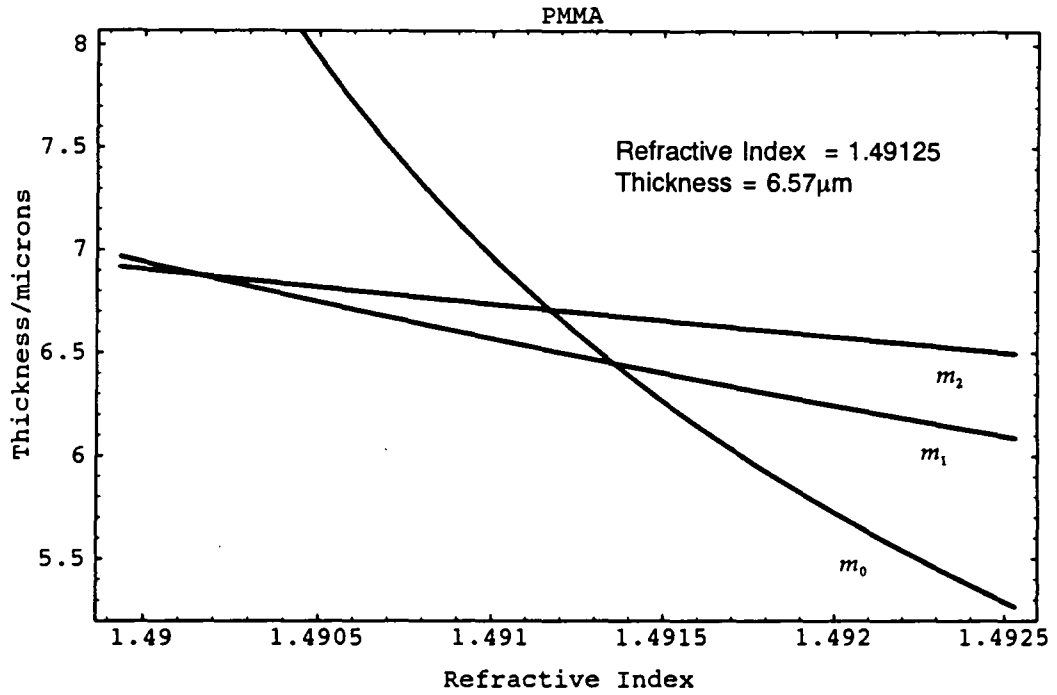
Figure 7.6: Mode Dispersion Curves for PMMA (Film 2) at 1.3 μm
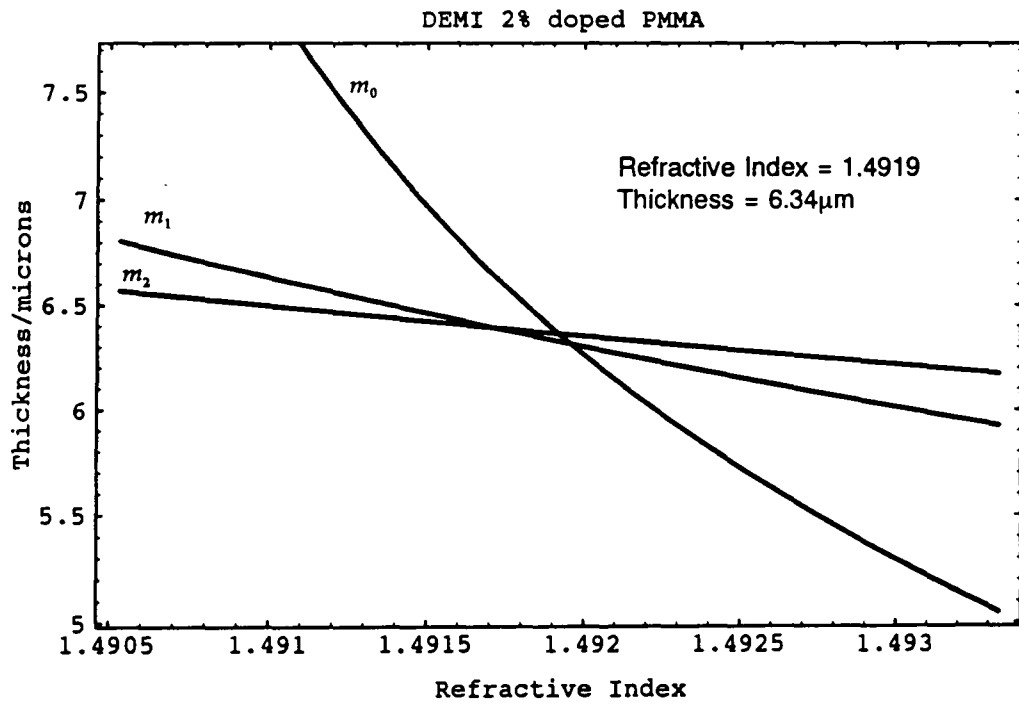
Figure 7.7: Mode Dispersion Curves for DEMI (Film 1) at 1.3 μm

DEMI 2% doped PMMA

Refractive Index = 1.4932
Thickness = 6.01μm
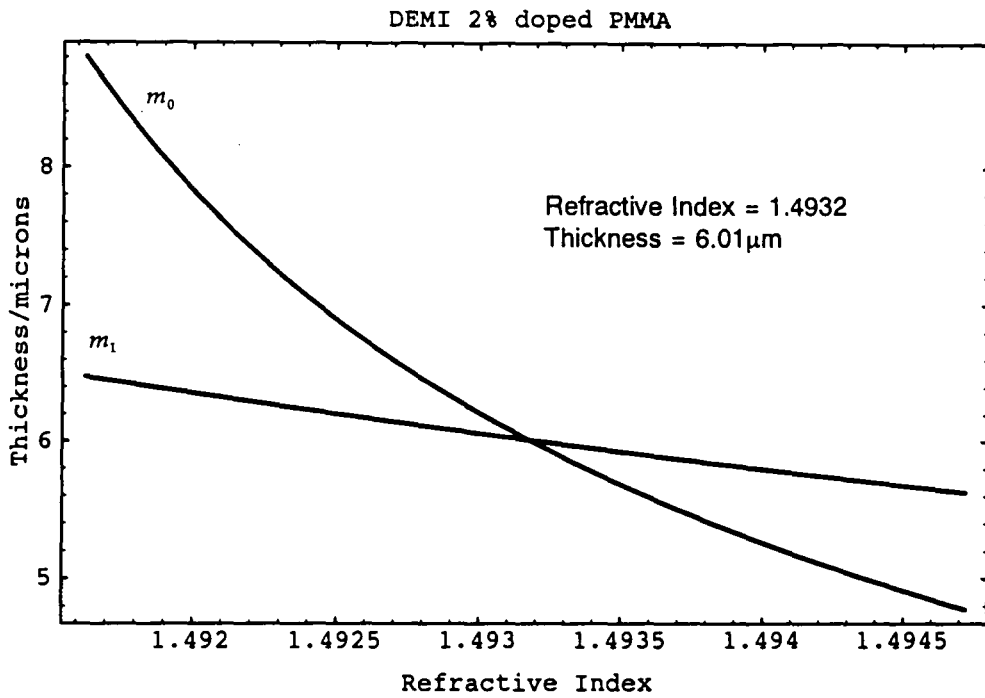
Figure 7.8: Mode Dispersion Curves for DEMI Film at 1.3 μm

DEMI 2% doped PMMA

Refractive Index = 1.6091
Thickness = 1.25μm
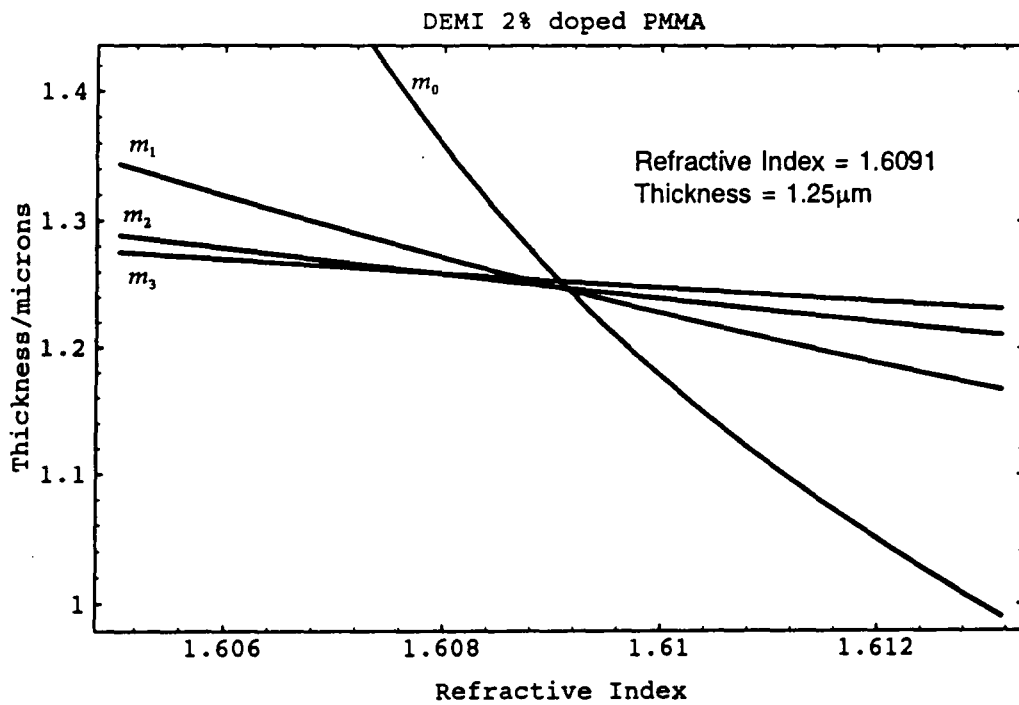
Figure 7.9: Mode Dispersion Curves for DEMI Film at 457.9 nm

Film	Mode number	Mode Index
PMMA film 1	0	1.489 ± 0.003
	1	1.481 ± 0.003
	2	1.469 ± 0.003
PMMA film 2	0	1.489 ± 0.003
	1	1.480 ± 0.003
	2	1.469 ± 0.003
DEMI 2% doped PMMA	0	1.489 ± 0.003
	1	1.481 ± 0.003
	2	1.467 ± 0.003
DEMI 2% doped PMMA	0	1.490 ± 0.003
	1	1.481 ± 0.003
DEMI 2% doped PMMA at 457.9 nm	0	1.601 ± 0.004
	1	1.576 ± 0.004
	2	1.536 ± 0.004
	3	1.481 ± 0.003

Table 7.6: Refractive Index Data at 1.3 μm

laser beam is guided, very absorbing films can be measured in this way. For extremely absorbing films mode lines are not observed but only a drop in the reflectivity of the laser beam. Using this method DEMI doped PMMA films were measured at 1.3 μm and 457.9 nm. (cf. table 7.6 and figures 7.5 to 7.9).

This means that the refractive index of a thin film can be determined right across the wavelength range and is not constrained by the material's absorption spectrum. In this way anomalous dispersion has been measured for DEMI doped films [105].

7.6 Poling

Most of the poling experiments carried out were done in the context of fabricating a proof of principle device, an amplitude modulator.
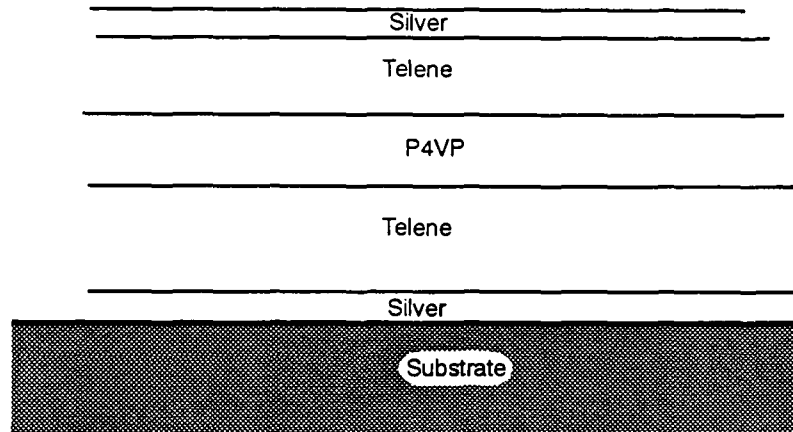
Figure 7.10: Schematic of Slab Waveguide Amplitude Modulator

7.6.1 Amplitude Modulator

Design

The general requirements for an efficient slab modulator are:

- Mono–mode operation [2].

- Refractive index of the optical buffer layers is close to, but lower than that of the guide layer [106].

- Optical buffer layers are sufficiently thick to prevent losses from absorption in the electrodes.

The guide layer was P4VP with a refractive index of 1.566 at 632.8 nm. Telene, a hydrocarbon thermoplastic, manufactured by B.F. Goodrich was chosen as the buffer, as the index was less than that of P4VP (cf. table 7.5) and was solvent compatible. That is the solvent for P4VP was a non–solvent for Telene, and vice versa. Figure 7.10 gives a schematic of the structure under consideration. Using the refractive indices of the polymers chosen and the criteria of mono–mode operation, the program NLAYER was used

[107, 108] which gave the the mode profile (cf. figure 7.11). This figure shows that the active layer has to be 0.8 μm thick and the optical buffer layers have to be at least 1 μm thick if the mode is not to interact with the electrodes. The mode is TM as the electrodes are in a transverse configuration, so that the guided wave interacts with the applied electric field.

§ 7.3 shows that Telene can easily be dipped at greater than 1 μm thickness, with 2.4 μm being chosen, as this is the most repeatable thickness. P4VP could be dipped at less than 0.8 μm using around 15 mm/min for the concentration of solution used. If a P4VP layer was dipped onto a baked Telene film the overall thickness was a linear combination of the individual thicknesses, which meant that the first stage of the structure could be realised. The second stage was completed when the Telene top layer also added as a linear combination of the individual thicknesses. However, Telene did not adhere to a metallised substrate, even using a silanisation procedure. The design of the modulator was then changed so that PVC, refractive index 1.541, became the bottom layer as there was no problem with this polymer adhering to a metallised substrate. Due to solvent incompatability, [109] in that P4VP dissolves in cyclohexanone, the only suitable solvent for PVC, Telene was kept as the top layer. Figure 7.12 shows the new field profile, which relaxed the constraint on the thickness to 1.2 μm. Problems with filtering viscous PVC solutions had led to a double spinning technique, that gave thicknesses of $\sim 2\mu m$. This was possibly due to the low solubility of PVC in cyclohexanone.
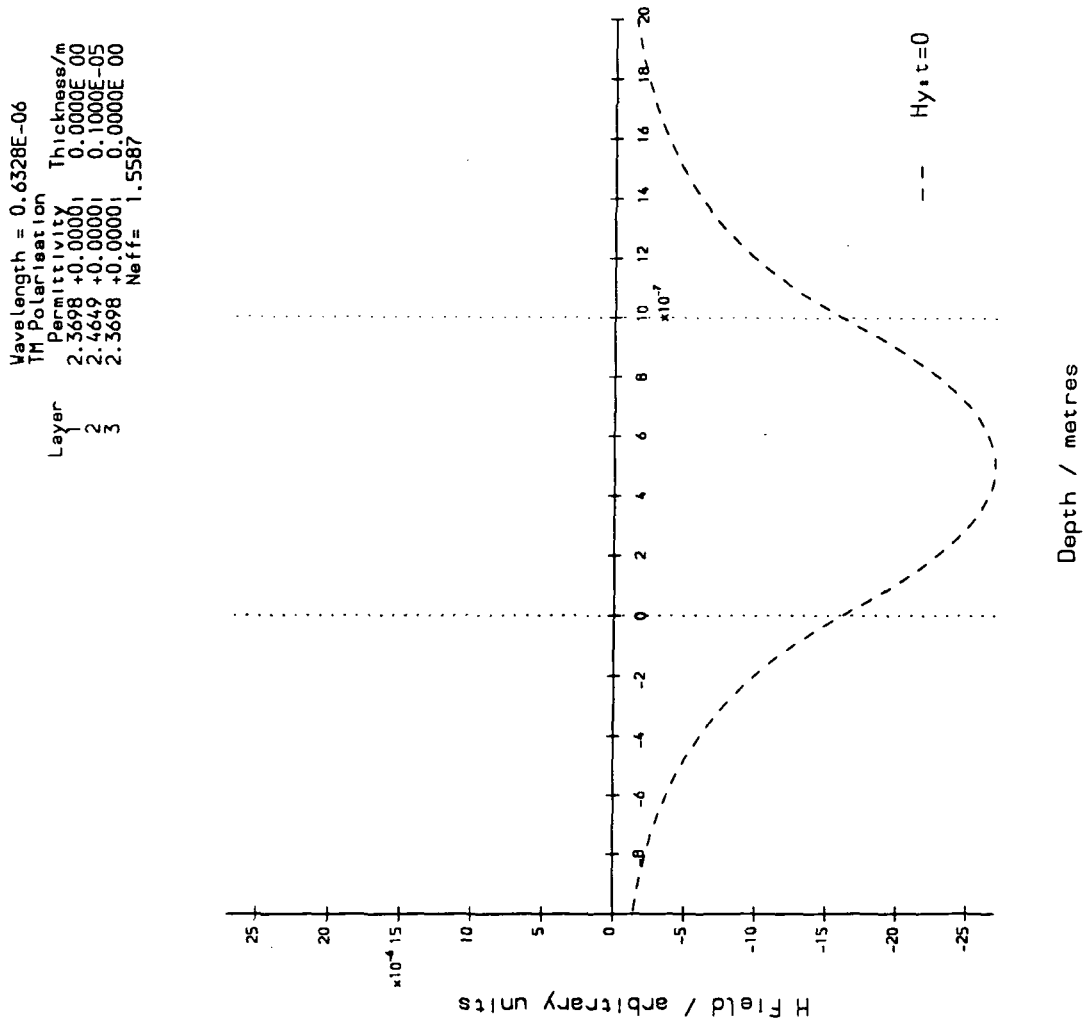
Figure 7.11: Mode Profile – Layer 1 = Telene, Layer 2 = P4VP, Layer 3 = Telene
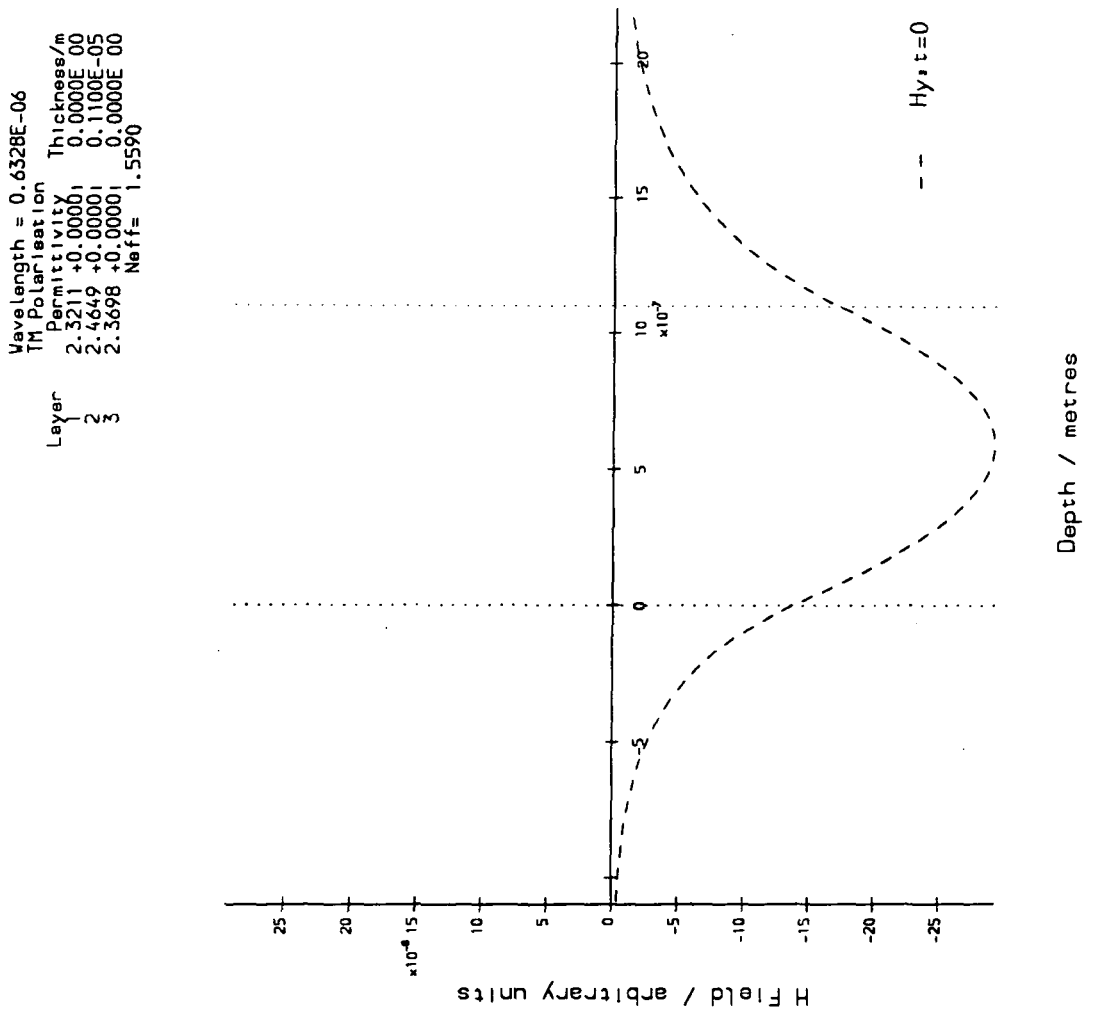
Figure 7.12: Mode Profile – Layer 1 = PVC, Layer 2 = P4VP, Layer 3 = Telene

Poling Studies

In this section the linear electro–optic response of each of the layers will be presented, with r_{33} being the measured value. This is important as the buffer layers should not to possess any coefficient which could be attributed to the active layer under study.

The current in this circuit was monitored using an electrometer during the whole poling procedure. The samples were tested by measuring their r_{33} coefficient as described in § 5.7. This has the advantage of simple sample preparation and a straight forward measurement technique.

In this case the films were cast onto ITO coated glass with the top electrode being silver which was evaporated onto the film using a simple vacuum evaporator and a molybdenum boat. The poling scheme was:

- Single layer PVC.

- Single layer Telene.

- PVC overcoated with P4VP.

- PVC layer, P4VP layer, and overcoated with P4VP

with values for P4VP taken as those measured by Karakus [50]. These systems gave the following current density versus temperature graphs (cf. figures 7.13–7.16). The rise in current flow can be interpreted as a phase transition where the dipoles in the polymer are able to align and the fixed charges become mobile, but the current is still at pre–breakdown levels [50]. The measured electro–optic coefficients (cf. figure 5.7) from these samples can be seen in table 7.7. PVC and Telene did not give a measurable response, and so did not contribute to the response of the modulator. It should be noted
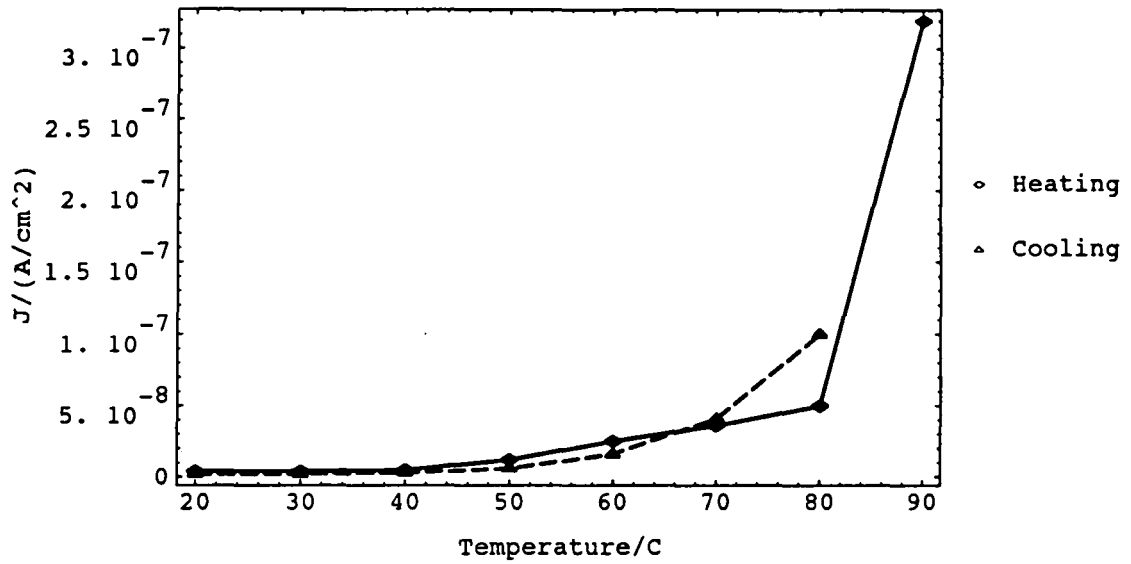
Figure 7.13: Poling Curve Single Layer PVC
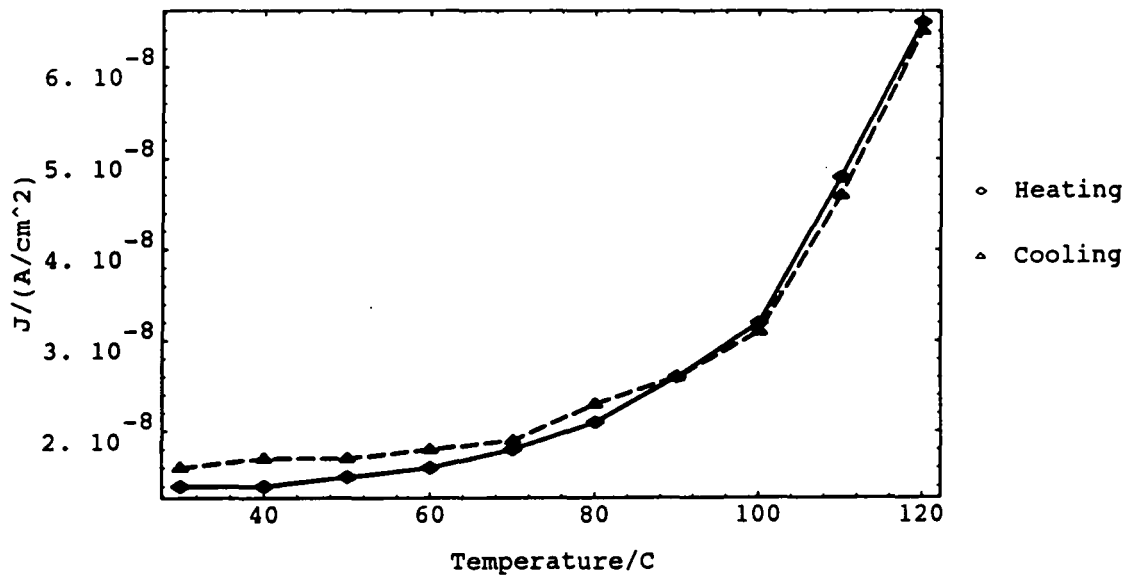
Figure 7.14: Poling Curve Single Layer Telene
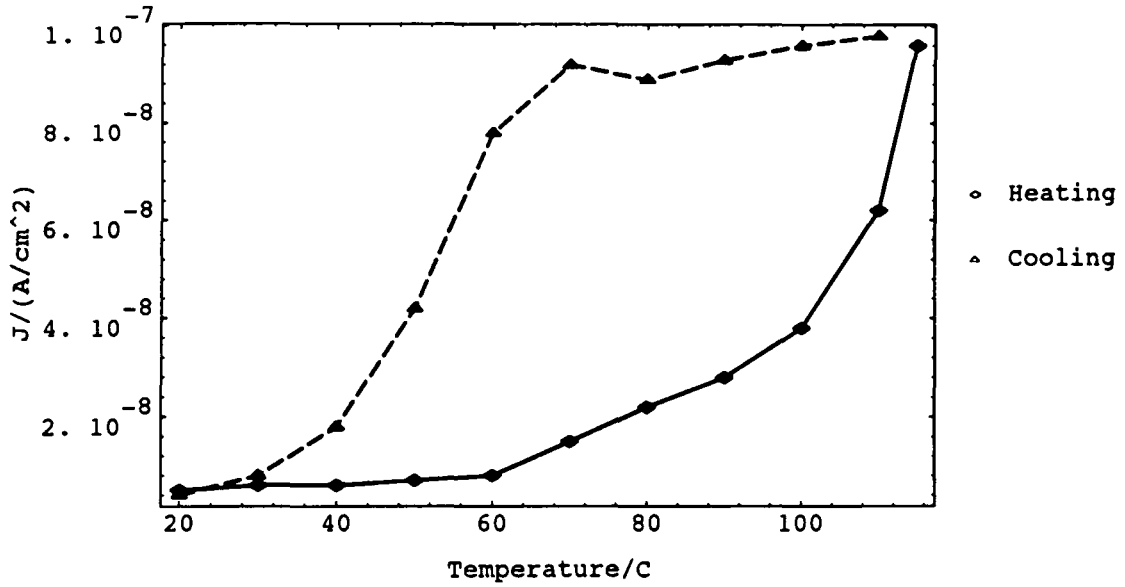
Figure 7.15: Poling Curve Double Layer PVC — P4VP
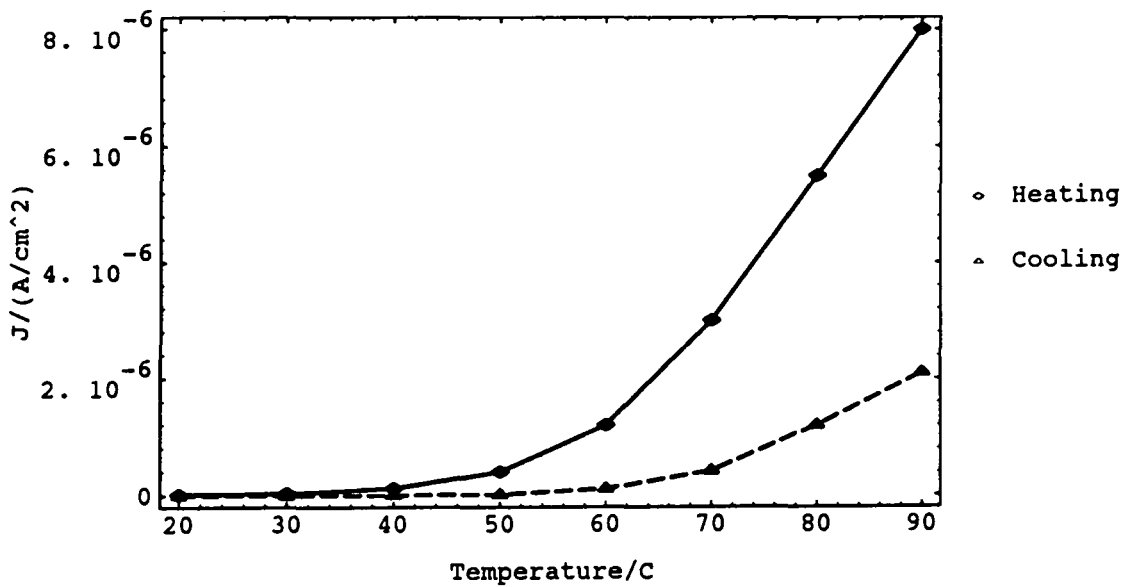
Figure 7.16: Poling Curve Triple Layer PVC — P4VP — Telene

Sample	Poling Field/$(V/\mu m)$	$r_{33}/(pm/V)$
PVC	2.5	not measurable
Telene	1.5	not measurable
PVC + P4VP	1	0.14
PVC + P4VP Telene	2.5	0.06

Table 7.7: r_{33} Coefficients

Sample	Poling Field/$(V/\mu m)$	$r_{33}/(pm/V)$
PVC + P4VP + PVC	2.8	1.8
P4VP	8.8	2.8

Table 7.8: Final Modulator System

that there was a larger drop in r_{33} when the Telene top layer was added. It was thought that this was due to most of the poling field dropping across the Telene as it is an extremely efficient insulator, and consequently the P4VP layer did not pole efficiently [81]. Since PVC spins satisfactorily on itself and P4VP was less soluble in cylohexanone than PVC, it follows that PVC could, after all, be used as the top buffer layer. This again changed the mode characteristics of the device. (cf. figure 7.17). From inspection of the field profile it can be seen that the P4VP layer had to be reduced in thickness to 1 μm to retain mono–mode operation. The poling characteristics of this system can be seen in figure 7.18. Table 7.8 shows the r_{33} of the complete system compared to a single layer of P4VP. Table 7.8 shows that the PVC–P4VP–PVC system gave a comparable response to the single layer [50]. That is the buffer layers have not reduced the poling ability of P4VP so as to make the modulator unviable.
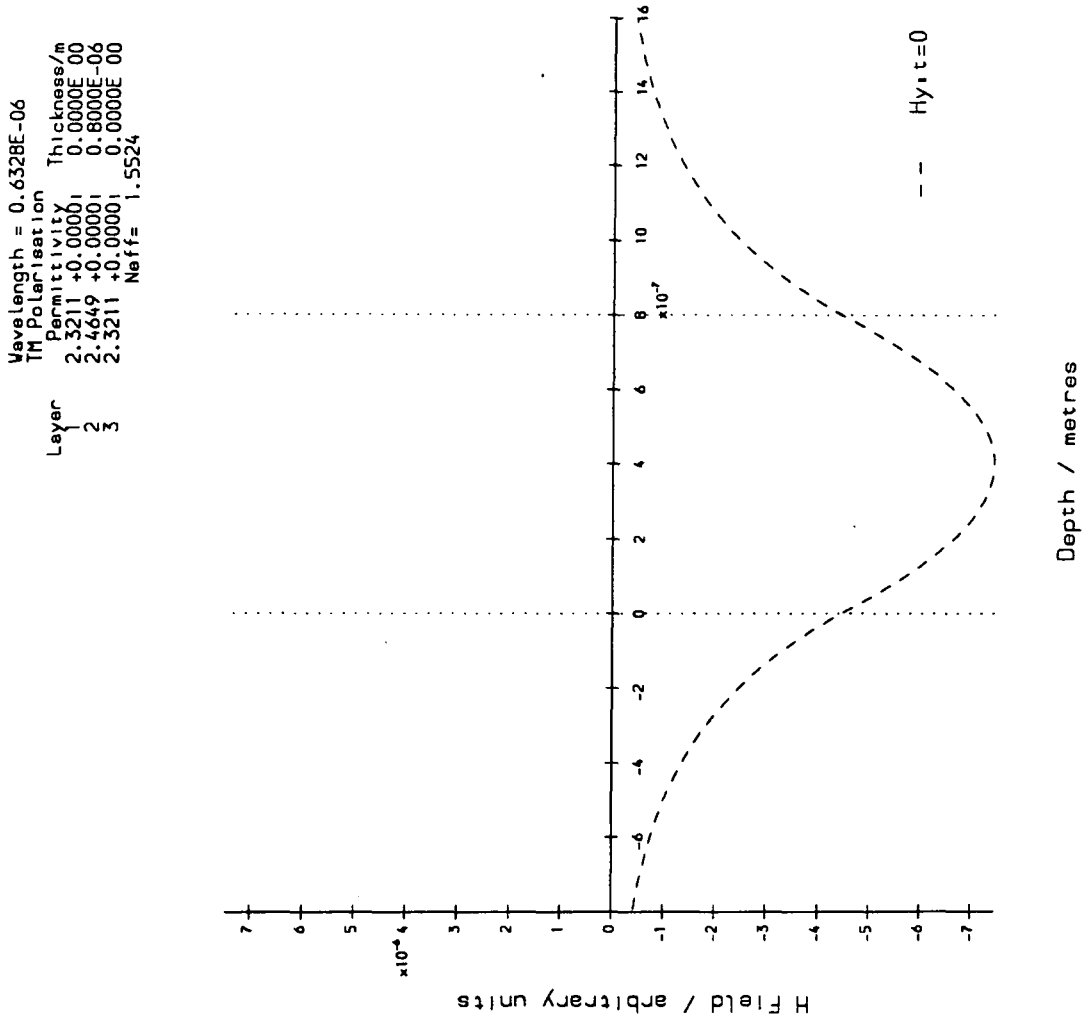
Figure 7.17: Mode Profile – Layer 1 = PVC, Layer 2 = P4VP, Layer 3 = PVC
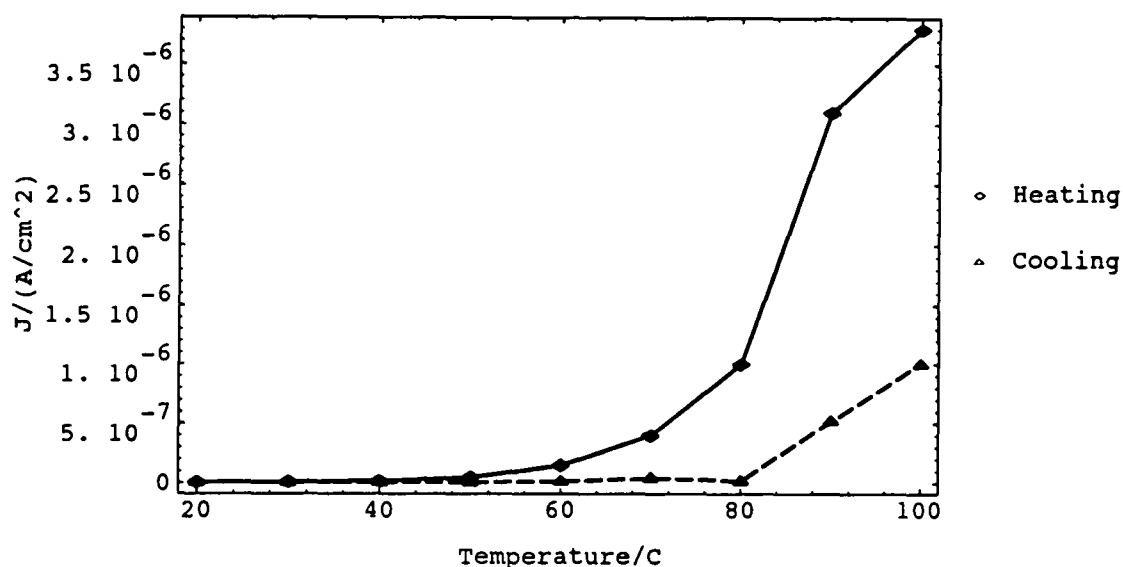
Figure 7.18: Poling Curve (PVC — P4VP — PVC)

7.7 Amplitude Modulator

This section describes the actual modulator system. Previously an ITO substrate was used but now metallised silcon substrates are used instead. Using silicon substrates enables the waveguide device to be cleaved and the laser beam introduced directly (cf. § 5.4.1) rather than risk damaging the film with a prism coupler. The microscope objectives used were mounted on X-Y-Z translation stages to focus the laser beam onto the cleaved face.

The problem of silver adhering to the substrate was remedied by pre-metallisation of the substrate with chrome, which adheres well, and the silver bonds to the chrome. The PVC was spun on to a single 3" substrate and the film baked in the usual way. The substrate was then cleaved to form 1 *cm* wide strips that could be dip coated with P4VP. The substrates were cleaved with a diamond scribe, by introducing a defect at the edge which propagates along one of the fault planes. The P4VP was dipped in the usual way onto

the substrate, and after baking the PVC top layer was spun on as before. A top electrode was evaporated onto the device by placing a rectangular (5 × 3 mm) mask of aluminium foil on top of the device. The final cleaving of the device end–faces was the most difficult as PVC adhesion was still a problem. It was found that if a greater pressure was applied to the side where the defect was introduced, compared to the other side more than 80 % yield could be achieved. The modulation voltage was applied through 48 SWG copper wire held in place at the edge of the device with epoxy and attached to the electrodes with silver paint.

The device was mounted onto the Z translation stage with a small spring loaded clip. The laser beam was introduced with a microscope objective lens where the correct focusing distance was found by observing the far field back reflection to obtain a small point, confirming a collimated reflection. From the small amount of scatter in the film a mode could be observed which could be coupled out with another microscope objective. The output was observed as a collimated horizontal line (cf. figure 5.2). Direct modulation of the beam could be seen on an oscilloscope and gave an estimated V_π of $120V$ as only 80 % modulation was produced. However this method gives a much less ambiguous measure of r_{33} compared to the reflection technique, as less approximations are needed. From the reflection technique V_π was estimated at $90V$ from Eq. 5.29 suggesting that the reflection technique gave an over estimation of r_{33}.

7.8 Channel Fabrication

Initial studies of channel fabrication using reactive ion etching (RIE) have been undertaken. Here an oxygen plasma was used to determine the etch rate of PVC. This was found to be 0.2 $\mu m/min$ at a pressure of 132 $mTorr$ and a power of $200W$. As a photolithography mask for the channel fabrication was used compatibility issues between etches and solvents had to be resolved. The PVC, photo–resist solvent, photo–resist etch and aluminium etch were found to be compatible and photo–resist channels were made of dimension 11 to 3 μm in width an $1cm$ in length. In theory, as there seems to be no compatibility problems an aluminium mask could be made and channels etched in PVC using RIE.

Chapter 8

Conclusion

8.1 Introduction

The field of molecular organic photonics is often presented in a compartmentalised fashion. However it should be apparent that a more complex interdependent approach is necessary. In this work the artificial split between molecular and device properties is maintained to avoid confusion in the experimental descriptions. Now the discussion will show that these two areas should not be viewed as separate.

8.2 Discussion

The measurements of molecular properties have determined the λ_{max}, μ, and β_0 for each of the molecules studied. For device properties the techniques to determine these have been shown with examples of each. The processes undergone in constructing an amplitude modulator as a case study were also shown.

Taking each of the molecular properties in turn it is instructive to see the

116

relevance they have to a device engineer. The absorption edge should be far away from the wavelengths used, as it is important for λ_{max} to be shifted to as short a wavelength as possible for reasonable guide lengths. At this point DEMI's unique properties become apparent. With its window in the "blue" it can take the advantage of resonance enhancement but there is no penalty with the absorption of the second harmonic. High dipole moment means that during poling the molecule will be subject to a greater torque, and so for a given applied field will tend to align more than for low dipole moment molecules. Therefore among molecules with an equivalent β, those with high μ will produce a larger effect. In devices this can mean smaller devices, lower modulating voltages, increased safety margins, enabling increased options on the optimisation of device performance. Similarly molecules aligned to the same degree will generate a larger effect with larger β values. The real step forwards are those molecules with high μ, high β, and with low absorption. Generally those molecules with high nonlinearity in general have an absorption edge shifted to longer wavelengths. Again the advantages of DEMI become apparent, with its high $\mu\beta$ coupled with a short wavelength window.

With these molecular properties playing such a direct role in device design it is obviously important to determine these accurately. This is not so important for λ_{max} but is for μ and β determination. Since the nonlinearity represented by β depends on the square of the input drive field any small error in β magnifies the error in the projected device performance. The dipole moment determination may not seem to matter to the same degree, but in fact it is just as important. This is because the EFISH technique returns $\mu\beta$, so any error in μ directly effects that of β. In the case of DEMI the

dipole moment has to be measured using a highly polar solvent, producing a μ value with an error of $\pm$ 10, which is not ideal.

The importance of measuring the molecular properties accurately has now been shown, therefore a number of what seem academic points do become of interest to the device engineer. That of the error in the quartz reference value assumes a much more prominent role since its error contributes so much to the overall value of β. Another important, and still unresolved source of error are the local field factors used, with several different versions scattered around the literature. These factors become more important with the highly polar solvents being used to dissolve the zwitterionic species. It is clear that the molecule's molecular properties can be radically dependent on local reaction fields. This has certainly been the case with DEMI where the values for μ measured were vastly different to the gas phase values. Ultimately this problem should be resolved when proper comparison is made with the hyper–Rayleigh scattering technique as no aligning field is used, and hence no local field factors are necessary.

At this stage mention should be made of the theoretical calculations involved with this work. When used to predict the molecular properties theoretical calculations have two important parts to play, that of screening suitable compounds for investigation, and corroborating the experimental values. In this work only the second part has been filled, where on the whole they have supported the results of the experimental work. However this is only the case where the local environment of the molecule is taken into account. This has important ramifications for molecules such as DEMI which change properties greatly between the gas phase and in solution. The effect is one the device engineer should be critically aware of, as disregarding a material

because of a low gas phase nonlinearity may be unjustified. An example of this is the poor $\mu\beta$ product of DEMI in the gas phase but an enhanced value in DMF similar to the type of local environment when doped into a polymer.

Although molecular properties are important in their own right, the experiments on device properties are only relevant to device applications. Measurements of these properties are often a short cut to investigation of suitable materials for devices. That is to say, if a doped polymer thin film is too lossy there is little to be gained from a thorough investigation of its molecular properties. Therefore the section on device properties is arranged in an order of experiments performed to eliminate an unsuitable material as efficiently as possible. At the point that poling studies are reached it is presumed that the molecule's nonlinearity and dipole moment are known and an estimate of the device's response has been calculated. This point ends the interdependency with the molecular properties and any device engineer can concentrate on their own discipline.

In conclusion it should be said that the main property a molecule of interest for device applications should have, is a high $\mu\beta$ product. If the product is low there is little interest for device work, where if it is high it can negate other factors that may be detrimental. i.e. low solubility is not a problem for extremely active molecules. DEMI does have a high $\mu\beta$, and as the first in a new class of compounds this bodes well for the future of photonics based on organic molecules.

8.3 Further Work

The obvious extension to this work would be to incorporate DEMI in a device configuration to determine whether it lives up to the promise of its high $\mu\beta_0$ product. This would be a frequency doubling waveguide using anomalous dispersion phase matching. It can be seen from the amount of work required to design and fabricate a simple amplitude modulator that this is no simple task. In conjunction with this it would certainly be interesting to examine the other molecules in the DEMI class of compounds, where from experience many unexpected avenues of research could occur. Specifically how the high nonlinearity and dipole moment versus stability trade-off develops would provide information about future directions for material optimisation. Another important area would be a careful study of the interface between measurements using the EFISH technique and that of hyper–Rayleigh scattering. This is especially relevant for zwitterionic molecules as they are near the limit of the application of EFISH. This may also give some new insight into the local field correction factors being used with polar solvents such as those used here.

•

Appendix A

The Mathematica program that fits a $\sin^2$ function to the EFISH data:

```
Needs["Statistics'NonlinearFit'"];
a1=.;a2=.;a3=.;a4=.;
f[x_] =
  N[a1 Sin[Pi x/2/a3 + a4/2]^2 + a2];
data=ReadList["Odyssey:data:NPP:NPPQZFAC.TXT",{Number,Number}];
g1=ListPlot[data];
max=2.4;
min=0.1;
peakToPeak=2.2;
distToMin=2;
lc=peakToPeak/2;
fit=NonlinearFit[data,f[x],x,
{{a1,max-min},{a2,min},{a3,lc},{a4,-distToMin Pi/lc}},
  ShowProgress->True]
g2=Plot[f[x]/. fit,{x,0,5},DisplayFunction->Identity];
Show[g1,g2,DisplayFunction->(Display[$Display, #1]&)];
(a1/2 + a2) /. fit
```

Mathematica package for slab waveguide analysis. The package includes functions to give the mode indices, and the film index and thickness from the mode indices.

```
(*********************************************

        Adapted from
        Roman E. Maeder: Programming in Mathematica,
        Second Edition, Addison-Wesley, 1991.


        *****************************************)


(* set up the package context, included any imports *)

BeginPackage["DG'Slab'"]

Needs["Statistics'DescriptiveStatistics'"]
(* read in any hidden imports *)

betaF::usage = "betaF[Angles,nc,np,prism angle]=mode indices ."

teModes::usage = " teModes[mode indices, ns, nc, lambda]=
ri and thickness "

tmModes::usage=" tmModes[mode indices, ns, nc, lambda]=
ri and thickness "


Begin["'Private'"]    (* begin the private context *)


te[modeIndex_List,nf_,ns_,nc_,k_] :=
  Module[{a,b,i1,i2,n,v},
    a=(ns^2-nc^2)/(nf^2-ns^2);
    b=(modeIndex^2-ns^2)/(nf^2-ns^2);
    i1=ArcTan[Sqrt[b/(1-b)]] + ArcTan[Sqrt[(b+a)/(1-b)]];
    i2=Table[i1[[n]]+(n-1) Pi,{n,Length[i1]}];
    v=i2/Sqrt[1-b];
    v/(k Sqrt[nf^2 - ns^2])
  ]

tm[modeIndex_List,nf_,ns_,nc_,k_] :=
  Module[{a,b,d,qs,i1,i2,n,v},
```

```
        qs=modeIndex^2/nf^2 + modeIndex^2/ns^2 - 1;
        a=nf^4/nc^4 * (ns^2-nc^2)/(nf^2-ns^2);
        b=(modeIndex^2-ns^2)/(nf^2-ns^2)*(nf^2)/(qs*ns^2);
        d=(1-ns^2)/nf^2 * (1-nc^2)/nf^2;
        i1=ArcTan[Sqrt[b/(1-b)]]+ArcTan[Sqrt[(b+a*(1-b*d))/(1-b)]];
        i2=Table[i1[[n]] + (n-1) Pi, {n,Length[i1]}];
        v=i2/(Sqrt[qs]*nf/ns*Sqrt[1-b]);
        v/(k Sqrt[nf^2-ns^2])
    ]


betaF[theta_List,nc_,np_,phi_] :=
    np Cos[90 Degree - phi Degree + ArcSin[nc Sin[
    theta Degree]/np]]/nc//N

teModes[modeIndex_List,ns_,nc_,lambda_] :=
    Module[{k,ri,filmIndex},
        k=2 Pi/lambda;
        ri=FindMinimum[Variance[te[modeIndex,nf,ns,nc,k]],
            {nf,{modeIndex[[1]]+1 10^(-5),modeIndex[[1]]+1 10^(-3)}},
            WorkingPrecision -> 20];
        filmIndex=nf /. ri[[2,1]];
        Plot[Evaluate[te[modeIndex,x,ns,nc,k] 1 10^6],
            {x,modeIndex[[1]]+(filmIndex-modeIndex[[1]])/2,
            filmIndex+(filmIndex-modeIndex[[1]])/2},
            AxesLabel -> {"RI", "Thickness (microns)"},
            AxesOrigin -> {modeIndex[[1]]+(filmIndex-
            modeIndex[[1]])/2,
            te[modeIndex,filmIndex+(filmIndex-modeIndex[[1]])/2,
            ns,nc,k][[1]]*1 10^6}
        ];
        Print["Thickness = ",N[Mean[te[modeIndex,
            filmIndex,ns,nc,k]],3]];
        Print["Refractive index = ",N[filmIndex,6]];
    ]

tmModes[modeIndex_List,ns_,nc_,lambda_] :=
    Module[{k,ri,filmIndex},
        k=2 Pi/lambda;
        ri=FindMinimum[Variance[tm[modeIndex,nf,ns,nc,k]],
            {nf,{modeIndex[[1]]+1 10^(-5),modeIndex[[1]]+
            1 10^(-3)}},
            WorkingPrecision -> 20];
        filmIndex=nf /. ri[[2,1]];
```

```
    Plot[Evaluate[tm[modeIndex,x,ns,nc,k] 1 10^6],
      {x,modeIndex[[1]]+(filmIndex-modeIndex[[1]])/2,
      filmIndex+(filmIndex-modeIndex[[1]])/2},
      AxesLabel -> {"RI", "Thickness (microns)"},
      AxesOrigin -> {modeIndex[[1]]+(filmIndex-
      modeIndex[[1]])/2,
      tm[modeIndex,filmIndex+(filmIndex-modeIndex[[1]])/2,
      ns,nc,k][[1]]*1 10^6}
    ];
    Print["Thickness = ",N[Mean[tm[modeIndex,
      filmIndex,ns,nc,k]],3]];
    Print["Refractive index = ",N[filmIndex,6]];
  ]


End[]           (* end the private context *)

Protect[ betaF,teModes,tmModes ]
(* protect exported symbols *)

EndPackage[]   (* end the package context *)
```

    C Program for control of the EFISH experiment.

```
/*
Program to control translation stage and perform
averaging via the Boxcar and aquire Maker fringe data
expt. Translation stage is started at 0 mm then moved
to a user specified distance. The distance between
measurements is 50 microns. The user declared average
is taken at each step.
WARNING   the red button on the rotary stage ramp
control stops any further communication.
If a total hang up occurs switch OFF all externals and
the computer and try again after a few seconds.
However minor hang up will occur on the boxcar if it
is not triggered but this will result in a time-out after
about a minute.*/

#include <math.h>
#include <graph.h>
#include <stdio.h>          /*  LIBRARIES */
#include <time.h>
#include <string.h>
#include <stdlib.h>
```

```
/*NEED to delete var errno in ieeeio.h to use this */
#include "ieeeio.h"        /* for C and I/O commands */
#include "iotmc60.h"
#include "iot_main.h"
#include "nrutil.h"         /* for dynamic array size */

#define STEPSIZE 25         /* step size in microns */
void Initialise();
void SHG(int averages);
void StepRot();
void DoorClose();

int averages, scanSize,  seconds,  steps;
int distMicrons, distmm;
float **data;
char sc[80],blockRead[80],move[80], bytedum[19];
char datafile[27], NameOfFile[10];
char stringAve[19], stringScan[19], *bytes;

main()
{
Initialise();
DoorClose();            /*  wait for door to close */
SHG(averages);          /* then do the averaging  */
free_cvector(bytes,0,scanSize+1);
/* releases memory from bytes array */
free_matrix(data,0,2,0,distMicrons/STEPSIZE+1);
exit(0);                                /* close files etc. */
}

void Initialise()
{
  int byted, byte1, byte2, byte3;

  ieeeinit();
  strcpy(datafile,"C:\\DG\\EFISH\\BETA\\");
  printf("Data File Name?\n");
  scanf("%s",NameOfFile);
  strcat(datafile,NameOfFile);
  strcat(datafile,".TXT");
  printf("Wait Time (seconds) ?\n");
  scanf("%d",&seconds);
  printf("Translation distance (mm) ?\n");
  scanf("%d",&distmm);
```

```
  distMicrons = distmm * 1000;
  printf("Number of averages?\n");
  scanf("%d",&averages);
  scanSize=averages*4;
  bytes=cvector(0,scanSize+1);
/* allocates a vector for scan data */
  data=matrix(0,2,0,distMicrons/STEPSIZE+1);
/* matrix for averaged data */
  ieeewt("REMOTE \n");   /* make externals listen */
  ieeewt("OUTPUT 16;MR;I2;MS;T1;W10\n");

  /*  Intialise boxcar
MR=master reset,  I2=Set Analogue channels 1,2 for
output, MS= Sync. mode, T1=Trigger every pulse
(Default every third pulse, T3)
W0= Send delay=zero;
see pg 45 of boxcar manual for further info */

  _clearscreen(_GCLEARSCREEN);

void SHG(int averages)
{
  float shg,ref,normalised,ch1,ch2,dist;
  int i,j,points,byted,byte1,byte2,byte3,steps,rback;
  FILE *out;

/**** Construct string to scan channels 1 & 2 for the
number of averages ***/

  itoa(averages,stringAve,10);
  strcpy(sc,"OUTPUT 16;SC1,2:");
  strcat(sc,stringAve);
  strcat(sc,"\n");

/*** Construct string for block read of scan data
directly into a vector ***/

  itoa(scanSize+1,stringScan,10);
  strcpy(blockRead,"ENTER 16 #");
  strcat(blockRead,stringScan);
  strcat(blockRead," BUFFER %d:%d\n");
  steps = distMicrons/STEPSIZE;
  for(j=0;j<=steps;j++) {
/********************************/
```

```
   ieeewt("OUTPUT 16;MR;I2;MS;T1;W255\n");
/*IMPORTANT TO STOP TIME OUT ERROR */
points=0;
/*********************************/
shg=ref=normalised=0.0;
ieeewt(sc);
while (points < averages) {
ieeewt("OUTPUT 16;?N\n");
/* Wait until scan has completed */
ieeewt("ENTER\n");
ieeescnf("%d",&points);
}
ieeewt("OUTPUT 16;X\n");
ieeeprtf(blockRead, segment(bytes), offset(bytes));
for(i=1;i<scanSize;i=i+4) {


/*******************************************
******************************/
/* This reads the data from the scan back.
(see page 46 of boxcar manual) */
/* IMPORTANT TO NOTE THAT ONE TERMINATION BYTE
IS SENT AT END OF TRANS.   */
/*      also note that numbers MUST be cast to unsigned
chars            */
/*******************************************
******************************/


ch1 = (unsigned char)bytes[i];
ch1 = ch1 + (((unsigned char)bytes[i-1] & '\017') << 8);
if (((unsigned char)bytes[i-1] & '\020') == '\020')
ch1 = -1 * ch1;
ch1 = ch1 * 0.0025;
ch2 = (unsigned char)bytes[i+2];
ch2 = ch2 + (((unsigned char)bytes[i+1] & '\017') << 8);
if (((unsigned char)bytes[i+1] & '\020') == '\020')
ch2 = -1 * ch2;
ch2 = ch2 * 0.0025;
/*********************************************
***************************/
  if (ch2>0.0) {
shg=shg+ch1;
ref=ref+ch2;
normalised=normalised + (ch1/(ch2));
  }
```

```
}
StepRot();
/* Move to next position */
normalised=normalised/averages;
shg=shg/averages;
ref=ref/averages;
dist=j * STEPSIZE / 1000.0;
/* distance in mm */
_settextposition(1,1);
printf("Average shg signal = %f",shg);
_settextposition(2,1);
printf("Average ref signal = %f",ref);
_settextposition(3,1);
printf("Average normalised signal = %f",normalised);
_settextposition(4,1);
printf("Position = %5.3f mm",dist);
data[0][j] = dist;
data[1][j] = shg;
data[2][j] = normalised;
}
   out = fopen(datafile, "w");
/* file for results */
   for(j=0;j<=steps;j++)
   fprintf(out,"%f   %f\n",data[0][j],data[2][j]);
   fclose(out);
   rback = distMicrons + STEPSIZE;
   byted = rback/256;
   byte1 = byted/256;
   byte2 = byted - (256 * byte1);
   byte3 = rback - (256 * byted);

   /*  11=Rotary stage address, secondary address is
the commmand.
02 puts the rotary stage into remote control */

   ieeewt("SEND UNL MTA LISTEN 1102\n");
   ieeewt("SEND UNL MTA LISTEN 1104\n");
/* Negative Direction */

   /* Move all the way back to zero */

   strcpy(move,"SEND UNL MTA LISTEN 1106 DATA ");
   itoa(byte3,bytedum,10);
   strcat(move,bytedum);
```

```
  strcat(move,",");
  itoa(byte2,bytedum,10);
  strcat(move,bytedum);
  strcat(move,",");
  itoa(byte1,bytedum,10);
  strcat(move,bytedum);
  strcat(move,"\n");
  ieeewt(move);

  ieeewt("SEND UNL MTA LISTEN 1107 DATA 255,255\n");
/* Fast Speed */
  ieeewt("SEND UNL MTA LISTEN 1103 DATA 13\n");
/* Send drive command */
  ieeewt("SEND UNL MTA LISTEN 1101\n");
/* returns to local */
  out = fopen("display.bat", "w");
  fprintf(out,"ep.exe %s \n",datafile);
  fclose(out);
}


void StepRot()
{
ieeewt("SEND UNL MTA LISTEN 1102\n");
/* remote control */
ieeewt("SEND UNL MTA LISTEN 1105\n");
/* positive direction */

    /* move forward by the defined step size in microns */

strcpy(move,"SEND UNL MTA LISTEN 1106 DATA ");
itoa(STEPSIZE,bytedum,10);
strcat(move,bytedum);
strcat(move,",0,0\n");
ieeewt(move);

ieeewt("SEND UNL MTA LISTEN 1107 DATA 0,75\n");
/* Slow Speed */
ieeewt("SEND UNL MTA LISTEN 1103 DATA 13\n");
/* Send drive command */
ieeewt("SEND UNL MTA LISTEN 1101\");
/* returns to local */
}


/* Waits for a user specified number of seconds before
```

```
 taking data */

void DoorClose()
{
  time_t time1;
  int elapse, oldelapse;

  time1 = time(NULL);
  oldelapse = 1;
  while (difftime(time(NULL), time1) < seconds) {
elapse =  difftime(time(NULL), time1) - seconds;
if (oldelapse != elapse) {
  _settextposition(1,1);
  printf(" %d seconds   ", elapse);
  _settextposition(2,1);
  printf("And Counting");
}
oldelapse = elapse;
  }
}
```

References

[1] P.A. Franken, A.E. Hill, C.W. Peters, and G. Weinreich. Generation of optical harmonics. *Phys. Rev. Lett.*, 7:118–119, 1961.

[2] Amnon Yariv. *Quantum Electronics*. John Wiley and Sons, third edition, 1989.

[3] L.D. Landau and E.M. Lifshitz. *Electrodynamics of Continuous Media*. Pergamon Press, 1960.

[4] M.E. Lines and A.M. Glass. *Principles and Applications of Ferroelectrics and Related Materials*. Clarendon Press, 1977.

[5] Le C.G. Fevre and Le R.J.W. Fevre. *Rev. of Pure and Appl. Chem.*, 5:261, 1955.

[6] Bloembergen N. *Nonlinear Optics*. Benjamin, 1965.

[7] M. Bass, P.A. Franken, A.E. Hill, C.W. Peters, and G. Weinreich. Optical mixing. *Phys. Rev. Lett.*, 8:18, 1962.

[8] W.H. Louisell. *Coupled Mode and Parametric Electronics*. Wiley, New York, 1960.

[9] J.A. Giordmaine and R.C. Miller. Tunable coherent parametric oscillation in $LiNbO_3$ at optical frequencies. *Phys. Rev. Lett.*, 14:973–976, 1965.

[10] M.W. McClain and D.M. Friedrich. Two–photon molecular electronic spectroscopy. *Ann Rev. Phys. Chem.*, 31:559–577, 1980.

[11] P.D. Maker and R.W. Terhune. Study of optical effects due to an induced polarization third order in the electric field strength. *Phys. Rev.*, 137 A:801–818, 1965.

[12] T.Y. Chang. *Opt. Eng.*, 20:220, 1981.

[13] V.M. Agranovich and D.L. Mills. *Surface Polarons*. North–Holland Publishing Co., Amsterdam, 1982.

[14] Y.R. Shen. *The Principles of Nonlinear Optics*. Wiley-Interscience, 1984.

[15] Pamela Thomas. Inorganic nonlinear materials. *Physics World*, Mar.:34–38, 1990.

[16] S.K. Kurtz and T.T. Perry. A powder technique for the evaluation of nonlinear optical materials. *J. Appl. Phys.*, 39:3798–3813, 1968.

[17] P.N. Butcher and D. Cotter. *The Elements of Nonlinear Optics*. Cambridge University Press, 1990.

[18] B.L. Davydov, L.D. Derkacheva, V.V. Dunina, M.E. Zhabotinskii, V.F. Zolin, L.G. Koreneva, and M.A. Samokhina. Connection between charge transfer and laser second harmonic generation. *ZhEFT Pis. Red.*, 12(1):24–26, 1970.

[19] G. Hauchecorne, F. Kerherve, and G. Mayer. Mesure des interactions entre ondes lumineuses dans diverses substances. *J. de Phys.*, 32:47–62, 1971.

[20] J.L. Oudar. Optical nonlinearities of conjugated molecules. stilbene derivatives and highly polar aromatic compounds. *J. Chem. Phys.*, 67(2):446–457, 1977.

[21] B.F. Levine and C.G. Bethea. Second and third order hyperpolarizabilities of organic molecules. *J. Chem. Phys.*, 63(6):2666–2682, 1975.

[22] K.D. Singer and A.F. Garito. Measurments of molecular second order optical susceptibilities using dc induced second harmonic generation. *J. Chem. Phys.*, 75(7):3572–3580, 1981.

[23] Kenneth David Singer. *Experimental Studies of Second Order Nonlinear Optical Susceptibilities in Organic Systems*. PhD thesis, Pennsylvania, 1981.

[24] C.J.F. Böttcher. *Theory of Electric Polarisation*. Elsevier, 1952.

[25] D.S. Chemla and J. Zyss. *Nonlinear Optical Properties of Organic Molecules and Crystals*, volume 2 of *Quantum Electronics*. Academic Press, 1987.

[26] D.S. Chemla and J. Zyss. *Nonlinear Optical Properties of Organic Molecules and Crystals*, volume 1 of *Quantum Electronics*. Academic Press, 1987.

[27] J. Zyss, J.F. Nicoud, and M. Coquillay. Chirality and hydrogen bonding in molecular crystals for phase–matched second–harmonic generation:N–(4–nitrophenyl)–(L)–prolinol (NPP). *J. Chem. Phys.*, 81(9):4160–4167, 1984.

[28] P.K. Tien. Light waves in thin films and integrated optics. *Appl. Opt.*, 10(11):2395–2413, 1971.

[29] B.K. Nayar and R.C. Booth. An introduction to integrated optics. *Br. Telecom. Tech. J.*, 4(4):5–15, 1986.

[30] George I. Stegeman and Colin T. Seaton. Nonlinear integrated optics. *J. Appl. Phys.*, 58(12):R57–R78, 1985.

[31] Marc De Micheli and Dan Ostrowsky. Nonlinear integrated optics. *Physics World*, Mar.:56–60, 1990.

[32] P.A. Norman, D. Bloor, J.S. Obhi, S.A. Karaulov, M.B. Hursthouse, P.V. Kolinsky, R.J. Jones, and S.R. Hall. Efficient second–harmonic generation in single crystals of 2– (N,N–dimethylamino) –5– nitroacetanilide. *J. Opt. Soc. Am. B*, 4(6):1013–1016, 1987.

[33] J.-C. Baumert, R.J. Twieg, G.C. Bjorklund, J.A. Logan, and C.W. Dirk. Crystal growth and characterization of 4–(N,N–dimethylamino)–3–acetamidonitrobenzene, a new organic material for nonlinear optics. *Appl. Phys. Lett.*, 51(19):1484–1486, 1987.

[34] J. Zyss. Nonlinear organic materials for integrated optics: a review. *J. Mol. Electron.*, 1:25–45, 1985.

[35] Y. Lansari, J. Ren, B. Sneed, K.A. Bowers, J.W. Cook, and J.F. Schetzina. Improved ohmic contacts for *p*–type *ZnSe* and related *p*–on–*n* diode structures. *Appl. Phys. Lett.*, 61:2554–2556, 1992.

[36] K. Nakano. Lecture, Durham Univ., 1994.

[37] Robert W. Boyd. *Nonlinear Optics*. Academic Press, 1992.

[38] I.M. Skinner and S.J. Garth. Reconcilliation of esu and mksa units in nonlinear optics. *Am. J. Phys.*, 58(2):177–181, 1990.

[39] Frits Zernike and John E. Midwinter. *Applied Nonlinear Optics*. John Wiley and Sons, 1973.

[40] Joseph Zyss, Christophe Dhenaut, Thai Chauvan, and Isabelle Ledoux. Quadratic nonlinear susceptibility of octupolar chiral ions. *Chem. Phys. Lett.*, 206(1,2,3,4):409–414, 1993.

[41] H. Fröhlich. *Theory of Dielectrics.* Oxford University Press, second edition, 1958.

[42] D.A. Kleinman. Nonlinear dielectric polarization in optical media. *Phys. Rev.*, 26:1977–79, 1962.

[43] J. Ducuing and C. Flytzanis. *Second order optical processes in solids*, pages 859–990. Optical Properties of Solids. North-Holland, Amsterdam, 1972.

[44] H. Rabin and C.L. Tang. *Quantum Electronics: A Treatise, Part A.* Academic Press, 1975.

[45] Paras N. Prasad, D.L. Beveridge, and M. Samoc. A coupled anharmonic oscillator model for optical nonlinearities of conjugated organic structures. *J. Chem. Phys.*, 91(4):2360–2365, 1989.

[46] J.L. Oudar and D.S. Chemla. Hyperpolarizabilities of the nitroanilines and their relations to the excited state dipole moment. *J. Chem. Phys.*, 66(6):2664–2668, 1977.

[47] J.A. Armstrong, N. Bloembergen, J. Ducuing, and P.S. Pershan. Interactions between light waves in a nonlinear dielectric. *Phys. Rev.*, 127:1918, 1962.

[48] Lars Onsager. Electric moments of molecules in liquids. *J. Am. Chem. Soc.*, 58:1486–1493, 1936.

[49] I. Ledoux and J. Zyss. Influence of the molecular environment in solution measurements of the second–order optical susceptibility for urea and derivatives. *Chem. Phys.*, 73:203–213, 1982.

[50] Y. Karakus, D. Bloor, and G.H. Cross. Enhanced linear electro-optic response and enhanced stability of thermo-poled 'guest-host' polycarbonate thin films. *J. Phys. D: Appl. Phys.*, 25:1014–1018, 1992.

[51] C.C. Teng and A.F. Garito. Dispersion of the nonlinear second-order optical susceptibility of organic systems. *Phys. Rev. B*, 28(12):6766–6773, 1983.

[52] B.F. Levine, C.G. Bethea, C.D. Thurmond, R.T. Lynch, and J.L. Bernstein. An organic crystal with an exceptionally large optical second–harmonic coefficient: 2–methyl–4–nitroaniline. *J. Appl. Phys.*, 50(4):2523–2527, 1979.

[53] G.F. Lipscomb, A.F. Garito, and R.S. Narang. An exceptionally large linear electro–optic effect in the organic solid MNA. *J. Chem. Phys.*, 75(3):1509–1516, 1981.

[54] J. Zyss and J.L. Oudar. Relations between microscopic and macro-scopic lowest–order optical nonlinearities of molecular crystals with one– or two–dimensional units. *Phys. Rev. A*, 26(4):2028-2048, 1982.

[55] I. Ledoux, D. Josse, P. Vidakovic, R.K. Raj, and R.B. Hierle. *Opt. Eng.*, 25:202, 1985.

[56] P.V. Kolinsky, R.J. Chad, R.J. Jones, S.R. Hall, P.A. Norman, D. Bloor, and J.S. Obhi. Second–harmonic generation in single crys-tals of 2–(N,N–dimethylamino)–5–nitroacetanilide (DAN) at 1.3 μm. *Electron. Lett.*, 23(15):791-792, 1987.

[57] Jason C. Cole, Judith A. K. Howard, Graham H. Cross, and Marek Sz-ablewski. The crystal structure of z–β–[(N, N'–diethylimmonium)–α–cyano–4–styryldicyanomethanide], a novel 'blue window' zwitterionic molecule for non–linear optics. *Acta Cryst.*, In Press, 1993.

[58] Marek Szablewski. Novel reactions of TCNQ: Formation of zwitterions for nonlinear optics by reaction with enamines. *J. Org. Chem.*, 59:954-956, 1994.

[59] Stanisław Kielich. Optical second-harmonic generation by electrically polarized isotropic media. *IEEE J. Quantum Electron.*, QE-5(12):562-568, 1969.

[60] Lap-Tak Cheng, Wilson Tam, Sylvia H. Stevenson, Gerald R. Mered-ith, Geert Rikken, and Seth R. Marder. Experimental investigations of organic molecular nonlinear optical polarizabilities. 1. methods and results on benzene and stilbene derivatives. *J. Phys. Chem.*, 95:10631-10643, 1991.

[61] Lap-Tak Cheng, Wilson Tam, Seth R. Marder, Albert E. Stiegman, Geert Rikken, and Charles W. Spangler. Experimental investigations of organic molecular nonlinear optical polarizabilities. 2. a study of conjugation dependences. *J. Phys. Chem.*, 95:10643-10652, 1991.

[62] P.A. Chollet, F. Kajzar, and J. Messier. Electric field induced optical second harmonic generation and polarization effects in polydiacetylene Langmuir–Blodgett multilayers. *Thin Solid Films*, 132:1-10, 1985.

[63] Y. Kawabe, H. Ikeda, T. Sahai, and K. Kawasaki. Second-order non-linear optical properties of new organic conjugated molecules. *J. Mater. Chem.*, 2(10):1025-1031, 1992.

[64] Mary L. Boas. *Mathematical Methods in the Physical Sciences*. John Wiley and Sons, second edition, 1983.

[65] C.R. Moylan. Advances in characterization of molecular hyperpolariz-abilities. Technical report, IBM Reasearch Division, 1992.

[66] P.D. Maker, R.W. Terhune, M. Nisenoff, and C.M. Savage. Effects of dispersion and focusing on the production of optical harmonics. *Phys. Rev. Lett.*, 8(1):21–22, 1962.

[67] J. Jerphagnon and S.K. Kurtz. Maker fringes: A detailed comparison of theory and experiment for isotropic and uniaxial crystals. *J. Appl. Phys.*, 41(4):1667–1681, 1970.

[68] G.D. Boyd, H. Kasper, and J.H. McFee. Linear and nonlinear optical properties of $AgGaS_2$, $CuGaS_2$, and $CuInS_2$, and theory of the wedge technique for the measurement of nonlinear coefficients. *IEEE J. Quantum Electron.*, QE-7:563–573, 1971.

[69] K.D. Singer, J.E. Sohn, L.A. King, H.M. Gordon, H.E. Katz, and C.W. Dirk. Second-order nonlinear-optical properties of donor– and acceptor-substituted aromatic compounds. *J. Opt. Soc. Am. B*, 6(7):1339–1349, 1989.

[70] Eugene Hecht. *Optics*. Addison-Wesley, second edition, 1987.

[71] Michael M. Choy and Robert L. Byer. Accurate second-order susceptibility measurements of visible and infrared nonlinear crystals. *Phys. Rev. B*, 14(4):1693–1706, 1976.

[72] J. Jerphagnon and S.K. Kurtz. Optical nonlinear susceptibilities: Accurate relative values for quartz, ammonium dihydrogen phosphate, and potassium dihydrogen phosphate. *Phys. Rev. B*, 1(4):1739–1744, 1970.

[73] William H. Press, Brian P. Flannery, Saul A. Teukolsky, and William T. Vetterling. *Numerical Recipes in C*. Cambridge University Press, 1988.

[74] E.A. Guggenheim. A proposed simplification in the procedure for computing electric dipole moments. *Trans. Faraday Soc.*, 45:714–20, 1949.

[75] F. Kajzar, I. Ledoux, and J. Zyss. Electric-field-induced optical second-harmonic generation in polydiacetylene solutions. *Phys. Rev. A*, 36(5):2210–2219, 1987.

[76] M. Nelkon and H.I. Humphreys. *Electrical Principles*. Heinemann, London, fourth edition, 1981.

[77] Paul Lorrain and Dale Corson. *Electromagnetic Fields and Waves*. W.H. Freeman, New York, second edition, 1970.

[78] Ch. Bosshard, K. Sutter, R. Schlesser, and P. Günter. Electro–optic effects in molecular crystals. *J. Opt. Soc. Am. B*, 10(5):867–885, 1993.

[79] Paras N. Prasad and David J. Williams. *Introduction to Nonlinear Optical Effects in Molecules and Polymers*. Wiley-Interscience, 1991.

[80] W.M.K.P. Wijekoon, Y. Zhang, S.P. Karna, P.N. Prasad, A.C. Griffin, and A.M. Bhatti. Second-order nonlinear optical effects in novel side–chain liquid crystalline polymers and monomers under bias of an applied dc electric field. *J. Opt. Soc. Am. B*, 9(10):1832–1842, 1992.

[81] M. Stahelin, C.A. Walsh, D.M. Burland, R.D. Miller, R.J. Twieg, and W. Volksen. Orientational decay in poled second-order nonlinear optical guest–host polymers: Temperature dependence and effects of poling geometry. *J. Appl. Phys.*, 73(12):8471–8479, 1993.

[82] Lian Li, Junyoung Lee, Xiaofan Zhu, Jayant Kumar, and Sukant K. Tripathy. Third-order optical nonlinearities in a photocrosslinkable polymer. *Jpn. J. Appl. Phys.*, 31:L89–L91, 1992.

[83] S.P.I.E., 1992.

[84] P.K. Tien and R. Ulrich. Theory of prism–coupler and thin film light guides. *J. Opt. Soc. Am.*, 60:1325–1337, 1970.

[85] Helmut K.V. Lotsch. Reflection and refraction of a beam of light at a plane interface. *J. Opt. Soc. Am.*, 58(4):551–561, 1968.

[86] M. Born and E. Wolf. *Principles of Optics*. Pergamon Press, fourth edition, 1970.

[87] M.J. Adams. *An Introduction to Optical Waveguides*. John Wiley and Sons, 1981.

[88] Prem Kumar Sharma. *Polymeric Thin Films for Integrated Optics*. PhD thesis, Durham, 1992.

[89] C.C. Yang, J.Y. Josefowicz, and L. Alexandru. Deposition of ultrathin films by a withdrawal method. *Thin Solid Films*, 74:117–127, 1980.

[90] M. Nakamura, A. Yariv, H.W. Yeh, S. Somekh, and H.L. Garvin. Optically pumped GaAs surface laser with corrugation feedback. *Appl. Phys. Lett.*, 22(10):515–516, 1973.

[91] D. Marcuse and E.A.J. Marcatili. Excitation of waveguides for integrated optics with laser beams. *Bell System Tech. J.*, 50:43–57, 1971.

[92] E.R. Schineller, R.P. Flam, and D.W. Wilmot. Optical waveguides formed by proton irradiation of fused silica. *J. Opt. Soc. Am.*, 58:1171–1176, 1968.

[93] P.K. Tien, R. Ulrich, and R.J. Martin. Modes of propagating light waves in thin deposited semiconductor films. *Appl. Phys. Lett.*, 14(6):291–294, 1969.

[94] T. Tamir. *Beam and Waveguide Couplers*, pages 83–137. Integrated Optics. Springer-Verlag, Berlin, 1975.

[95] F. Zernike. *Fabrication and Measurement of Passive Components*, pages 201–241. Integrated Optics. Springer-Verlag, Berlin, 1975.

[96] Gongjian Zhang and Keisuke Sasaki. Measuring anisotropic refractive indices and film thicknesses of thin organic crystals using the prism coupling method. *Appl. Opt.*, 27(7):1358–1362, 1988.

[97] Emile Pelletier, F. Flory, and Y. Hu. Optical characterization of thin films by guided waves. *Appl. Opt.*, 28(14):2918–2924, 1989.

[98] H. Kogelnik and V. Ramaswamy. Scaling rules for thin film optical waveguides. *Appl. Opt.*, 13:1857–1862, 1974.

[99] P.J. Wells. *Linear and nonlinear optical properties of poly (4 – vinylpyridine) waveguides.* PhD thesis, University of London, 1990.

[100] C.C. Teng and H.T. Man. Simple reflection technique for measuring the electro–optic coefficient of poled polymers. *Appl. Phys. Lett.*, 56(18):1734–1736, 1990.

[101] Jay S. Schildkraut. Determination of the electrooptic coefficient of a poled polymer film. *Appl. Opt.*, 29(19):2839–2841, 1990.

[102] K.D. Singer, W.G. Kuzyk, W.R. Holland, J.E. Sohn, S.J. Lalama, R.B. Comizzoli, H.E. Katz, and M.L. Schilling. Electro–optic phase modulation and optical SHG in corona–poled polymer films. *Appl. Phys. Lett.*, 53:1800–1802, 1988.

[103] John A. Riddick and William B. Bunger. *Techniques of Chemistry: Organic Solvents*, volume II. Wiley-Interscience, third edition, 1970.

[104] J.L. Brédas. Pers. Comm., 1994.

[105] G.H. Cross. Pers. Comm., 1994.

[106] D.L. Lee. *Electromagnetic Principles of Integrated Optics*. John Wiley and Sons, 1986.

[107] J. Cresswell. Pers. Comm., 1994.

[108] D. Marcuse. *Theory of Dielectric Optical Waveguides*. Academic Press, 1974.

[109] J. Brandrup and E.H. Immergut. *Polymer Handbook*. John Wiley Interscience, third edition, 1989.